STRUCTURAL INVESTIGATION OF CARBOPOL ETD2050 BY LIGHT SCATTERING

by

David Lee

BSc (Co-Op), Simon Fraser University, 2005

<small>A THESIS SUBMITTED IN PARTIAL FULFILLMENT

OF THE REQUIREMENTS FOR THE DEGREE OF

MASTER OF SCIENCE</small>

in the

Department

of

Physics

© David Lee 2009

Simon Fraser University

Summer 2009

APPROVAL

Name: David Lee

Degree: Master of Science

Title of thesis: Structural Investigation of Carbopol ETD2050 by Light Scattering

Examining Committee: Dr. Jeffrey M McGuirk
Chair

_____

Dr. Barbara J Frisken, Professor
Senior Supervisor

_____

Dr. Arthur E Bailey, President
SciTech Instuments Inc
Supervisor

_____

Dr. John L Bechhoefer, Professor
Supervisor

_____

Dr. Michael E Hayden, Professor
Supervisor

_____

Dr. Michael Plischke, Professor
Examiner

Date Approved: August 17th, 2009

Declaration of
Partial Copyright Licence

The author, whose copyright is declared on the title page of this work, has granted to Simon Fraser University the right to lend this thesis, project or extended essay to users of the Simon Fraser University Library, and to make partial or single copies only for such users or in response to a request from the library of any other university, or other educational institution, on its own behalf or for one of its users.

The author has further granted permission to Simon Fraser University to keep or make a digital copy for use in its circulating collection (currently available to the public at the "Institutional Repository" link of the SFU Library website <www.lib.sfu.ca> at: <http://ir.lib.sfu.ca/handle/1892/112>) and, without changing the content, to translate the thesis/project or extended essays, if technically possible, to any medium or format for the purpose of preservation of the digital work.

The author has further agreed that permission for multiple copying of this work for scholarly purposes may be granted by either the author or the Dean of Graduate Studies.

It is understood that copying or publication of this work for financial gain shall not be allowed without the author's written permission.

Permission for public performance, or limited permission for private scholarly use, of any multimedia materials forming part of this work, may have been granted by the author. This information may be found on the separately catalogued multimedia material and in the signed Partial Copyright Licence.

While licensing SFU to permit the above uses, the author retains copyright in the thesis, project or extended essays, including the right to change the work for subsequent purposes, including editing and publishing the work in whole or in part, and licensing other parties, as the author may desire.

The original Partial Copyright Licence attesting to these terms, and signed by this author, may be found in the original bound copy of this work, retained in the Simon Fraser University Archive.

Simon Fraser University Library
Burnaby, BC, Canada

Abstract

Carbopol, a family of cross-linked acrylic acid-based polymers and a well-known thickener used in personal care, household and industrial products, is often used as a model yield-stress fluid because it is transparent and its rheological properties can be precisely tuned by sample preparation conditions. Carbopol dispersions behave as an elastic solid, but they will flow when the applied stress exceeds a sample-dependent yield value. Both the yield-stress phenomena and the range of potential applications motivate the study of the microscopic structure and properties of yield-stress fluids. These investigation will lead to a fundamental understanding of the yield-stress phenomenon of Carbopol. Light scattering experiments investigating Carbopol ETD2050 dispersed in water have revealed that the Carbopol microstructure consists of a small and a large length scale, possibly described by different cross-linking densities. Experiments also show that the length scales and mass fractal dimension depend on the sample concentration and pH.

Acknowledgments

I have to first give my many thanks to Prof. Barbara Frisken and the Physics department at SFU for guiding me and giving me the opportunity to pursue this degree. Also I want to thank Dr. Art Bailey, who has helped me to understand the many aspects of instrumental and optical design, and who served on my supervisory committee. Many thanks to the other members of my supervisory committee, Prof. Michael Hayden and Prof. John Bechhoefer, who have supplied me with valuable input along the way. Many thanks to Prof. Michael Plischke, Prof. Martin Zuckermann, and Prof. Michael Eikerling for their insightful polymer discussions. I would have have to greatly thank all the members of the Frisken lab through the years, for all of the invaluable discussions. Finally a great big thank you goes to my Co-op coordinators Maggie Verity and Dr. Deborah Bartlette who without beginning to believe in me with Co-op, would have not brought me to where I am today, and have always encouraged me to challenge my goals and push myself to the limit. I extend much gratitude to endearing friends, Charlene and Mya, from whom many wonderful scientific and non-scientific discussion have flourished over the years. And always, I thank Christine, for her support and understanding, through the late nights, and the questions about chemistry, and the yelling at inanimate objects. To mom and dad – Factum est.

"Around here, however, we dont look backwards for very long. There's really no secret to our approach. We keep moving forward – opening up new doors and doing new things – because we're curious and curiosity keeps leading us down new paths."

— Walt Disney

Contents

List of Figures

List of Tables

Chapter 1

Introduction

Light scattering is a fact in our everyday lives. Everything around us is made of particles or molecules that scatter, from the rocks below our feet to the clouds above our heads. Take for example the atmosphere, which contains billions of natural and man-made particles that have the ability to scatter solar radiation in all directions. This thesis is focused on using Small-Angle Light Scattering (SALS) to study the microstructure of a commercial polymer gel called Carbopol, originally manufactured by BF Goodrich.

Gels are soft condensed matter materials; as they are intermediate between a solid and a liquid. They consist of subunits that aggregate to create a network that spans space and is typically immersed in a medium, which can be a liquid or gas. Depending on their composition, subunit and medium, the material properties of gels can vary from those of a viscous fluid to a semi-rigid solid [1].

Carbopol is a synthetic polymer gel consisting of polyacrylic acid crosslinked subunits. These subunits can be several microns in size, making light scattering an ideal method for studying their structure. Because of the synthetic nature of Carbopol, the physical properties are highly controllable and reproducible during manufacturing. These polymers can be used as an effective thickener across a large pH range and are less heat sensitive than other thickening agents. Apart from being an effective thickener, Carbopol polymers also possess a shear-thinning property (*i.e.* they thin under an applied stress) which enables their ease of distribution and extrusion [2].

Many of the studies of Carbopol have focused on its bulk rheology, its viscoelastic response to an applied force. Carnali and Naser characterize the network of Carbopol by measuring the intrinsic viscosity and overlap concentration to deduce the swelling ratio

[3]. Their work led to an illustrative model of Carbopol, as shown in Fig 1.1, adapted from Roberts and Barnes [4]. The proposed Carbopol structure consists of highly cross-linked centre and overlapping dangling ends.

Overlapping dangling ends   Highly cross-linked centre
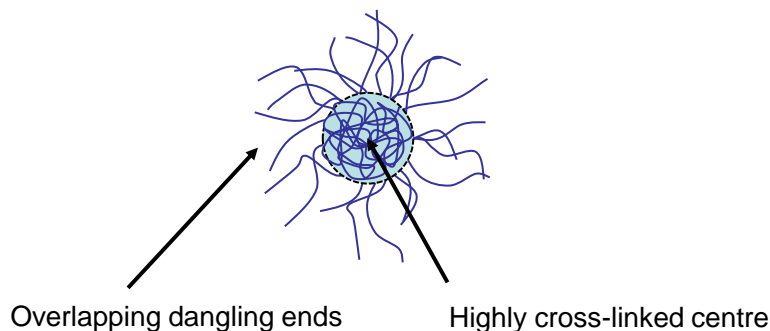
Figure 1.1: Illustrated structure of Carbopol with a dense cross-linked centre and overlapping polymer dangling ends. Adapted from Roberts and Barnes [4].

Analysis of the rheology measurement shows that there is an apparent yield stress over a range of pH [5, 6]. Yield stress is a property found in shear-thinning fluids. For stresses below the yield stress, no flow takes place and only solid-like or elastic behaviour is seen, and for stresses above the yield stress, flow occurs and liquid-like behaviour is observed. This description of yield stress can be applied to solids, like copper, and semi-solids, such as clay[7].

The rheology of Carbopol at the microscopic level has been studied using techniques such as optical tweezers [8], dynamic light scattering [9], and multiple-particle tracking [9, 10]. Carbopol samples prepared for theses techniques contain silica or polystyrene spheres to aid in the investigation. In optical tweezers experiments, a silica sphere is dragged through a sample and the measured displacements translate into directional forces. For Carbopol, it was found that these spheres encountered soft un-clustered obstacles ranging in size from 2 μm to about 10 μm [8]. In contrast to optical tweezer experiments where local structure is explored using spheres, dynamic light scattering (DLS) probes the ensemble behaviour of the scattering spheres. DLS shows that the mean-squared displacement decreases with increasing concentration. The observation of individual spheres, through particle tracking, shows that particles are trapped in a site for a period of time before abruptly moving to another site. The magnitude of the mean-squared displacement decreases with increasing concentration, consistent with DLS results. Increasing the concentration of Carbopol

reduces the size of the trapped site as well as the probability of site-to-site hopping. The behaviour of the spheres, inferred from both DLS and particle tracking experiments, is consistent with the schematic representation of Carbopol, shown in Fig. 1.1, where the particles probe the less-dense inter-particle regions of a nearly packed gel particle system [9]. Particle tracking also shows the existence of a two-phase system, with fast particles probing the viscous environments and slow particles probing the elastic environment. This result further supports the illustrated structure of Carbopol, where the fast particles are probing the exterior fluid region, while the slow particles are probing the polymer region [10].

The structure of Carbopol that has been investigated with optical microscopes, and observations conclude an interconnected fibrous structure for the un-neutralized dispersion [8], as shown in Fig. 1.2(a). Cryo-scanning electron microscopy has revealed that the un-neutralized dispersions are fibrous, (cf. Fig. 1.2(b)), while neutralized dispersions show honeycomb-like structures (cf. Fig. 1.2(c)). The apex points of the honeycomb structure are considered to be sites of crosslinking with the edges formed from the entanglement of polymers with neighbouring structures [11].

Similar studies of structure and rheology have been performed on poly(acrylic acid), the main component of Carbopol. Information gathered from poly(acrylic acid) should offer insight into the structure and behaviour of Carbopol. It was found that the structure and swelling of poly(acrylic acid) depend on pH, ionic strength and degree of crosslinking [12, 13]. Both light and neutron scattering experiments on gels, show power-law characteristics, evidence of a fractal system [14]. With the insight that the Carbopol gel particles could possibly be tens to hundreds of microns in size, small-angle light scattering should be an excellent method for probing the long-length-scale regime.

Light scattering is an excellent tool for studies in soft condensed matter where many systems have inhomogeneities with length scales ranging several orders of magnitude larger and smaller than the wavelength of light. Theses systems include, but are not limited to, polymers [15], colloids [16], micelles [17], liquid crystals [18], aerosols [19], vesicles [20], blood cells [21], and human hair [22]. Light scattering is a non-invasive probe, such that there is no physical contact or broken surface boundaries. Light scattering can also be used to probe viscoelastic properties of fluids and solids [23].

Light scattering has been studied since the late 19th century, where the problems being addressed were the sky, in particular its color and its polarization. Air molecules are much
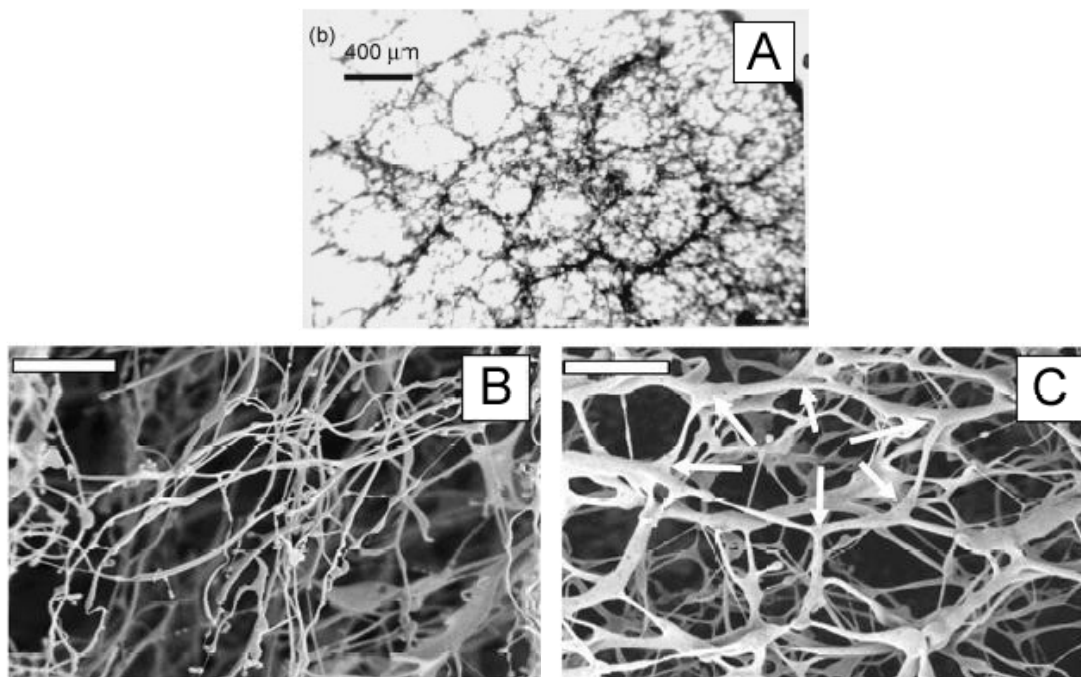
Figure 1.2: (a) Optical micrograph of 0.1 wt% Carbopl 960 with scale bar at 400 μm. Scanning electon micrographs of 0.1 wt% Carbopl 941 with the scale bar at 5 μm for (b) an un-neutralized dispersion and (c) dispersion neutralized with 1% TEA. Figures have been reproduced with permission of the publisher.

smaller that the wavelength of visible light from the sun. In 1871, John William Strutt (Third Lord Rayleigh) showed that the intensity of light scattered from particles much smaller than the wavelength of light increases as the inverse of the wavelength of the light raised to the fourth power [24]. Our atmosphere exhibits Rayleigh scattering. Suspended in the air are small particles of dust, ice crystals and water droplets, which scatter blue light more effectively than red, causing the sky to appear blue. As the sun sets, the preferential scattering of short-wavelength(blue) leaves long-wavelength(red) to penetrate through the atmosphere, causing a red sunset. When the particles are larger in size, like water droplets in a cloud, all wavelengths of light are scattered, so that clouds appears white. White clouds can also form from a large concentration of small particulate matter. The denser these clouds become, the less of incoming light is transmitted through the cloud, and the darker they appear [25].

Light scattering is a simple tool because of the simple connection between quantities

measured in experiments and those which are predicted by statistical mechanics. Two types of light scattering experiments will be described here, each providing a different set of information. Static Light Scattering (SLS) measurements yield the angular dependence of the averaged scattered light intensity, and provides structural information about the system. In a dilute system, information about the shape of individual particles can be obtained, while in a concentrated system, information about the spatial arrangement of the particles can be determined. Dynamic Light Scattering (DLS) amounts to the analysis of the time-dependent fluctuations in the scattered light intensity. This yields dynamic information, such as how the particles are moving (*eg* Brownian motion) and how their shape fluctuates in time [26].

In scattering experiments, the measured structural length scale Λ is given by $\Lambda = 2\pi/q$, where q is the magnitude of the scattering wave vector. The scattering wave vector is related to the angle between the scattered and incident beam, θ, by the relation $q = 4\pi/\lambda_n \cdot \sin(\theta/2)$, where λ_n is wavelength of light in the media and n is the refractive index on the scattering medium. Therefore, the structural length scale varies inversely with the scattering angle and linearly with the wavelength of light [27]. Figure 1.3 presents a plot of the the relative structural size, Λ/λ_n as a function of the scattering angle θ. In order to measure large structures, as anticipated for Carbopol gels, it is necessary to either perform measurements using a measurement wavelength comparable to the size of the structure and at larger angles or to perform measurements with shorter wavelengths and at smaller angles. Chapter 2 describes the development of a small-angle light scattering instrument at a fixed wavelength.

Light scattering instruments have evolved from custom instruments using optics with single-angle, single-photon counters [28] to coherent sources, commercial optics and a larger angular range equipped with digital correlators [29]. Commercially available laser scattering instruments can perform measurements of the scattered intensity as a function of angle and/or the scattered intensity correlation function at a fixed scattering angle. Currently these instruments possess a limited angular range, typically 20° to 150°, enabling characterization of a range particle sizes, such as $\Lambda = 1$ to 330 nm using a 632 nm wavelength light. These instruments are capable of time-scales that range from microseconds to milliseconds by utilizing photomultiplier tube detectors and digital correlators.

Small-angle scattering instruments tend to be physically long so that the scattered signal at small angles can be separated from the unscattered signal at zero degrees. One of the early small-angle light scattering instruments was developed at Bell laboratories using a

$$\frac{\Lambda}{\lambda_n} \propto \frac{1}{\sin(\theta/2)}$$
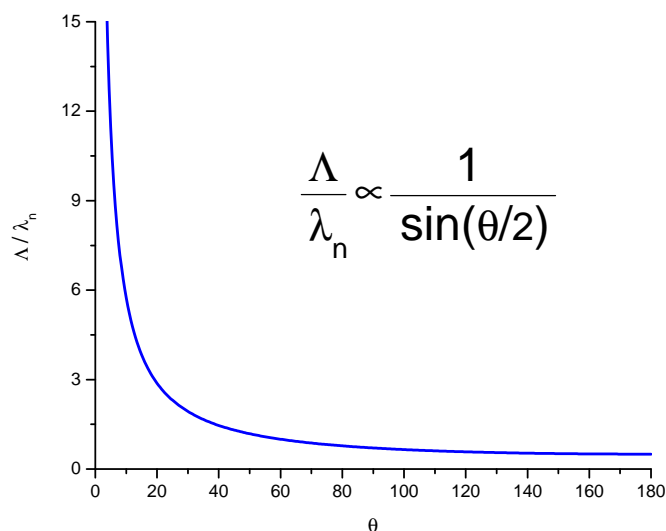
Figure 1.3: Relative structural size Λ/λ_n as a function of the scattering angle θ

long optical axis, folded using mirrors to conserve space, with a 1D silicon photodetector [30]. During the past ten years, there has been increased commercial development of CCD and CMOS sensor technology, as well as advances in computer technology. CCD and CMOS cameras offer the advantage of a two-dimensional array of photon detectors which in turn enable one to study the angle and polarization dependence of scattered light. An example of a small-angle light scattering instrument for small-angle static light scattering utilizing these new technologies was built by F. Ferri [31]. Faster computers have allowed for the design of a computer based real-time autocorrelator for use in small-angle dynamic light scattering [32]. Several other instruments were developed enhancing different aspects of small-angle light scattering instruments [27]. The instrument that we have designed and commisioned presently consists of a 2D-CCD camera to capture images spanning a scattering angular range of $\theta = 0.08°$ to $12.95°$ which translates to a structural size range of Λ from ≈ 2 to $\approx 450\mu$m using a helium-neon laser.

Using small-angle light scattering to characterize the structure of Carbopol polymers will aid the development of refined structural models. The structure of Carbopol could be considered to be a gel particle [3], a heterogeneous paste [33], or a glass [34]. Information about structure could lead to insights regarding the behaviour and rheology and perhaps an understanding about the origin of the yield stress in Carbopol [3].

Information about the structure and rheology of Carbopol polymers allows

manufacturers to provide product with a wide range of viscosities. Carbopol is fairly transparent and its rheological properties, including the yield stress, can be tuned to suit a wide range of application. Carbopol has been successfully used in the formulation of commercial semisolids and pharmaceutical products. General semisolid products are shampoos, lotions, creams, toothpastes [35] and ointments. Ointments are generally lotions suspending topical drugs, such as lidocaine, hydrocortisone, and methadone, for slow release [36].

1.1 Outline

The rest of the thesis is divided into three parts. Chapter 2 presents small-angle light scattering with an introduction to the theory and the instrumental design. The theory section discusses the development of static light scattering, from small scattering objects to large scattering objects. The instrumentation section covers the development, design and calibration of our small-angle light scattering instrument as well as a discussion of how we collect and analyze data. Chapter 3 presents Carbopol ETD2050 in the context of its polymer chemistry. This is followed by the results and interpretation of the Carbopol ETD2050 light scattering study. Chapter 4 summarizes the entire study, with suggestions for further investigations.

Chapter 2

Small-Angle Light Scattering

Measuring the angular distribution of light scattered from a sample makes it possible to determine the size, shape, diffusion coefficient, and molecular weight of particles in a sample. Instrumentation makes it possible to measure the total light intensity (static light scattering) and changes in light intensity as a function of time due to time-dependent processes in the sample (dynamic light scattering).

Commercially available laser scattering instruments can perform measurements over an angular range that is typically $20°$ to $150°$, enabling characterization of a range of particle sizes, such as $\Lambda = 1$ to 330 nm using 632 nm wavelength light, and time scales that range from microseconds to milliseconds by utilizing photomultiplier tubes and digital correlators. During the past ten years, there has been increased commercial development of CCD and CMOS sensor technology and advances in computer technology. Coupled with increased interest in the study of systems that are inhomogeneous on length scales of order of the wavelength of light or larger, such as colloids, gels, porous media and foams, this has prompted a rapid development of small-angle light scattering (SALS) techniques and designs [27].

In this chapter I present an introduction to the theory and instrumentation associated with small-angle light scattering. In the theory section, I will discuss the development of static light scattering, from the early days of Rayleigh to the contributions of Maxwell, from small scattering objects to large scattering objects. The instrumentation section will cover the development, design and calibration of our small-angle light scattering instrument as well as a discussion on how we collected and analyzed data.

2.1 Principles of Light Scattering

In 1871, Rayleigh showed that for the case where the wavelength of the electromagnetic wave interacting with a particle is much larger than the particle diameter, the electric field can be considered approximately constant throughout the volume of the particle [24]. The particle responds to the incident electric field as an oscillating dipole, radiating in all directions. The induced dipole moment is proportional to the electric field through the polarizability tensor α. The polarizability of materials is often isotropic, in which case α is treated as a scalar. The angular distribution of the scattered light intensity, I_s, from linearly polarized incident light is written as [37]

$$I_s = I_o \frac{k^4 \alpha^2}{r^2} \sin^2 \Phi \quad , \tag{2.1}$$

where r is the distance between the particle and the observation point, I_o is the intensity of incident light and k is the magnitude of the propagation vector written as

$$k = \frac{2\pi n_s}{\lambda_o} \quad , \tag{2.2}$$

where n_s is the refractive index of the surrounding medium and λ_o is the wavelength of light in vacuum. Φ is the angle between the scattering direction and the polarization of the incident light, which is related to the scattering angle θ and the angle between the incident polarization and the scattering plane ϕ by

$$\sin^2(\Phi) = 1 - \sin^2(\theta) \cos^2(\phi) \quad , \tag{2.3}$$

as depicted in Fig. 2.1. The Rayleigh-Gans-Debye (RGD) approximation arises from the assumption that the intensity of the scattered light depends only on the spatial arrangement of the scattering volume elements and the assumption that the amplitude and phase of the incident wave is unaffected by the particle. These conditions lead to a region where the RGD approximation is valid given by

$$\frac{2\pi L}{\lambda_o} \left(\frac{n_p}{n_s} - 1 \right) \ll 1 \quad , \tag{2.4}$$
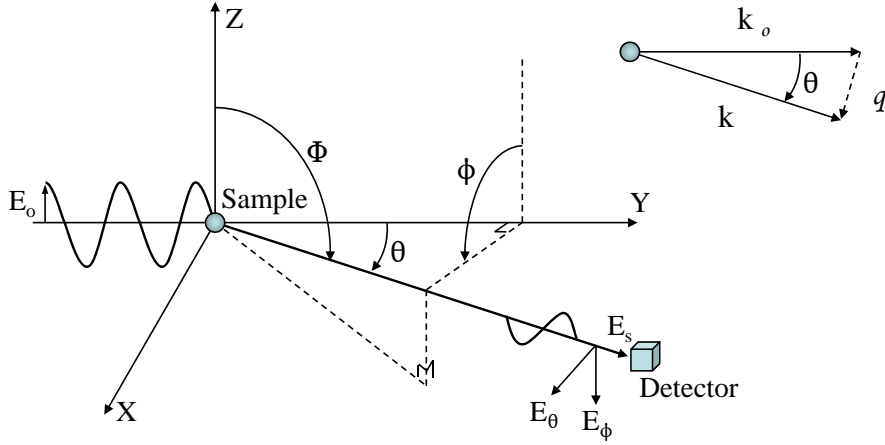
Figure 2.1: Diagram of the scattering geometry used throughout the thesis. (X, Y, Z) is the right-handed Cartesian coordinate system. E_o is the incident electric field propagating in the $+Y$ direction and E_s is the scattered electric field which is broken down into spherical components E_θ and E_ϕ. (Φ, θ, ϕ) are related scattering angles as described by Eq. 2.3.

where n_p is the refractive index of the particle, n_s is the refractive index of the surrounding medium, and L is the longest linear dimension of the particle. Therefore, RGD solutions are valid for particles of arbitrary shape only if the particle size compared to the wavelength of light is not too large ($L \ll \lambda$) and the relative refractive index is small ($n_p \approx n_s$) [38].

Often the scattered intensity is written in terms of the scattering wave vector $\mathbf{q} = \mathbf{k} - \mathbf{k_o}$, where $\mathbf{k}$ is the scattered wave vector and $\mathbf{k_o}$ is the incident wave vector. We are often interested in the magnitude which is written as

$$|\mathbf{q}| = q = \frac{4\pi n_s}{\lambda_o} \sin\left(\frac{\theta}{2}\right) \quad . \tag{2.5}$$

In far-field scattering, where the angular intensity distribution is independent of distance from the scatterer, it is often standard to define a term independent of the particle to object distance, called the Rayleigh ratio $\mathcal{R}$, which for larger particles is a function q [37]. The Rayleigh ratio is the ratio of the scattered intensity to the incident intensity, written as

$$\mathcal{R}(q) = \frac{I_s}{I_o} = \frac{k^4 \alpha^2 \rho}{\lambda^4} \sin^2 \Phi F(q) \quad , \tag{2.6}$$

where ρ is the particle number density in solution, and $F(q)$ is the scattering factor consisting

of two separable terms

$$F(q) = P(q)S(q) \quad . \tag{2.7}$$

$P(q)$ is the form factor, which accounts for intraparticle scattering based on the shape and size of the particle. $S(q)$ is the structure factor, which accounts for interparticle correlations, and is a function of the local order and interaction potential. We will focus on the infinite-dilution regime where there are minimal interactions between particles; thus, $S(q) = 1$. The form factor is determined by a pair-wise sum over all possible (Z) scattering centres of a single particle

$$P(q) = \left\langle \left| \frac{1}{Z} \sum_{j=1}^{Z} e^{i\mathbf{q}\cdot\mathbf{r}_j} \right|^2 \right\rangle \quad . \tag{2.8}$$

For a homogeneous sphere of finite radius R, the calculation yields

$$P(q) = \left[\frac{2J_1(qR)}{qR} \right]^2 \quad , \tag{2.9}$$

where J_1 is the first-orderBessel function of the first kind.

According to Maxwell's equations, the exact analytical solution for scattering takes the form of the Helmholtz equation. Electromagnetic scattering from a single object has received much attention and a comprehensive survey has been presented in many scattering texts [38, 39, 40].

The solution for any isolated three-dimensional object is possible if the objects surface can be describe in a coordinate system where the solution wavefunction is separable. This has been accomplished for a homogeneous cylinder [41], sphere [42], and ellipsoid [43] as well as layered systems [44]. The analytical solution for scattering from a sphere, known as the Mie solution, will be described here as it will be used in our study of polystyrene latex spheres in Sec. 2.5.3.

The Mie solution solves the problem of an isolated, spherical, homogeneous, isotropic, dielectric particle of arbitrary radius in a non-absorbing medium immersed in an electromagnetic wave of arbitrary wavelength. The solution for the sphere was first presented by Ludvig Lorenz in 1890 [45] and independently presented by Gustav Mie in 1908 [42]; since then the solution has been referred to as the Lorenz-Mie or Mie solution. Clear mathematical treatments of the underlying solution are presented in various scattering texts [38, 39, 40],

and a brief review is presented here.

The relationship between the incident (E_o) and scattered (E_s) electric field is established by defining a scattering matrix **S** with wave propagation in the $+y$-direction:

$$
\left(\begin{array}{c} E_{||} \\ E_{\perp} \end{array} \right)_s = \frac{e^{ik(r-y)}}{-ikr} \left(\begin{array}{cc} S_{11} & S_{12} \\ S_{21} & S_{22} \end{array} \right) \left(\begin{array}{c} E_{||} \\ E_{\perp} \end{array} \right)_o \quad , \tag{2.10}
$$

where the subscripts refer to the electric field polarization, parallel ($||$) and perpendicular ($\perp$) to the scattering plane defined by ϕ. For spherical particles, the off-diagonal elements S_{12} and S_{21} are zero and the diagonal elements depend solely on the scattering angle θ [46]. The diagonal elements of the scattering matrix can be written

$$
S_{11}(\theta) = \sum_{j=1}^{\infty} \frac{2j+1}{j(j+1)} \left(a_j \pi_j(\cos\theta) + b_j \tau_j(\cos\theta) \right) \quad , \tag{2.11}
$$

$$
S_{22}(\theta) = \sum_{j=1}^{\infty} \frac{2j+1}{j(j+1)} \left(a_j \tau_j(\cos\theta) + b_j \pi_j(\cos\theta) \right) \quad , \tag{2.12}
$$

where a_j and b_j are coefficients involving Riccati-Bessel functions. The functions π_j and τ_j depend on the scattering angle θ and are written in terms of the Legendre polynomials. Additional details about these functions and coefficients are presented in Appendix A.

In spherical coordinates and in the far-field limit, the electric field components, $E_{||}$ and $E_{\perp}$, are equivalent to E_{θ} and E_{ϕ} respectively, as shown in Fig. 2.1. The associated scattered intensities $I_{\theta s}$ and $I_{\phi s}$ are given by

$$
I_{\phi s}(\theta, \phi) = \frac{1}{k^2 r^2} |S_{11}(\theta)|^2 \sin^2 \phi \quad , \tag{2.13}
$$

$$
I_{\theta s}(\theta, \phi) = \frac{1}{k^2 r^2} |S_{22}(\theta)|^2 \cos^2 \phi \quad . \tag{2.14}
$$

For scattering in an arbitrary direction (θ, ϕ) the form factor is given by

$$
P(\theta, \phi) = |S_{11}(\theta)|^2 \sin^2 \phi + |S_{22}(\theta)|^2 \cos^2 \phi \quad , \tag{2.15}
$$

where ϕ is the angle between the scattering plane and the incident polarization.

These calculations are extremely sensitive to the refractive indices of the scattering object and its surrounding medium. The number of terms required in the sum is based on

the convergence of the sum of Riccati-Bessel functions and can be described as a function of the size parameter (kR). Generally, we work in the range $0.02 \leq kR < 50$ when using a HeNe 632nm wavelength laser. According to Wiscombe [47] the number of terms, N, required for the coefficients, a_j, and b_j, to be small $(|a_j|^2 + |b_j|^2 < 10^{-14})$ is

$$N = kR + 4.05(kR)^{1/3} + 2 \qquad .$$ (2.16)

2.2 Instrumental Setup

The small-angle light scattering instrument used in these experiments is based on the previous work of F. Ferri [31] and is built on an optical breadboard to minimize mechanical vibrations. Figure 2.2 shows a schematic view of the apparatus from above, and Appendix B lists additional details about the various components used. The light source is a Thorlabs 12mW TEM00 helium-neon (He-Ne, $\lambda = 632.8$nm) linearly polarized laser with a beam diameter of 0.88mm.
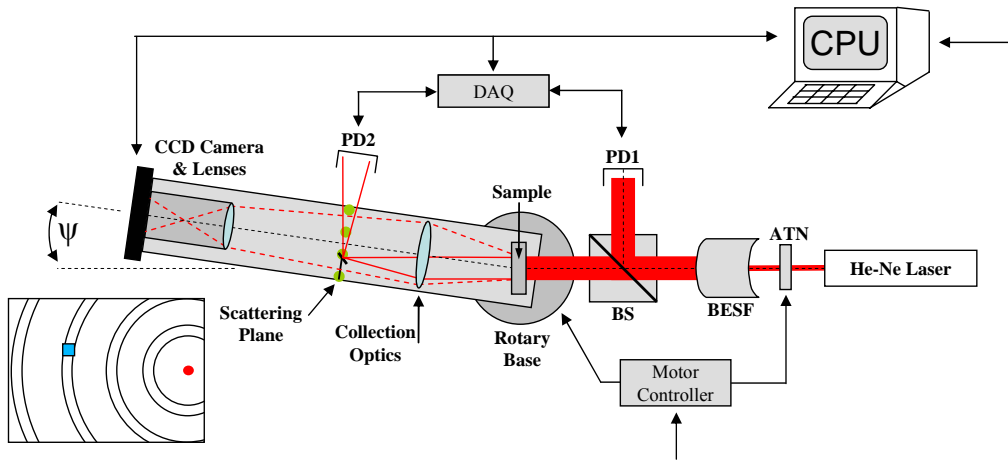
Figure 2.2: Schematic diagram of the small-angle light scattering instrument setup from above. Components are described in the text. The lower left shows the field of view seen by the camera, where the • represents the optical centre and the □ is representative of the size of a CCD pixel relative to one of the concentric rings of constant scattering angle θ. [Not to scale.]

The laser beam is sent through a series of components that attenuate the power and then reshape and expand the beam. The attenuator (ATN) consists of a mechanical linear

actuator controlled by a data acquisition board (DAQ - Data Translation DT9802) and can reduce the beam power up to a factor of $2x10^6$, as measured by a laser power meter. The beam diameter is expanded from its 0.88mm nominal diameter to a 2mm diameter utilizing a Keplerian beam expander (BESF) with a 10μm circular aperture for spatial filtering. The Keplerian beam expander operates by using two positive focal length lenses where the magnification is the ratio of the focal lengths. Spatial filtering is made possible by inserting a pinhole at the internal focal point of the lens pair. A 2 mm output diameter was selected to match the size of a CCD pixel to the size of the coherent scattering area. Matching these two areas is desirable for dynamic light scattering measurements.Dynamic light scattering is beyond the scope of this thesis, and is to be implemented at a later date. Following the BESF, a quartz plate (BS) deflects 30 % of the beam power off to a photodiode (PD1) which monitors the power of the light incident on the sample cell.

The sample cells used with the SALS instrument are cylindrical with a diameter of 19mm and long axis lengths of 1, 5, 10, and 26 mm. Long cells enables the user to measure weakly scattering or transparent samples while short cell enable the user to measure strongly scattering or turbid samples. During a measurement, a sample cell is mounted with its long axis along the incident optical axis and centred above the rotational center of a rotary base which connects to the detection system armature.

The collection optics, consisting of an achromatic doublet and a positive meniscus lens, converts all the scattered light from the sample at an angle θ to scattered light on a ring of radius r of constant scattering angle θ on the CCD defined by

$$r = Mf\tan(\theta) \quad , \tag{2.17}$$

where f is the focal length of the collection optics and M is the system magnification, which arises from imaging the image plane on to the CCD with the camera optics. We expect the magnification to be 1, so as to have the image plane and CCD the same size. Determination of the magnification is demonstrated in Sec. 2.5.2. A ray trace of two light rays in the scattering and imaging condition is presented in Fig. 2.3.

A mirror, made by polishing an engraving tool (Minitools) at $\sim45°$, is mounted on a xyz-translational stage (National Apertures) and placed in the focal plane of the collection optics (Thorlabs) to reflect the unscattered transmitted beam to a photodiode (PD2). The transmitted beam is removed to prevent saturation of the CCD. The detection system
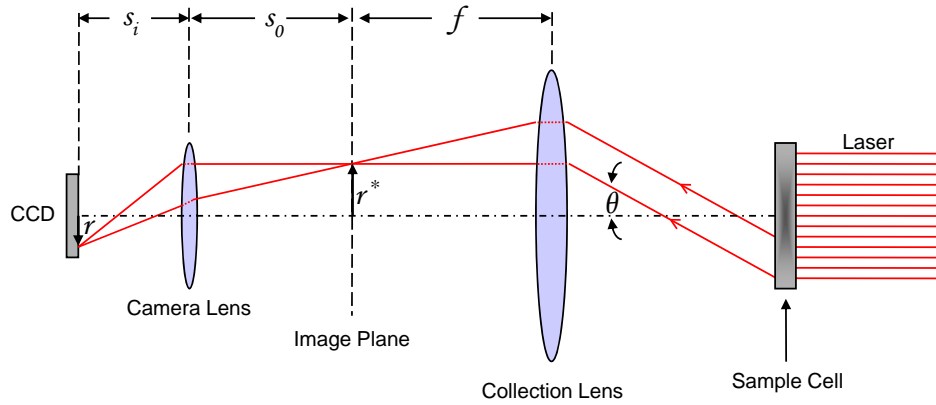
Figure 2.3: Ray trace of the optics in the setup, showing how two light rays scattered at an angle θ are mapped to a point on a ring of radius r^* in the image plane. The ring is subsequently mapped on to the CCD with a radius r.

consists of a 1200x1600 12-bit monochrome CCD camera (QImaging) with a line filter (Thorlabs), and an Apo-Rodenstock photo-optics (Linos).

The entire detection setup, collection lenses and camera, may be rotated away from the optical axis by an angle ψ. Off-axis illumination of the collection optics reduces lens aberrations resulting in better performance near the diffraction limit. With an off-axis collection optics, the optical centre on the CCD is located near one edge which gives an increased angular range without changing the magnification. The minimum observable angle for water-based scattering is 0.06°, corresponding to a scattering vector of 0.014 μm^{-1}. The minimum angle is set by the finite size of the beam dump and the size of a pixel on the CCD. Two imaging positions were utilized in this work presented here. In the primary imaging position, the arm offset angle is $\psi = 6°$, allowing for imaging at the minimum angle around the beam dump and a maximum observable angle of 9.68° and scattering vector of $q = 2.24$ μm^{-1}. A secondary imaging position, located at a total offset of $\psi = 18°$ which is away from the the beam, extends the maximum observable angle to $\sim 21°$ and the maximum scattering vector to $q = 4.82$ μm^{-1}. Systems with structural properties on length scales of $\Lambda = 2\pi q^{-1} \approx 3\mu$m to 450 μm can be investigated, which include emulsions, colloidal aggregates, gels, polymer blends, and vesicles. The images and results discussed in latter sections result from observations in the primary imaging position unless otherwise noted.

The final data are often presented in terms of the Rayleigh ratio $\mathcal{R}$ which is reported in

cm^{-1} units. However since the intensities are not referenced to the scattering of a standard scatterer, such as toluene, the Rayleigh ratios reported in this thesis are in arbitrary units (*au*).

Three instrumental limitations — vignetting, stray light, and dynamic range — must be investigated before using the instrument to study various samples.

2.2.1 Vignetting

Vignetting is a condition where not all of the light immersing a lens is collected. Because of the entrance pupil, an image of the limiting apertures along the optical axis, limiting some of the rays from the object from reaching the detector. This is recognized by a darkening in the peripheral regions of the image. Investigations of our optical setup revealed that the collection of light is in fact limited by the entrance pupil associated with by the camera optics. Figure 2.4 shows the effect of vignetting as observed in the scattered intensity measured for a sample of 1 μm polystyrene spheres. The graph of Fig. 2.4a is the radially averaged intensity of the image shown in Fig. 2.4b. In the RGD limit (Eq. 2.4) we would expect the scattered intensity to be consistent with Eq. 2.9 and decrease monatonically over the angular range. Instead the observed scattered intensity has a number of discontinuities denoted by the numbered bands. The fact that the numbered bands occur each time a scattering ring encounters a geometric edge of the CCD led us to investigate this problem in the context of vignetting.

To understand how we must arrange the optics in order to collect all of the light, the concept of conjugate optics is employed. A simple example of conjugate pairs in geometrical optics is the object and image planes of a lens. If there are multiple lenses, vignetting can occur as shown in Fig. 2.5. For this instrument, there are two conjugate pairs; one conjugate pair is formed by the collection lens which creates an image of the sample cell, denoted by an arrow, and the second conjugate pair is formed by the camera lens which maps the image plane onto the CCD. Figure 2.5 shows the effect of varying only the position of the sample cell. The values of s_i, s_o, and f are fixed for the desired angular mapping. The aperture stop forming the entrance pupil is located in the camera optics housing and is represented by $\perp$.

When the separation between the collection lens and the sample cell is small, as shown in Fig. 2.5a, the image of the sample cell appears behind the CCD, and some of the image forming rays are blocked by the aperture of the camera lens. When the separation between

(a) Ring-averaged count

(b) Scattered image
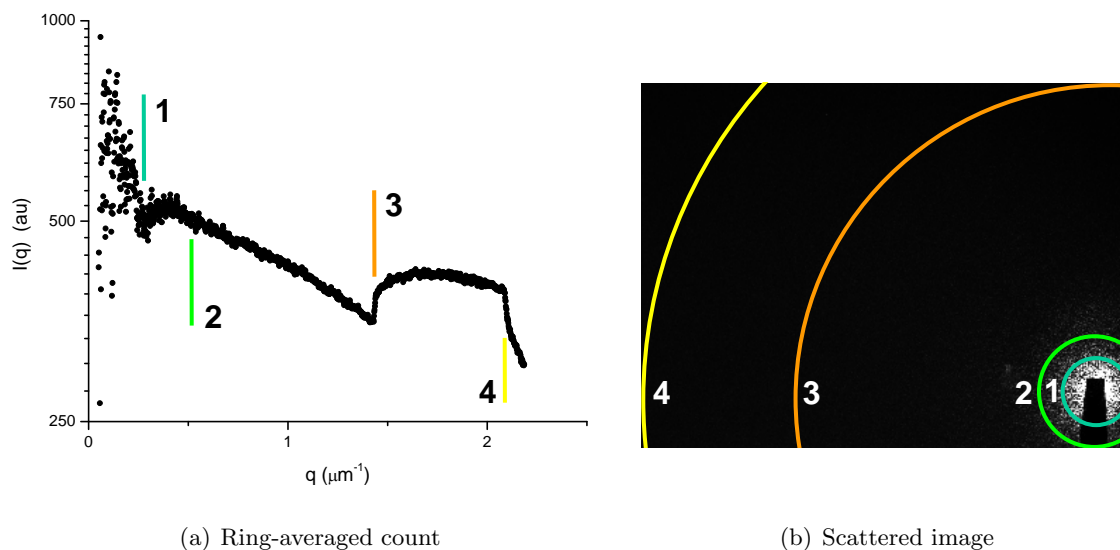
Figure 2.4: (a) Graph and (b) image illustrating the effects of vignetting. The numbered rings identify locations where scattering rings encounter a geometric edge of the CCD.

the collection lens and the sample cell is positioned correctly, as shown in Fig. 2.5b, the image of the sample cell is located at the plane of the camera lens, and all image forming rays are accepted by the aperture of the lens. When the separation between the collection lens and the sample cell is large, as shown in Fig. 2.5c, the image of the sample cell appears in front of the camera optics, and some of the rays which form it are blocked by the aperture of the camera lens.

Therefore, to minimize vignetting, the lenses should be positioned such that all of the light emitted at a particular angle is accepted by the aperture of the various lenses and the ideal case is depicted in Fig. 2.5b. The result of this alignment is presented in Fig. 2.6, which compares the scattered intensity before and after adjustments. The figure also shows the theoretical scattering curve calculated using Eq. 2.9 with $R = 500$nm and arbitrarily scaled to show the overall q-dependence.
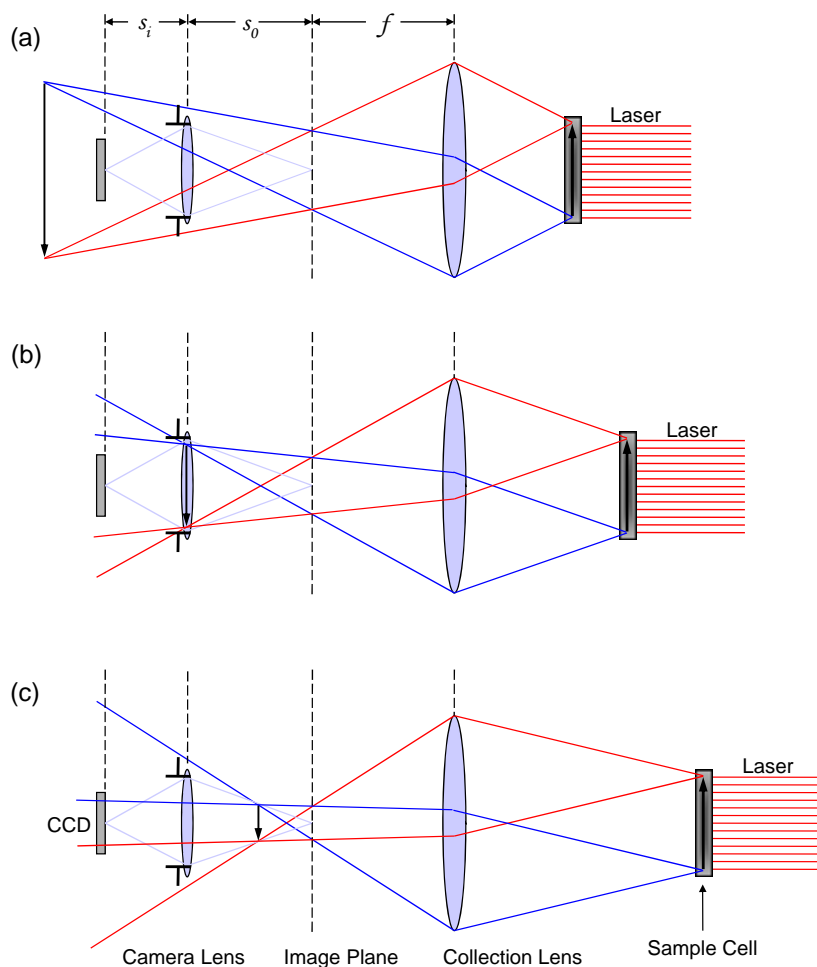
Figure 2.5: Conjugate optics setup demonstrating the two sets of conjugate pairs present in the detection optics. One conjugate pair is formed by the collection lens, which creates an image of the sample cell denoted by an arrow. The second conjugate pair is formed by the camera lens, which maps the image plane to the CCD. This figure depicts the effect on imaging conditions caused by the camera lens aperture as a function of the placement of the sample cell. The $\perp$ represents the location of the aperture stop within the camera optics. The values of s_i, s_o, and f are fixed for the desired angular mapping. (a) When the separation between the collection lens and the sample cell is small, the image of the sample cell appears behind the CCD, and some of the image forming rays are blocked by the aperture of the camera lens. (b) When the separation between the collection lens and the sample cell is positioned correctly, the image of the sample cell is located at the plane of the camera lens, and all image forming rays are accepted by the aperture of the lens. (c) When the separation between the collection lens and the sample cell is large, the image of the sample cell appears in front of the camera optics, and some the rays which form it are blocked by the aperture of the camera lens.
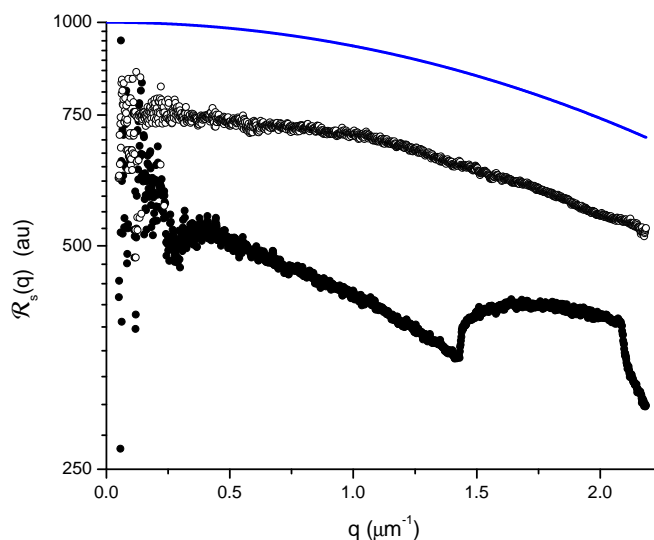
Figure 2.6: A comparison of the effect of conjugate-pair alignment on the scattering pattern of $1\mu m$ diameter polystyrene latex spheres. The ● represent data before alignment and the ○ represent data after alignment and cleaning of the optics. The theoretical curve represented by — has been scaled so as to better display the overall improvement in the q-dependence.

2.2.2 Stray Light

Stray light occurs mainly light is scattered from dirt along the optical beam path. To minimize stray light, all optical surfaces are anti-reflective (AR) coated, and all mounts and enclosures are treated to be flat black. The only interfaces that lack an AR coating are those associated with the sample cells, where every effort is made to keep the cell surfaces clean. Using the conjugate-pair optical alignment also reduces the stray light. Figure 2.7 illustrates the effect of optical alignment on the stray light, and shows that the conjugate pair optics setup appears to resolve the majority of stray-light problems that result from optical abberations.

2.2.3 Dynamic Range

Dynamic range is a measure of the ratio between the largest and the smallest measurable signal. The CCD camera possesses a 12-bit AD converter which results in a sensitivity of 3.6 decades in intensity. For an instrument of this design there are two ways to extend the
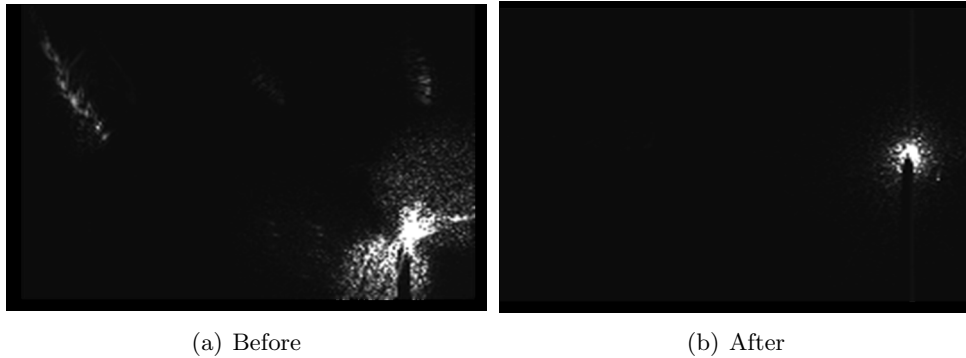
(a) Before   (b) After

Figure 2.7: Stray light observed (a) before and (b) after comparison after alignment of the optics. Images were captured by scattering from a water-filled cell at an exposure time of 100ms.

dynamic range: by varying the incident laser power for a fixed exposure time or using a fixed incident laser power with varying exposure times. We primarily used the latter of the two methods to extend the range of the intensities that could be measured.

To test this method, we measured the diffraction pattern caused by a 15 μm circular aperture. This resulted in an image of high dynamic range. We took a series of measurements with different exposure times T_{exp}. The final data was a composite of several images chosen to avoid saturation of the CCD at 4095 counts. This procedure increased the dynamic range beyond 12-bits by taking advantage of the linearity of the CCD [48].

Linearity was determined by acquiring images of the diffraction pattern using different exposure times. For each image, the same pixel slice consisting of 3200 pixels (2 pixels high, 1600 pixels wide) are extracted. A pixel-to-pixel comparison of the digital values obtained from the two exposure times was made. Each pixel-pair is compared by calculating

$$R = \frac{C_{Long}}{C_{Short}} \frac{T_{Short}}{T_{Long}} \quad , \tag{2.18}$$

where R is the intensity ratio scaled by the exposure time ratio, C_{Long} and C_{Short} are the digital counts from the pixel recorded from long and short exposure times respectively, and T_{Long} and T_{Short} are the long and short exposure times respectively. For perfect CCD operation, R would be 1 for each pixel, and a plot against either C_{Long} or C_{short} would result in a horizontal line of magnitude 1.

Typical data are shown in Fig. 2.8, which is a plot of R versus C_{Long} for a 3200

pixel-to-pixel comparison using a time ratio (T_{Long}/T_{Short}) of 2. The scaled intensity is constant and approximately equal to one in the range where C_{Long} is between 150 and 3500. There are two regions where $R \neq 1$, one at small values and one at large values of C_{Long}. At large values of C_{Long}, the scaled ratio becomes rapidly smaller because C_{Long} has reached the 4095 count saturation limit of the CCD, while C_{Short} has not. At small values of C_{Long}, the scatter in the ratio is due to the non-linear response of the CCD at count levels below 50 counts.
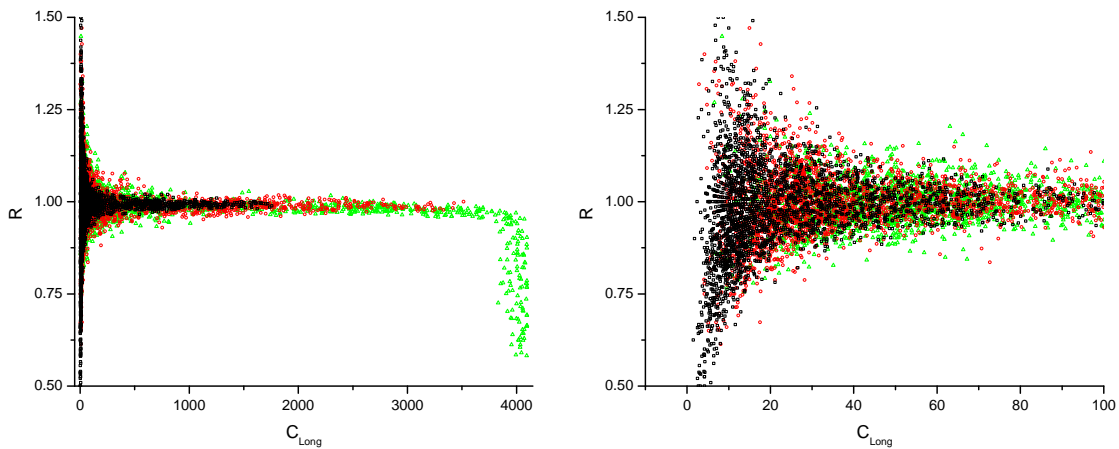
Figure 2.8: (a) Plot of the scaled count ratio R on the CCD readout for a time ratio of 2, using 3 different time sets ([100,200] ms, [300,600] ms, and [500,1000] ms). (b) Expanded view for low counts.

The scaled intensity ratio plateau value is not exactly one. For the data shown in Fig. 2.8 $\langle R \rangle = 0.99(3)$ over the identified plateau range. This indicates that the camera is not exactly linear. We found that the scaled intensity plateau value varies as a function of T_{Long}/T_{Short} and is independent of the choice of T_{Short}. Figure 2.9 show results for plateau values in the range $2 < T_{Long}/T_{Short} < 25$, and reveals a scaling dependence, which can be used to correct the values of individual pixel counts for different exposure times. Typical T_{Long}/T_{Short} ratios used in this work were between 2 and 10, which contributes about a 3% correction. This correction was not implemented in the work presented here, since the uncertainty of the mean intensity of a constant-θ scattering ring on the CCD is larger than the correction warranted for linearity.

By incorporating multiple exposure times and using data within the nearly linear
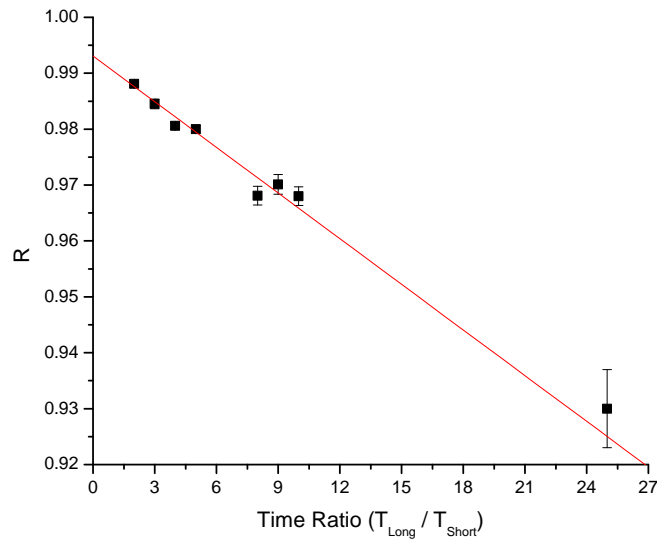
Figure 2.9: Average CCD linear response measured over the plateau range plotted as a function of the time ratio. This line is a linear fit to the data with a slope of $-0.0028(1)$ and an intercept of $0.9932(5)$.

response region, the dynamic range of the instrument is effectively extended to ≈ 8.4 decades which is equivalent to ≈ 28-bits. The dynamic range was estimated by observing the scattering of a range of scattering samples.

2.3   Measuring the Scattered Intensity

To compare data with theory, we need to obtain the Rayleigh scattering ratio, $\mathcal{R}(q)$, which is proportional to the measured intensity $I(q)$. The measured intensity also includes contributions from three sources: sample turbidity, measured solid angle, and light polarization. To measure $\mathcal{R}(q)$, these three contributions must be removed as they account for geometrical effects of the instrument.

Sample turbidity

Sample turbidity causes attenuation of light as it passes through the sample. The intensity of the transmitted light I_t through a sample is given by

$$I_t = I_o e^{-\tau l} \quad , \tag{2.19}$$

where I_o is the incident intensity, τ is the turbidity of the sample, and l is the thickness of the sample cell.
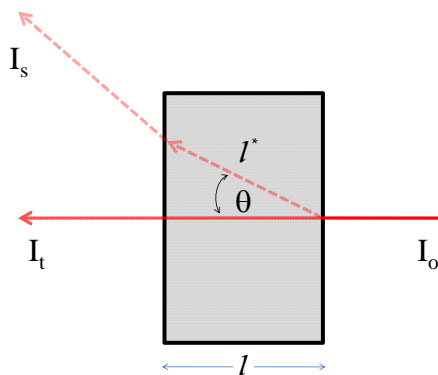
Figure 2.10: Schematic of the sample cell demonstrating the effect of the scattering angle θ on the apparent path length. In this figure l is the thickness of the sample cell and l^* is the apparent path length at a scattering angle θ.

Because of the geometry of the scattering cells, there are slightly different path lengths for light scattered at different angles, θ. Figure 2.10 shows a schematic representation of the scattering setup, where $l^* = l/\cos\theta$ is the apparent path length through the cell at a scattering angle θ. The intensity of the transmitted light I_t is then more accurately written in the form

$$I_t(\theta) = I_o e^{-\tau l^*} = I_o \left(e^{-\tau l}\right)^{1/\cos\theta} \quad . \tag{2.20}$$

The correction to the absolute intensity depends on the value of τl. For $\tau l = 1$ the correction amounts to $\approx 1.5\%$ at the largest scattering angle.

Measured Solid Angle

Correcting for the solid angle arises from the projection of the spherical scattering surface on to the flat surface of the CCD. Intensity provides a measure of the differential power per unit solid angle $\frac{dP}{d\Omega}$, where the solid angle is written as $d\Omega = \frac{dA}{r^2}$, A is the area of a CCD pixel, and r is the distance from the scattering point to the CCD pixel, as shown in Fig. 2.3. The projection of the CCD pixel area dA onto the scattering sphere is written as $dA = dA' \cos\theta$. The effective distance r from the scattering point to the CCD pixel is $r = r'/\cos\theta$, where r' is the distance from the scattering point to the detector at $0°$. The combination of these two corrections results in the actual solid angle being written as

$d\Omega = \frac{dA'}{r'^2}\cos^3\theta$. Therefore, the actual intensity I_{actual} from geometrical corrections at the CCD is

$$I_{actual} = \frac{dP}{d\Omega} = \frac{dP}{d\Omega'\cos^3\theta} = \frac{I_{measured}}{\cos^3\theta} \quad , \qquad (2.21)$$

where $I_{measured}$ is the measured intensity at the CCD before corrections. The geometrical correction amounts to $\approx 7\%$ at the largest scattering angle.
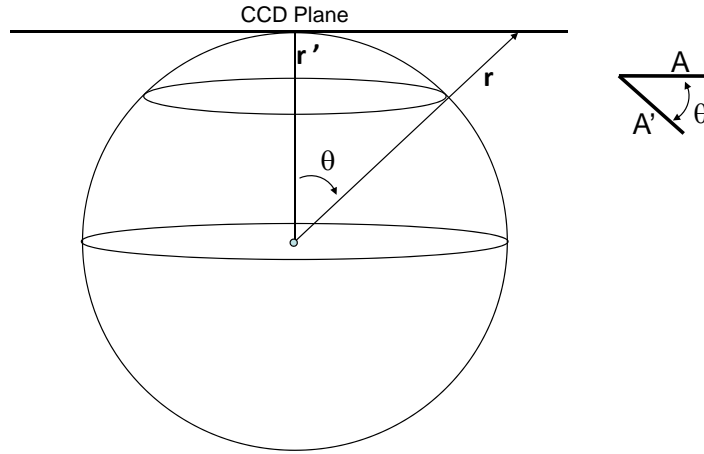
Figure 2.11: Geometry used in determining the correction to the solid angle. In this figure, r' is the distance from the scattering centre to the CCD at $0°$, r is the distance from the scattering centre to a CCD pixel at a scattering angle θ, A is the the area of a CCD pixel and A' is the area subtended by the pixel on the scattering sphere.

Light Polarization

This last correction assumes the use of linearly polarized incident light. As discussed previously and presented in Eq. 2.3, $\sin^2\Phi$ varies from pixel-to-pixel. Therefore, the correction applied is $\langle\sin^2\Phi\rangle$, which is the average over all of the pixels of the same scattering angle θ. For the scattering arrangement presented above, this translates to a $< 1\ \%$ correction at the largest scattering angle.

Complete mathematical form

The form of the scattered intensity, I_s, is rewritten to include the vignetting, solid angle and polarization contributions. Also included in the scattered intensity is a contribution

from the length of the scattering volume l^*,

$$I_s(q) \quad = \quad I_o e^{-\tau_s l^*} l^* < \sin^2 \Phi > \cos^3 \theta \mathcal{R}(q) \quad , \tag{2.22}$$

where τ_s is the turbidity of the scattering sample and $\mathcal{R}(q)$ is the Rayleigh ratio for the scattered light. The latter can be written as the sum of three Rayleigh ratios,

$$\mathcal{R}(q) = \mathcal{R}_s(q) + \mathcal{R}_{solvent}(q) + \mathcal{R}_{stray}(q) \quad , \tag{2.23}$$

where $\mathcal{R}_s(q)$, $\mathcal{R}_{solvent}(q)$, and $\mathcal{R}_{stray}(q)$ are the Rayleigh scattering contributions from the sample, solvent and stray light, respectively. The scattered intensity from the reference cell containing pure solvent is

$$I_r(q) \quad = \quad I_o e^{-\tau_r l^*} l^* < \sin^2 \Phi > \cos^3 \theta \left(\mathcal{R}_{solvent}(q) + \mathcal{R}_{stray}(q) \right) \quad , \tag{2.24}$$

where τ_r is the turbidity from the reference cell.

The combination of Eqs. 2.22 and 2.24 provides a method for obtaining the Rayleigh ratio for the sample:

$$\mathcal{R}_s(q) = \frac{1}{l^* < \sin^2 \Phi > \cos^3 \theta} \left[\frac{I_s(q)}{I_o e^{-\tau_s l^*}} - \frac{I_r(q)}{I_o e^{-\tau_r l^*}} \right] \quad . \tag{2.25}$$

This allows us to account for various geometrical corrections and directly apply in general Eq. 2.6 for interpretation of the data using various model form factors and structure factors.

2.4 Data Acquisition and Analysis Software

A customized LabVIEW program provides a software interface, control, and analysis for the SALS instrument. Figure 2.12 shows the user interface under the imaging tab with active blocks labeled 1 through 6.

Block 1 consists of the user input parameters: the radial region of interest (minimum / maximum radii and radial steps), the number of images to average over, the refractive index of the medium, the list of exposure times, and the type of method for handling multiple exposure times (ring, coupled-pixel, independent-pixel). The user also selects the sample cell thickness, the sample type (calibration pinhole or sample), the option for a debugging
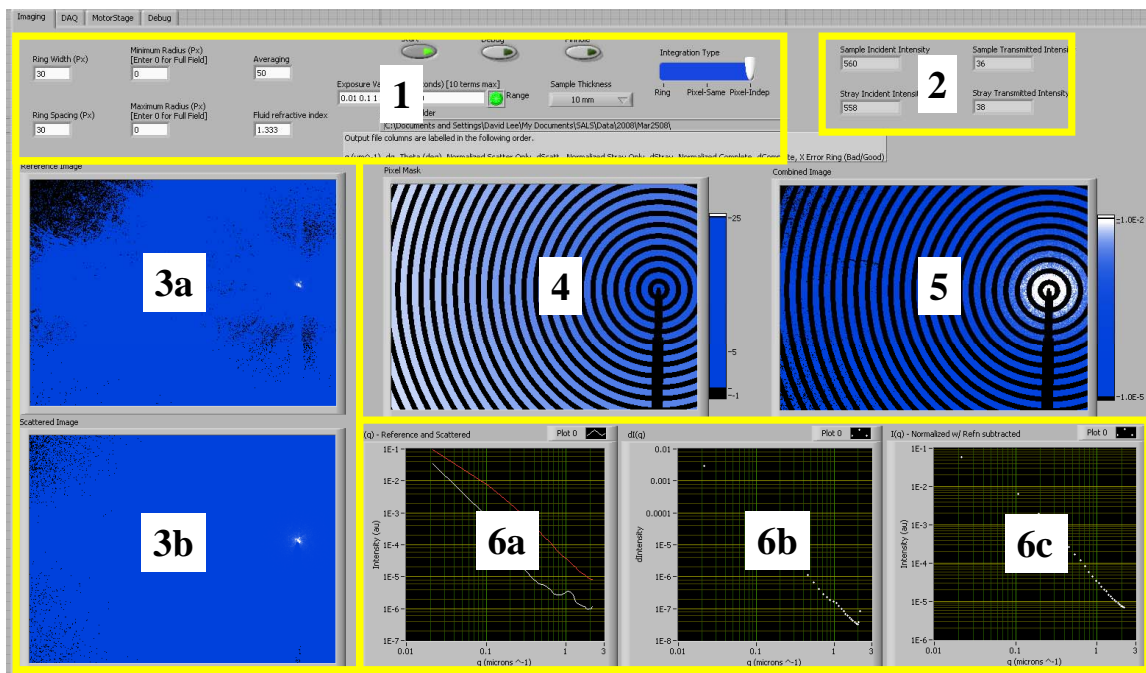
Figure 2.12: Front panel of the LabView software interface program. Block 1 consists of user interface parameters. Block 2 displays the average readings from the photodiodes and reports the calculated relative turbidity. Block 3 displays images from the reference and scattering samples. Block 4 presents the radial map for analysis. Block 5 shows the super position of the radial map with the final assembled image. Block 6 presents the radially-averaged value of the reference and scattering sample, as well as the Rayleigh ratio with uncertainty.

output which saves calculations at various points in the algorithm, and a save folder for all of the output files. Block 2 displays the average readings from the two collecting photodiodes for the reference and transmitted locations and reports a calculated turbidity relative to the reference. Blocks 3a and 3b display images from the reference sample and the scattering sample, respectively. Block 4 displays a map identifying each pixel with a particular ring, defined by the user parameters, displayed on a colormap. Block 5 displays the scattered intensity corrected for the reference intensity and normalized for the sample turbidity and exposure time. Block 6 plots the radially-averaged intensity results for the measurement. Block 6a plots the radially-averaged scattered and reference intensity for the images of Block 3. Block 6b plots uncertainty of the mean, and Block 6c plots the Rayleigh ratio of the corrected scattered intensity displayed in Block 5.

In addition to the imaging tab of the front panel, there are three other tabs across the top for additional uses. The DAQ tab provides an interface for adjusting the sensitivity and read-outs for measurements made by the photodiodes. The MotorStage tab enables the user to select from the two preset imaging positions and control the attenuation of the incident laser power. The Debug tab displays relevant images and graphs associated with various stages of the software.
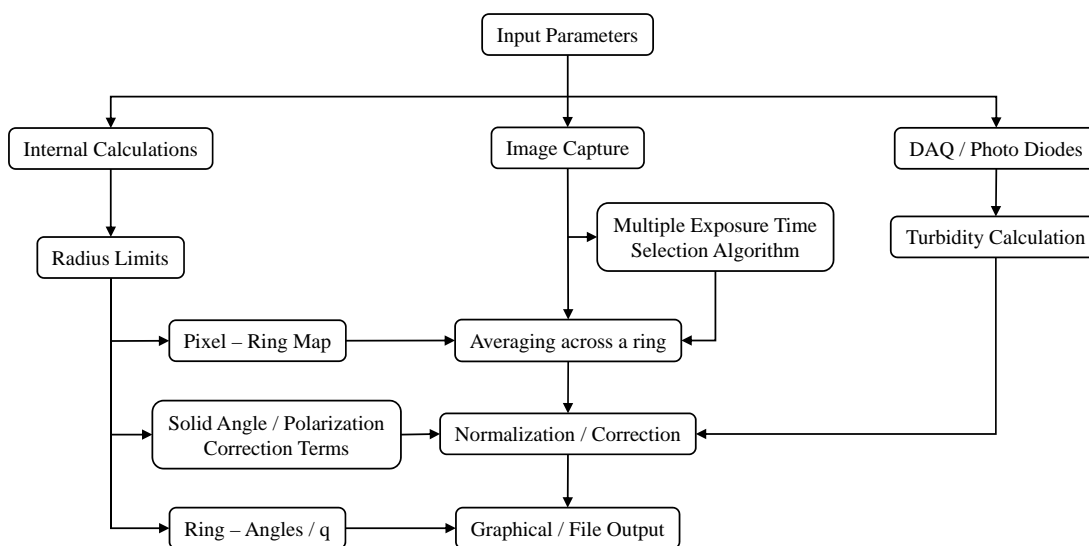
Figure 2.13: Flowchart of the LabView software program. Each of the three main vertical branches operate independently until an input is required from a parallel branch.

The organization of the data acquisition and analysis software is summarized in the flowchart shown in Fig. 2.13 and in the following text.

The software operates by first requiring the user to supply information for each of the input parameters in Block 1 of Fig. 2.12. The program is automated and provides prompts whenever required. When the program is started, it prompts the user to insert the reference cell containing the dispersing solvent. During the capture of the reference images, the photodiodes measure the incident and transmitted intensities of the laser. Upon completion, the program prompts the user to insert the sample cell. During the capture of sample scattering images, the photodiodes measure the incident and transmitted intensities of the laser.

During the capture of reference and sample images, the program calculates and assigns

each pixel to a particular scattering angle θ with uncertainty $\delta\theta$ due to the finite pixel size or ring width, and subsequently a scattering vector q with uncertainty δq. Following the assignment of angles, the scattering corrections are also calculated.

The images from different exposure times are handled as 2D arrays. Depending on the user selection for the method to handle multiple exposure times, an internal algorithm determines which rings of pixels or individual pixels are used from each exposure time. The selection algorithm determines the largest exposure time used where the digital intensity of each pixel or ring is within the linear range previously determined from linearity tests. Following the algorithm, a compiled image is constructed by using the appropriate pixel or ring normalized for the respective exposure time and the appropriate reference intensity is subtracted. This is followed by a correction to account for sample turbidity. The resulting image is displayed in Block 5 of Fig. 2.12.

The intensity of the compiled image is averaged along pixels from the same scattering ring with corrections applied and returns the Rayleigh ratio $\mathcal{R}_s$ with the standard deviation of the mean, $\delta\mathcal{R}_s$, and displayed in the graph of Block 6c. The data is then saved to a file. The output file columns listed in order are: scattering q, uncertainty δq, scattering angle θ, reference intensity I_r, uncertainty δI_r, sample intensity I_s, uncertainty δI_s, Rayleigh ratio $\mathcal{R}_s$, and uncertainty $\delta\mathcal{R}_s$.

Further details of the pixel-to-ring, ring-to-scattering vector q, and exposure-time-selection algorithms are presented in Appendix C.

2.5   Instrument Calibration

Calibration of the instrument consists of two steps: determining the optical centre, and determining the optical magnification. The scattering from polystyrene latex spheres was measured to check the results of the calibration.

2.5.1   Determining the Optical Centre

The location of the optical centre is required for the proper assignment of scattering angles and scattering vectors. Determining the optical centre to the highest precision possible also reduces the uncertainty in the scattering angle and scattering vector.

The optical centre was determined by attenuating the beam power and removing the beamdump allowing the laser to shine directly onto the CCD. The incident beam power was
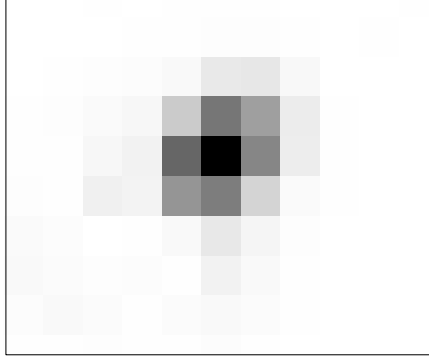
Figure 2.14: An 11x11 pixel section of an acquired image of the optical centre displayed using an inverted greyscale, where the brightest pixel is represented by the darkest pixel in the image. To the first approximation, the centre of the beam is determined by the location of the brightest pixel $(1438.0(5), 586.0(5))$.

attenuated to the point where image acquisition over a short $100~\mu s$ exposure time possible without saturating the CCD. The image profile is shown using an inverted greyscale in Fig. 2.14. To first approximation, the optical centre can be assigned to the brightest pixel of the pattern $(1438.0(5), 586.0(5))$ where the origin is locaed at the upper-left most pixel on the 1600x1200 CCD.

More accuracy is achieved by calculating the two-dimensional centre of mass of the intensity. By considering the intensities of the surrounding pixels, it is possible to determine the centre to sub-pixel accuracy. The centre $(\bar{x}_o, \bar{y}_o)$ with uncertainty σ^2 is defined by the centroid calculation for an $N \times M$ region

$$
\bar{x}_o = \frac{1}{M} \sum_{j=0}^{M} \frac{\sum_{i=0}^{N} x_{i,j} I_{i,j}}{\sum_{i=0}^{N} I_{i,j}} \quad , \qquad \bar{y}_o = \frac{1}{N} \sum_{i=0}^{N} \frac{\sum_{j=0}^{M} y_{i,j} I_{i,j}}{\sum_{j=0}^{M} I_{i,j}} \quad ,
$$
$$
\sigma_x^2 = \frac{1}{M} \sum_{j=0}^{M} \frac{1}{\sum_{i=0}^{N} I_{i,j}} \quad , \qquad \sigma_y^2 = \frac{1}{N} \sum_{i=0}^{N} \frac{1}{\sum_{j=0}^{M} I_{i,j}} \quad ,
$$

(2.26)

where $x_{i,j}$ is the horizontal index, $y_{i,j}$ is the vertical index and $I_{i,j}$ is the intensity of pixel (i,j). This mathematical algorithm performs a weighted-mean calculation across each row/column using the local intensity as the weighting factors followed by an average across the columns/rows. Applying Eq. 2.26 to the data shown in Fig. 2.14, the calculated optical centre is $(1437.91(4), 586.22(5))$. The first approximation of the optical centre is consistent with this more precise measurement.

2.5.2   Determining the Optical Magnification

Determination of the instrument's optical magnification was carried out using 10μm and 15μm nominal diameter circular apertures (National Aperture). To characterize the size, roundness, and manufacturing defects, the apertures were imaged using a Scanning Electron Microscope (SFU Nanoimaging Facility, FEI Strata DB235 FESEM/FIB). Typical images are shown in Fig. 2.15. The diameters of the apertures were measured by fitting a circle to the image and are found to be $10.7(1)\mu$m and $16.9(2)\mu$m respectively. The uncertainty is determined by the SEM imaging program from fitting a circle. The reported uncertainty is within the SEM's maximum uncertainty of 2% as determined using calibration targets.

(a) $10\mu m$ (b) $15\mu m$
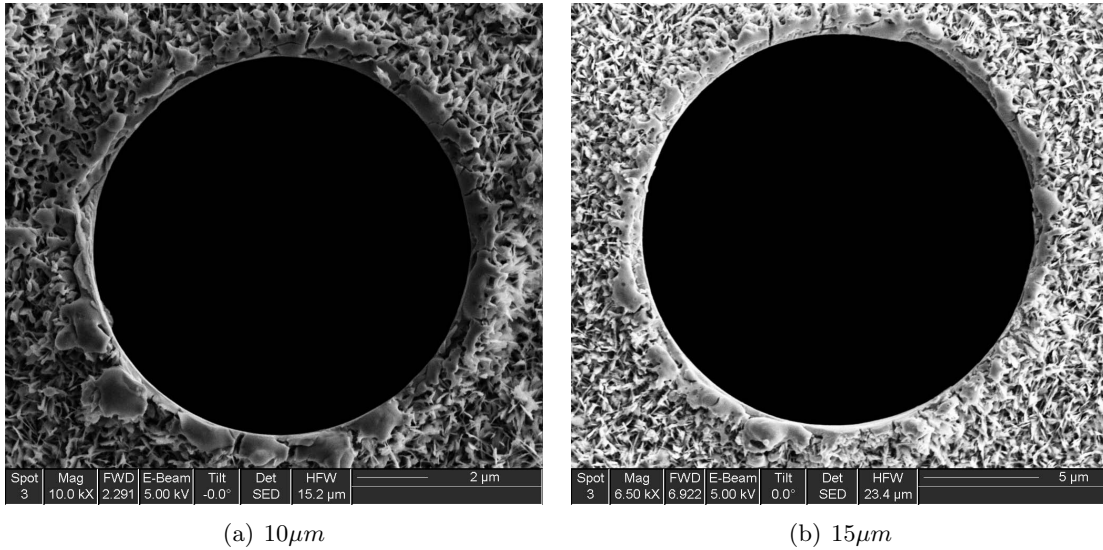
Figure 2.15: SEM micrographs of (a) 10μm and (b) 15μm nominal diameter mounted apertures. Diameters as measured by SEM are $10.6(1)\mu$m and $16.9(2)\mu$m respectively.

The intensity pattern due to the diffraction of light through a circular aperture is described in terms of the first-order Bessel function of the first kind J_1 [49]

$$P(\theta) = P_o \left[\frac{2J_1(kR\sin\theta)}{kR\sin\theta} \right]^2 \quad , \tag{2.27}$$

where R is the radius of the circular aperture. The radially-averaged intensities for both apertures are presented in Fig. 2.16 with the preliminary magnification set to one.

The radially-averaged intensity for the 10μm aperture was fit to Eq. 2.27 with the radius

(a) $10\mu m$ (b) $15\mu m$
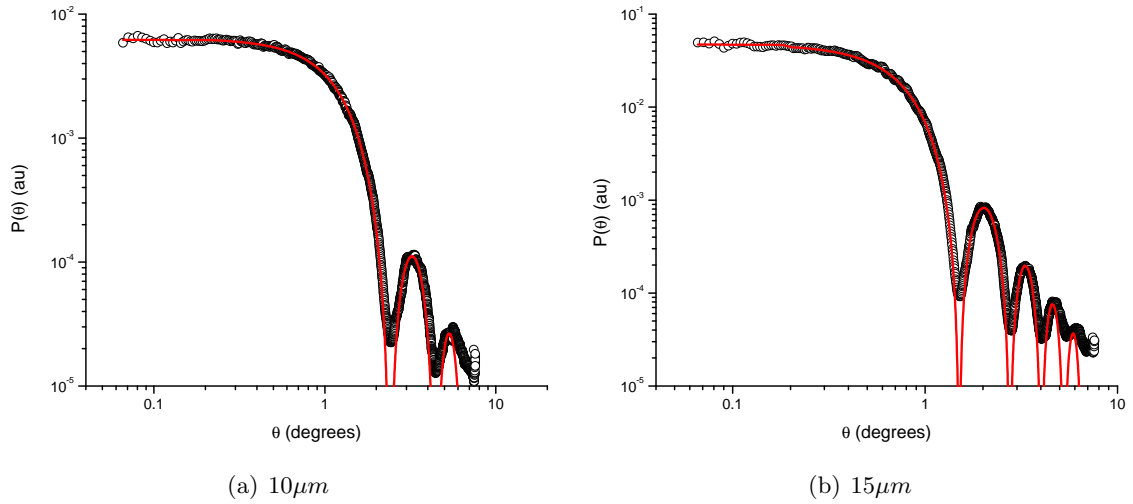
Figure 2.16: Scattering data (circles ○) collected from (a) 10 μm and (b) 15 μm nominal diameter apertures. The curves represent fits of Eq. 2.27 to the data. The magnification is determined from fit to the 10 μm aperture data using the diameter measured using SEM. The fit of the 15 μm nominal diameter aperture data using this magnification results in a determination of its radius.

set to the value measured using the SEM and the scattering angle θ set to (cf. Eq. 2.17)

$$\theta = \arctan\left(\frac{1}{M}\tan(\omega)\right) \quad , \tag{2.28}$$

where ω is the scattering angle for the scattered intensity collected at a magnification of $M = 1$. Fitting the scattered intensity data from the 10 μm using a combination of Eqs. 2.27 and 2.28 reveals that the system magnification is 0.579(6). We do not recover the expected magnification of 1, likely caused by a limiting aperture in the camera optics, that required the camera to be placed closer to the imaging plane than planned to reduce vignetting. The magnification was fixed at 0.579 and the radially-averaged intensity from the 15 μm aperture was fit to Eq. 2.27. The diameter was determined to be 17.0(2) μm, which is consistent with the diameter measured with the SEM.

2.5.3 Polystyrene Spheres

The calibration of the SALS instrument was tested by measuring the scattered intensity of spherical polystyrene latex particles. The particles were 1 μm diameter spheres from

Interfacial Dynamics, and 2 μm and 3 μm diameter spheres from Spherotech. According to the manufacturers' specification, the diameters of these particles are 1.01(4) μm, 2.15(5) μm and 3.17(4) μm as determined by transmission electron microscopy.

These three particles do not satisfy the RGD approximation scattering conditions; the left side of Eq. 2.4 evaluates to 1.91, 4.12, and 6.05 respectively.

The radially-averaged intensity curves for each of the spheres are presented in Fig. 2.17, along with the corresponding fits from Mie scattering calculations. The fits were performed using the Levenberg-Marquardt algorithm on two parameters, the amplitude and the radius.

The diameters of the spherical polystyrene latex particles were determined from these fits to be 1.2(1) μm, 2.08(4) μm and 3.03(5) μm. These values differ from those stated by the manufacturer with at most a 10% discrepancy.
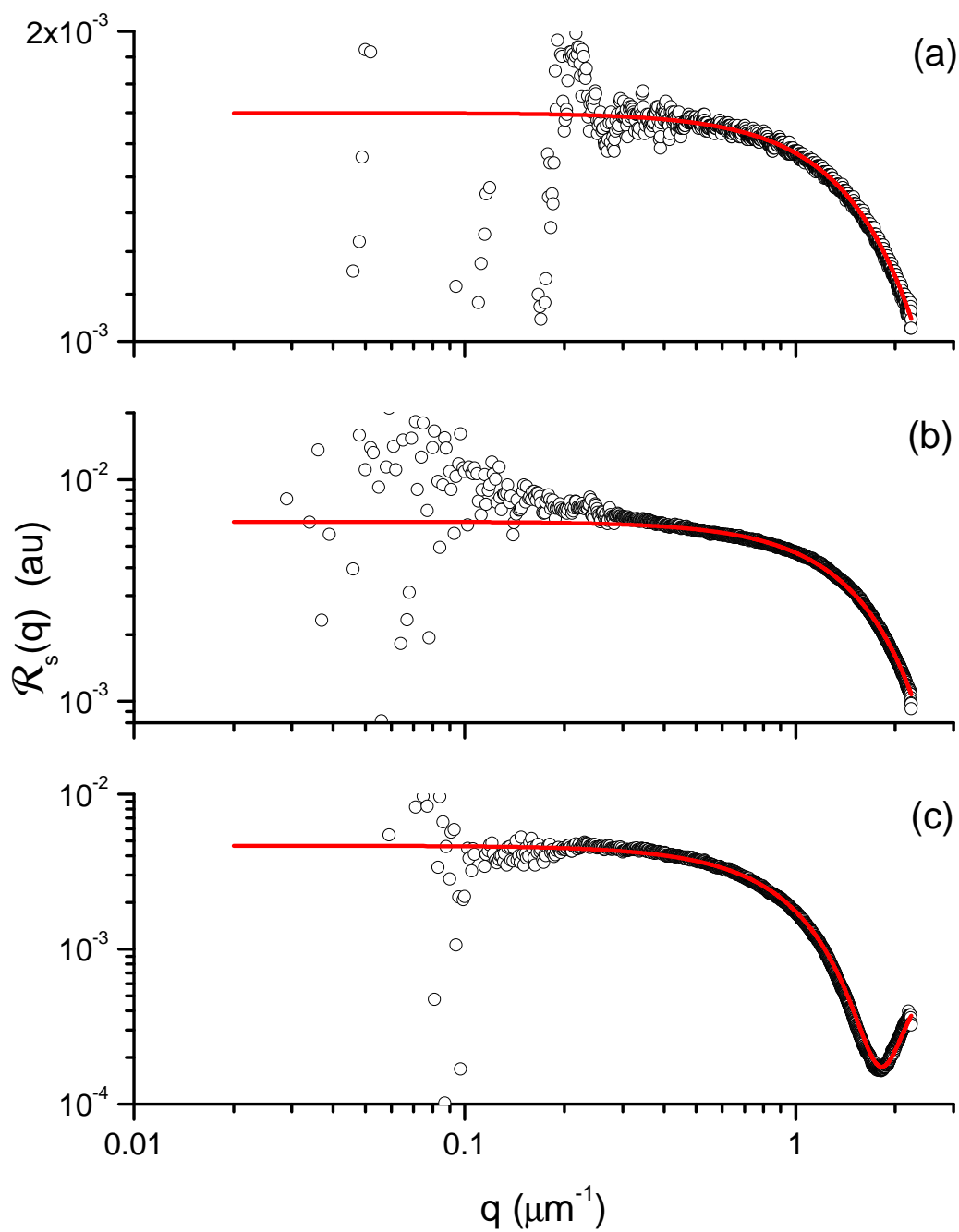
Figure 2.17: Scattering data for polystyrene latex spherical particles (circles ∘) fit to the Mie scattering function form. The diameters of the polystyrene latex spheres were determined to be (a) 1.2(1) μm, (b) 2.08(4) μm and (c) 3.03(5) μm.

Chapter 3

Light Scattering Studies of Carbopol ETD2050

Aqueous polymer dispersions are used extensively as thickeners in consumer and pharmaceutical products to improve their rheological properties [11, 50, 51]. Carbopol, a family of synthetic high molecular weight cross-linked acrylic acid-based polymers developed by BF Goodrich, is a well-known thickener used in personal care, household and industrial products.

The unique chemistry of Carbopol polymers allows them to be used as highly efficient thickeners, adhesives, suspending aids, stabilizers, and controlled release agents. Carbopol exhibits a yield-stress and is often used as a model yield-stress fluid because it is transparent and its rheological properties can be precisely tuned by sample preparation[5].

Much of the study of Carbopol has been geared toward rheological properties [4, 6, 9] with supplementary studies of structure [8, 11]. More general studies of structure and rheology have been performed on poly(acrylic acid), the main component of Carbopol [12, 13]. Structural investigations of Carbopol have typically been made using small-angle neutron scattering. With the understanding that the Carbopol gel particles could possibly be tens to hundreds of microns in size, small-angle light scattering should be an excellent method for probing the long length scale regime.

In this chapter, Carbopol is first introduced in the context of its polymer chemistry. This is followed by a presentation of light scattering results and interpretation.

3.1 Properties of Carbopol

Experiments were performed using Carbopol ETD2050. Easy-to-disperse (ETD) Carbopol products are hydrophobically modified for use in higher electrolyte or surfactant-containing personal-care products [35]. Carbopol ETD2050 consists of high-molecular weight ($>$ $1GDa$) polymers made up of homopolymers of acrylic acid and copolymers of acrylic acid and long-chain (C10-C30) alkyl acrylates crosslinked with a polyalkenyl polyether [2]. Figure 3.1 displays the chemical structures of the individual polymers, and Fig. 3.2 provides a schematic illustration of the polymer crosslinking. It has been reported that the dry Carbopol polymer particles are 0.2μm average diameter with flocculates $2-7\mu$m in diameter [2].

(a) poly(acrylic acid)   (b) poly(alkyl acrylate)   (c) polyalkenyl polyether
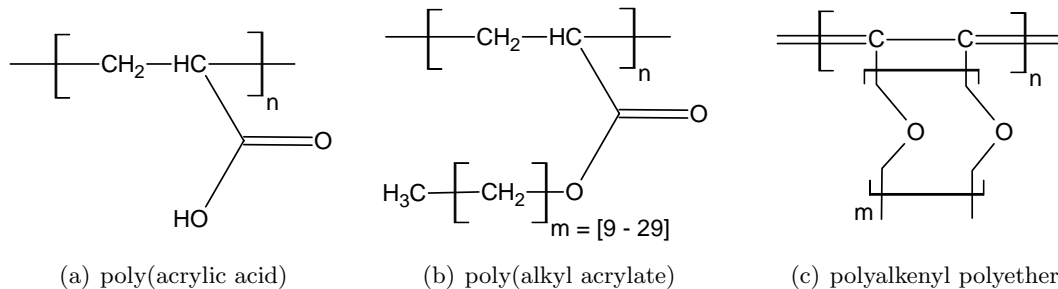
Figure 3.1: (a)Homopolymers of acrylic acid, (b)copolymers of alkyl acrylate and (c)polyalkenyl polyether crosslinker used in the formulation of Carbopol ETD2050.

The carboxylic groups are the principal chemical sites that affect the thickening characteristics. The thickening properties can occur via one of two mechanisms, depending on the dispersing medium [53]: 1) Aqueous solvent dispersion, where neutralization into its appropriate salts causes the polymer to expand, producing a gel-like structure. 2) Non-aqueous polar solvent dispersion, where hydroxyl donors expand the structure via hydrogen bonding.

Experiments performed in this thesis involve aqueous dispersions of Carbopol which are mildly acidic because of the carboxylic groups. When dispersed in an aqueous medium, the carboxylic groups release the hydrogen atom in favour of a resonance hybrid charge [54]. The molar ratio of dissociated carboxylic groups ($-COO^-$) to the associate carboxylic acid groups ($-COOH$) is governed by pH relative to the pKa of the polymer as described by

$$pH - pKa = log\left(\frac{-COO^-}{-COOH}\right) \quad . \tag{3.1}$$

(a) Homopolymer   (b) Copolymer
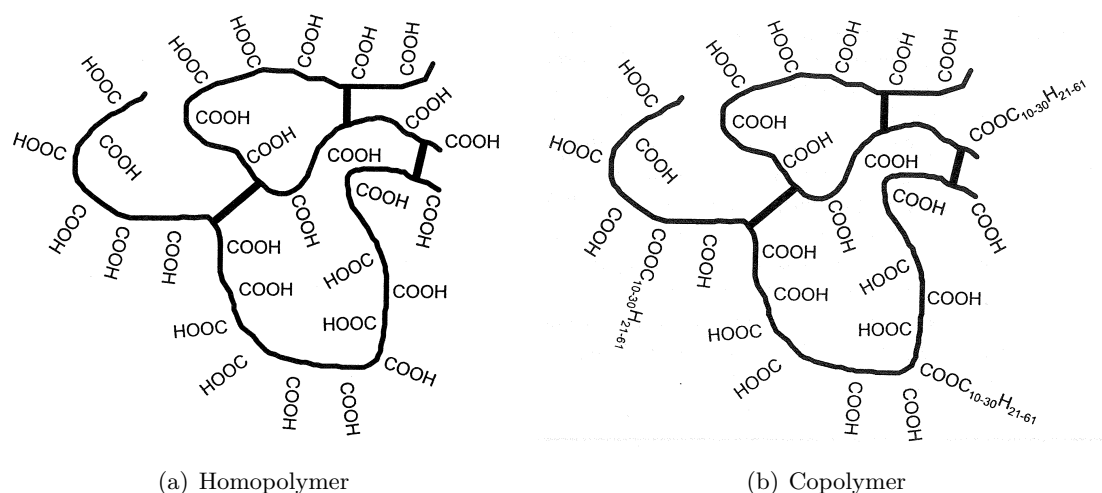
Figure 3.2: Illustration of the polymer structures which make up Carbopol ETD2050. The homopolymer and copolymer are crosslinked with polyalkenyl polyether [52]. The straight segments represent the polymer crosslinker.

When the pH is much smaller than the pKa the associated form is preferred, and for pH much larger than the pKa the dissociated form is preferred. When the pH is equal to the pKa, there are equal portions of dissociated and associated acid forms. The pKa of poly(acrylic acid) is 4.25 [55], while that of Carbopol is reported to be 6.0(5) [2]. Reported changes in rheological properties of Carbopol occur at a pH closer to that of poly(acrylic acid) [2].

The dissociated free hydrogen ions do not disperse homogeneously throughout the sample but instead reside inhomogeneously within the polymer or close by in the aqueous medium. This is characteristic of a Donnan equilibrium, as shown in Fig. 3.3 [2, 56]. The Donnan equilibrium is characterized by a heterogeneous distribution of diffusible ions between two ionic solutions. Consider a two-phase ionic system, in which one charged component is physically restricted to one phase, but ions of any other species can move freely between the two phases. Such a situation can arise when two electrolyte solutions are separated by a semi-permeable membrane or from the inherently immobile nature of one charged component. In either case, an uneven distribution of the diffusible ions over the two phases will develop, as their concentrations adjust to make their electrochemical potentials the same in each phase. This establishes an osmotic pressure difference and an electric potential difference between the phases [57].
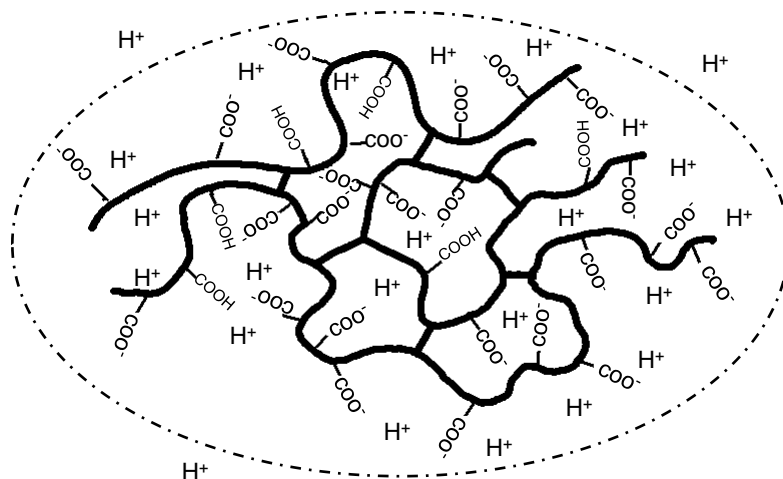
Figure 3.3: Ionic polymers dispersed in an aqueous medium form a Donnan equilibrium. The Donnan equilibrium is characteristic of an inhomogeneous distribution of mobile ions in the system, described by a boundary layer.

When Carbopol is neutralized using an aqueous base, such as sodium hydroxide, the gel particle swells by a factor of up to 10 in diameter; *ie.* a factor of 1000 in volume [2]. Neutralization replaces a free hydrogen cation from the polymer with another free cation, such as sodium if the sample is neutralized with sodium hydroxide. The sodium carboxylate formed as a result remains as a dissociated salt in the aqueous medium. The repulsive force between the negative charges of the carboxyl groups and osmotic pressure from mobile ions cause the structure to swell, as evidenced by the sample thickening during neutralization [2].

3.2   Sample Preparation

Carbopol ETD2050 powder was added, over the course of several hours, to de-ionized distilled water while stirring at $\approx$ 100 rpm. Stirring continued for an additional 12 hours at $\approx$ 50 rpm to ensure that the particulates were dispersed homogeneously and fully swollen. The time required for hydration before neutralization is not a critical factor in the distribution of the particle gel, but the stirring speed is important. Stirring in solution with a stirbar or paddle helps to ensure a homogeneous mixture; however, stirring at high speeds, generally greater than 1000 rpm, during hydration will induce the break-up of the

gel particle [58, 59].

A dispersion containing 5 wt% Carbopol (expressed in grams of dry Carbopol per 100 ml of de-ionized distilled water) was prepared and subsequently diluted to achieve aliquots of 2.0, 1.5, 1.0, 0.5, 0.2, and 0.1 wt%. Aqueous dispersions of Carbopol polymers had pH's in the range of 2.5 to 3.6 depending on the polymer concentration. The greater the concentration, the higher was the carboxylic acid concentration and, therefore, the lower the pH.

For each of the concentrations, smaller aliquots were neutralized to various pH-levels using concentrated 20 wt% aqueous sodium hydroxide (NaOH). This high concentration of NaOH was used to minimize the dilution of the samples. Table 3.1 presents the concentration and pH values of the fifty-seven samples investigated. pH values with an asterix ($*$) in the row are earmarked for concentration comparison in Sec. 3.4.2.

		Concentration ϕ ($wt\%$)				
	0.10	0.20	0.50	1.00	1.50	2.00
						2.62
					2.71	2.69
				2.83	2.79	2.79
			3.02	2.99	2.98	3.01
		3.35	3.36	3.35	3.40	3.35
pH	3.58	3.59	3.61	3.62	3.60	3.62
$*$	3.81	3.81	3.79	3.83	3.78	3.82
$*$	4.31	4.27	4.26	4.25	4.23	4.26
$*$	5.01	5.02	5.02	5.00	4.98	4.98
$*$	6.02	5.99	5.99	6.00	6.00	5.99
$*$	8.02	7.98	8.00	8.07	7.98	8.00
$*$	11.05	11.07	11.00	10.98	11.00	11.05

Table 3.1: Listing of the concentration and pH values for all samples studied. pH values with an $*$ in the row are earmarked for concentration comparison.

3.2.1 Optical Microscopy

Several Carbopol samples were imaged under an optical microscope (Olympus BX51) in both bright-field and phase contrast imaging conditions.

Figure 3.4(a) shows a 40x magnification image of Carbopol grains after the powder was sent through a sieve ($\approx$0.1mm squares). The image shows individual grains ranging in size

between 1 and 2 μm. Aggregates range from 5 to 10 μm and could be as large as 100 μm on account of the size of the sieve.

Figures 3.4(b)-(d) show 2 wt% Carbopol samples imaged with a Ph3 phase contrast filter, bright regions represent a high density, while darker regions represent a low density. The 10x image of un-neutralized Carbopol sample, Fig. 3.4(b) shows cluster-like heterogeneity with sizes of order $\approx$ 20 μm. The 100x image of un-neutralized Carbopol sample, Fig. 3.4(c), shows a magnified view of the centre portion of Fig. 3.4(b) and further illustrates the heterogeneity observed in the brightness contrast image. The 100x image of Carbopol neutralized to pH6, Fig. 3.4(d), shows a very homogeneous density.

(a) Grains of Carbopol @ 40x

(b) 2.0 wt% un-neutralized @ 10x

(c) 2.0 wt% un-neutralized @ 100x

(d) 2.0 wt% neutralized to pH6 100x
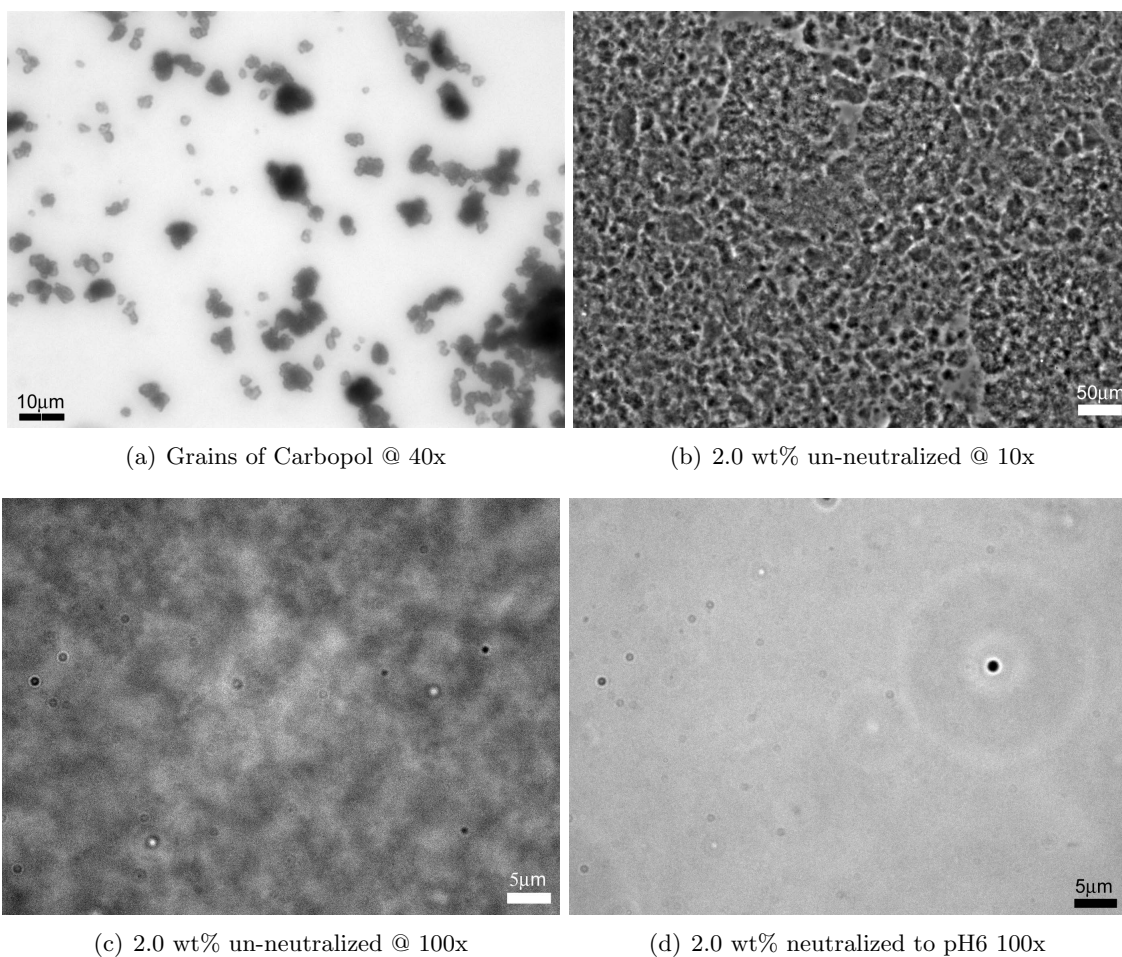
Figure 3.4: Microscope images of (a) dry grains of Carbopol, (b),(c) un-neutralized 2wt% Carbopol and (d) 2wt% Carbopol neutralized to pH6.

3.2.2 Sample Turbidity

The samples prepared as described above showed a noticeable trend in the sample turbidity. A photograph of the 2.0 wt% Carbopol series with increasing pH going from left to right is shown in Fig. 3.5. As the samples are neutralized, the pH increases and the turbidity of the samples decreases.
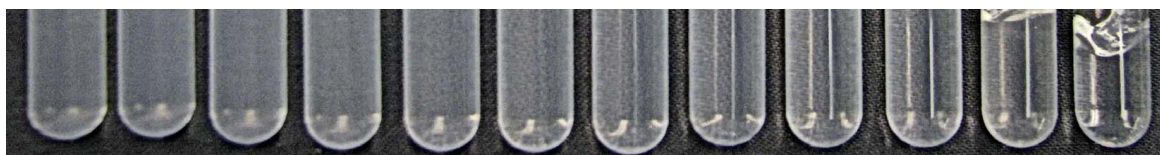
pH $\longrightarrow$

Figure 3.5: Representative effect of pH on the turbidity. Presented are the neutralized samples of $2.0wt\%$ Carbopol, with increasing pH from left to right. As the pH increases, the turbidity of the samples decreases.

3.2.3 Table-top Rheology

Some of the samples, particularly those prepared at low pH, would flow under applied stress, while other samples would not flow but instead showed elastic-like behaviour, indicating that the sample had gelled. A general diagnostic was used to test for gelation. A 25 mm diameter tube containing a 20 g sample was inverted and observed after 5 seconds. Figure 3.6 presents the findings for samples, where the solid bullet ($\bullet$) identifies samples that flowed and the open bullet ($\circ$) identifies samples that did not flow.

Raghavan and Cipriano [60], showed that the yield stress, τ_o, along the long axis of a vertically-oriented cylindrical cell is

$$\tau_o \cong \frac{Mg}{\pi R^2} \quad , \tag{3.2}$$

where M is the mass of the sample, R is the radius of the cylinder and g is the gravitational acceleration. This condition originates from the von Mises yield criterion for static equilibrium balances the yield-stress with the gravitational stress.

For our geometry, $M = 20$ g, $R = 12.5$ cm, and $\tau_o \cong 4$ Pa. From this we estimate that the samples that flowed have $\tau_o < 4$ Pa, while samples that did not flow have $\tau_o > 4$ Pa.
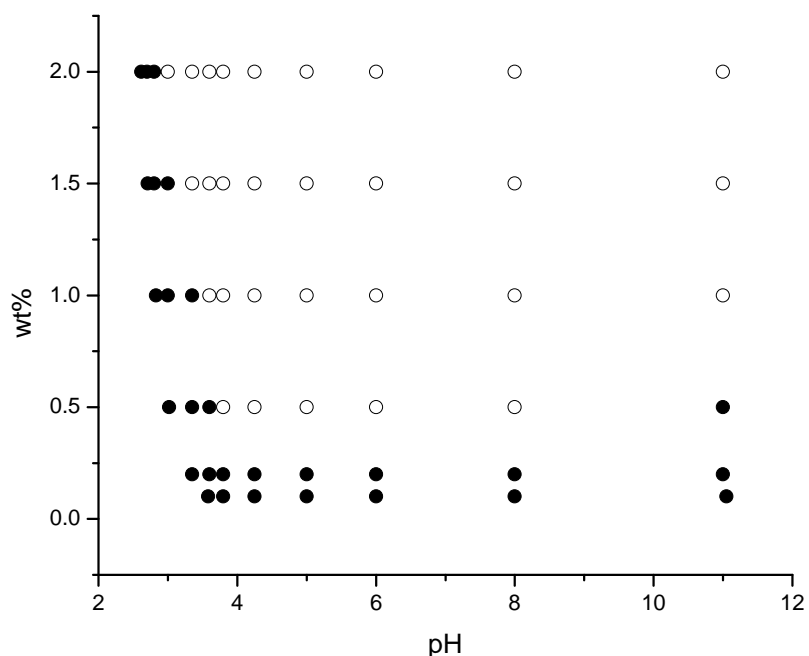
Figure 3.6: Tabletop rheology results for samples in a 25 mm diameter tube. Samples that flowed are denoted by • and samples that did not flow are denoted by ∘.

We can compare this to the yield stress of several consumer products: ketchup at 15 Pa, mayonnaise at 100 Pa, and hair gel at 135 Pa [7].

The observation of flow for a Carbopol sample at 0.5 wt% at low pH values and at pH 11, is reminiscent of the viscosity behaviour for Carbopol. Figure 3.7 provides an illustration of the viscosity of a 0.5 wt% sample of Carbopol 941 measured at 20 rpm based on information provided by the manufacturer [2]. Carbopol 941 is formulated similarly to Carbopol ETD2050 and provides an excellent reference for rheology. Literature states that at low- and high-pH, the viscosity greatly smaller than the viscosity at ph 7. This can be explained in the context of polymer swelling. At low-pH the polymers are tight and small, and can flow pass eachother. When swollen, such as at pH 7, the polymers interact and entangle and their motion of the polymers are jammed resulting in little flow. However at high-pH, the polymers become fully extended and lose their elastic behaviour, and their structure is very vacuous enabling for the easy flow of polymers.
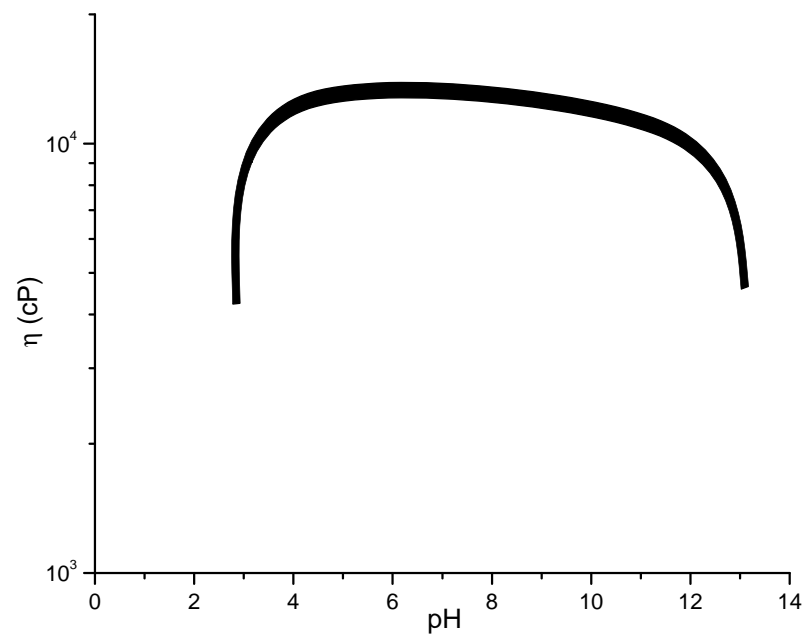
Figure 3.7: An illustration of the viscosity of a 0.5 wt% sample of Carbopol 941 (akin to Carbopol ETD2050) measured at 20 rpm based on information provided by the manufacturer [2].

3.3 Scattering Experiments

All measurements were made using a combination of two instruments, the SALS and the commercial ALV-5000/e DLS/SLS light scattering instrument (ALV Gmbh). This combination provides scattering angles ranging from $0.08 - 150°$ which translates into a scattering q range of $0.02 - 25$ μm^{-1}, over 3 decades in q. Carbopol samples at higher concentrations and/or pH exhibit non-ergodic behaviour where time averaging fails to fully represent the ensemble statistics. Because of this property, a cuvette rotation unit was used for all samples for static light scattering measurements performed in the ALV. By rotating the sample, we are able to collect information from a large number of spatial orientations, thus performing an ensemble average. Sample rotation in the SALS was not necessary since averaging of all pixels associated particular scattering angle accounts for the ensemble average.

Merging the scattering curves from both instruments involves applying an overall multiplicative constant to account for differences in the collection optics, detector, geometry, etc. This constant was determined by matching the scattering curves obtained from the two instruments for the un-neutralized samples. The multiplicative constant may be different between concentration series, but is kept constant for each sample in a concentration series. The Rayleigh ratio provided by the ALV is a measure of $I_{sample}/(f \cdot I_o)$, where f is an instrumental constant. Comparing Eq. 2.25 to $I_{sample}/(f \cdot I_o)$, a term not accounted for is the contribution from turbidity. Therefore neutralized samples measured on the ALV were also scaled with the sample turbidity relative to the un-neutralized sample as measured in the SALS instrument. Turbidity corrections in SALS measurements are applied during data collection.

3.4 Scattering Results

The scattering results are presented in two formats: the scattering curves for all pH values at particular concentrations, and the scattering curves for all concentrations at particular pH values marked by $*$ in Table 3.1. All of the scattering curves are presented with data from both the SALS and the ALV instrument. The data shown in the q-range from ≈ 0.02 to ≈ 2 μm^{-1}, was taken with the SALS instrument and the data in the q-range from ≈ 3 to ≈ 25 μm^{-1} was taken with the ALV light scattering instrument.

3.4.1 Scattering for Each Concentration as a Function of pH

The scattering data for each sample concentration as a function of the scattering vector q as the pH is varied from ≈ 3 to 11 are presented in Figs. 3.8 through 3.13. Lines are drawn on the graphs to designate power law slopes as a guide to the eye.

The scattering data for the 0.1 wt% Carbopol are presented in Fig. 3.8. The amount of scattering decreases as q increases. The scattering also decreases as the pH increases, with the main decrease occuring at pH values between 3.8 and 4.3, after which the level of scattering remains approximately constant. In the large-q regime, the scattering exhibits power-law behaviour, with not one but two exponents. With increasing pH, the second power-law scattering term (implying a second scattering length scale) becomes more evident. This observation leads to the identification of two length scales in these samples, with a larger length-scale at $q \approx 0.2 \ \mu\mathrm{m}^{-1}$ and a smaller length-scale at $q \approx 3 \ \mu\mathrm{m}^{-1}$.

As the concentration is increased to 0.2 wt%, 0.5 wt%, and 1.0 wt% Carbopol, as shown in Figs. 3.9 - 3.11 respectively, the similar behaviour is observed except that the small-q scattering feature weakens and shifts to smaller values q ($\approx 0.09 \mu m^{-1}$, $\approx 0.06 \mu m^{-1}$, and $\approx 0.04 \mu m^{-1}$ respectively). This indicates that the associated length scale is increasing with concentration.

At concentrations of 1.0 wt%, 1.5 wt%, and 2.0 wt% Carbopol as shown in Figs. 3.11 - 3.13, we notice that the scattering curves do not merge into a pH-independetn regime above pH 4, as was the case for lower concentrations. Instead they continue to decrease in relative intensity as the pH is increased. At pH values above 4, a saddle can be observed in the scattering curves at $q \approx 0.6 \mu m^{-1}$, with the deepest plateau occuring at $1.0 wt\%$ and above pH 7.

Figure 3.8: Relative intensity of light scattered $\mathcal{R}_s$ as a function of scattering wavevector q for 0.1 wt% Carbopol ETD2050 neutralized with NaOH.
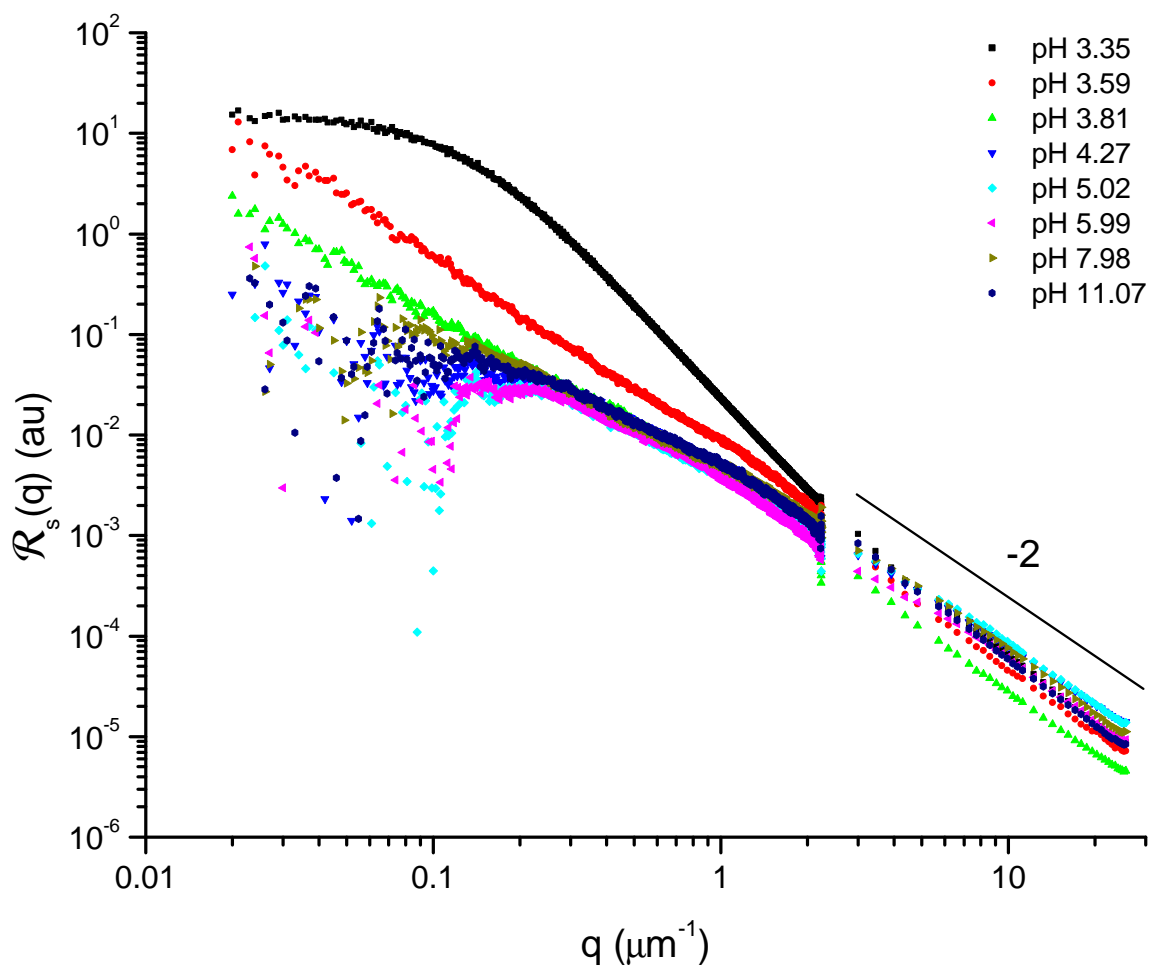
Figure 3.9: Relative intensity of light scattered $\mathcal{R}_s$ as a function of scattering wavevector q for 0.2 wt% Carbopol ETD2050 neutralized with NaOH.
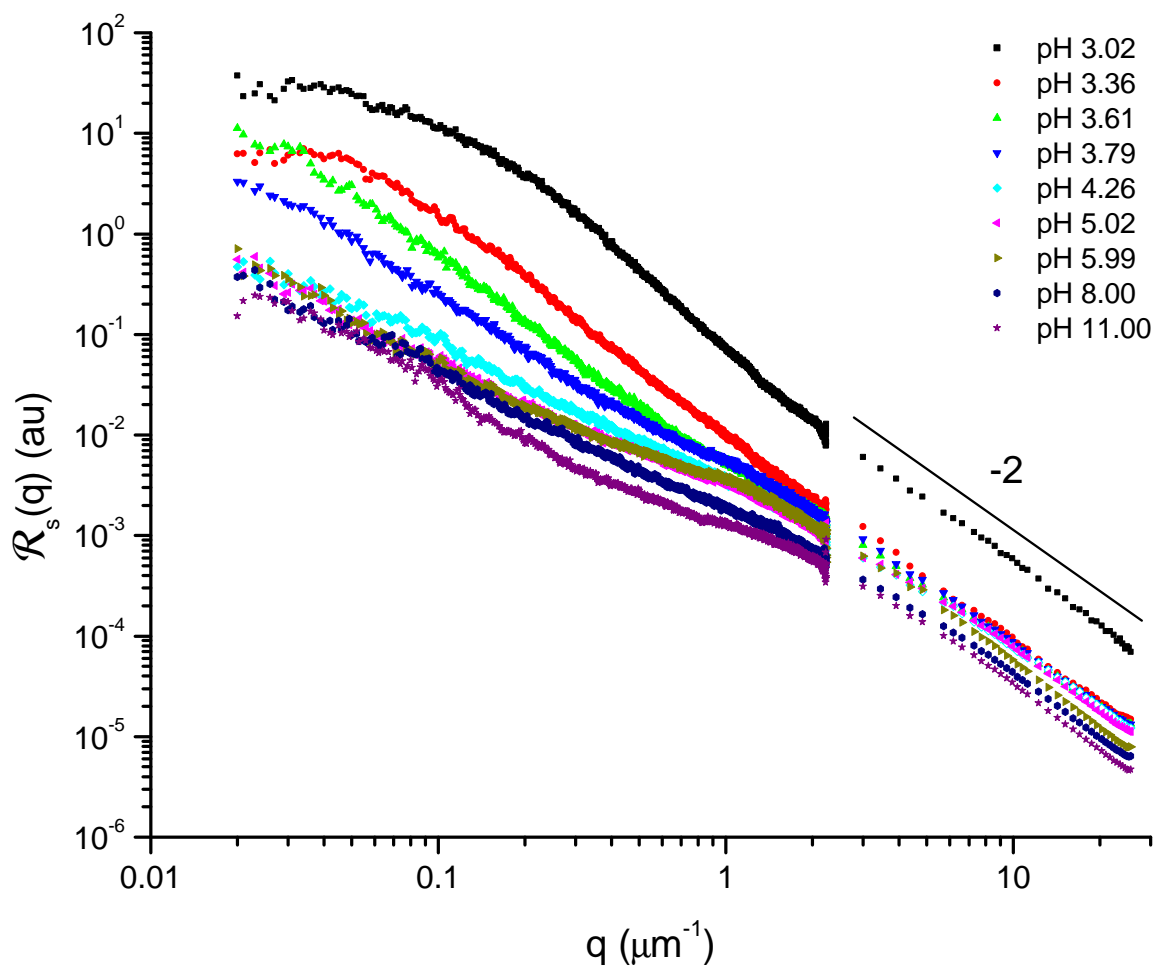
Figure 3.10: Relative intensity of light scattered $\mathcal{R}_s$ as a function of scattering wavevector q for 0.5 wt% Carbopol ETD2050 neutralized with NaOH.

Figure 3.11: Relative intensity of light scattered $\mathcal{R}_s$ as a function of scattering wavevector q for 1.0 wt% Carbopol ETD2050 neutralized with NaOH.

Figure 3.12: Relative intensity of light scattered $\mathcal{R}_s$ as a function of scattering wavevector q for 1.5 wt% Carbopol ETD2050 neutralized with NaOH.

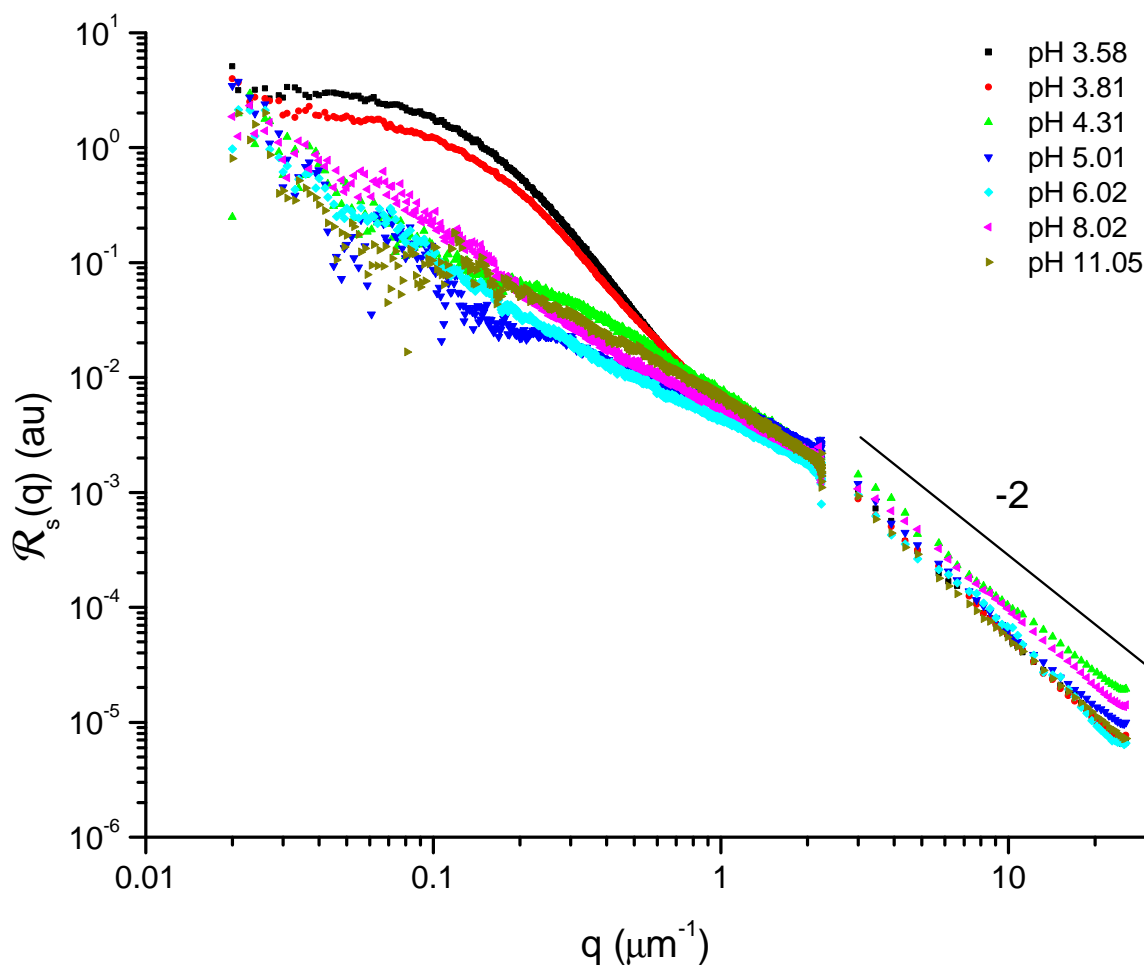Figure 3.13: Relative intensity of light scattered $\mathcal{R}_s$ as a function of scattering wavevector q for 2.0 wt% Carbopol ETD2050 neutralized with NaOH.

3.4.2 Scattering from Samples of Similar pH with 0.1≤ c ≤2.0

The scattering data for samples with different concentrations but roughly the same pH are compared in Figs. 3.14 through 3.20. The vertical axis shows the concentration scaled Rayleigh scattering ratio scaled of the sample. Lines are drawn on the graphs to designate approximate power law slopes where appropriate.

The data corresponding to the un-neutralized samples are shown in Fig. 3.14. These data span a range of pH. The observed small-q ($\approx 0.2~\mu$m^{-1}) change in relative intensity does not appear to vary much as concentration is varied. For concentrations greater than $1.0wt\%$, the small-q region exhibits a power law exponent of about -2. In the large-q region, the scattering data also exhibits power law exponent of about -2.

NaOH was added to all of the samples. A pH of ≈ 3.8 is the lowest possible pH common to data spanning the full range of concentrations, as shown in Fig. 3.15. Evidence of the larger length-scale is not observable for concentrations above 0.1 wt%. However, a smaller length-scale is observable, as evident from a change in the relative scattering intensity, for concentrations larger than 0.1 wt%. The second scattering feature becomes more prominent with increasing pH. For concentrations above 0.1 wt%, the small q region also exhibits power law exponent of about -2.

For pH values of ≈ 4.25, ≈ 5.00, ≈ 6.00, ≈ 8.00, and ≈ 11.00 as shown in Figs. 3.16 through 3.20, evidence of the smaller length-scale is observable for concentrations larger than $0.5wt\%$. The smaller length-scale feature becomes more prominent with increasing pH. The overall scattering profile exhibits a small-q power law exponent of about -2 and a large-q power law exponent of about -2, joined by a transition with a lower power law exponent.

Figure 3.14: Concentration scaled relative intensity of light scattered $\mathcal{R}_s$ as a function of scattering wavevector q for un-neutralized Carbopol ETD2050.

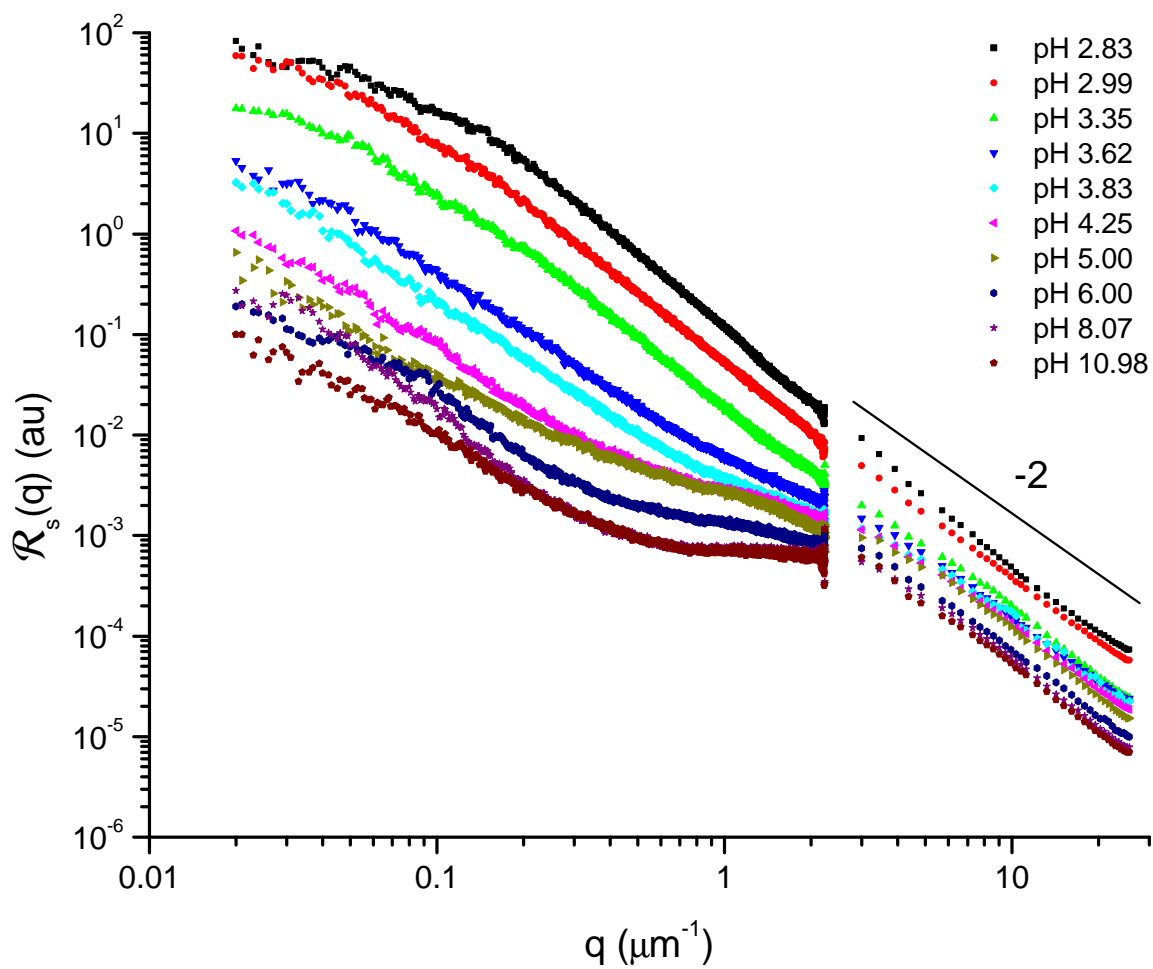Figure 3.15: Concentration scaled relative intensity of light scattered $\mathcal{R}_s$ as a function of scattering wavevector q for Carbopol ETD2050 neutralized to $\approx$pH 3.8.
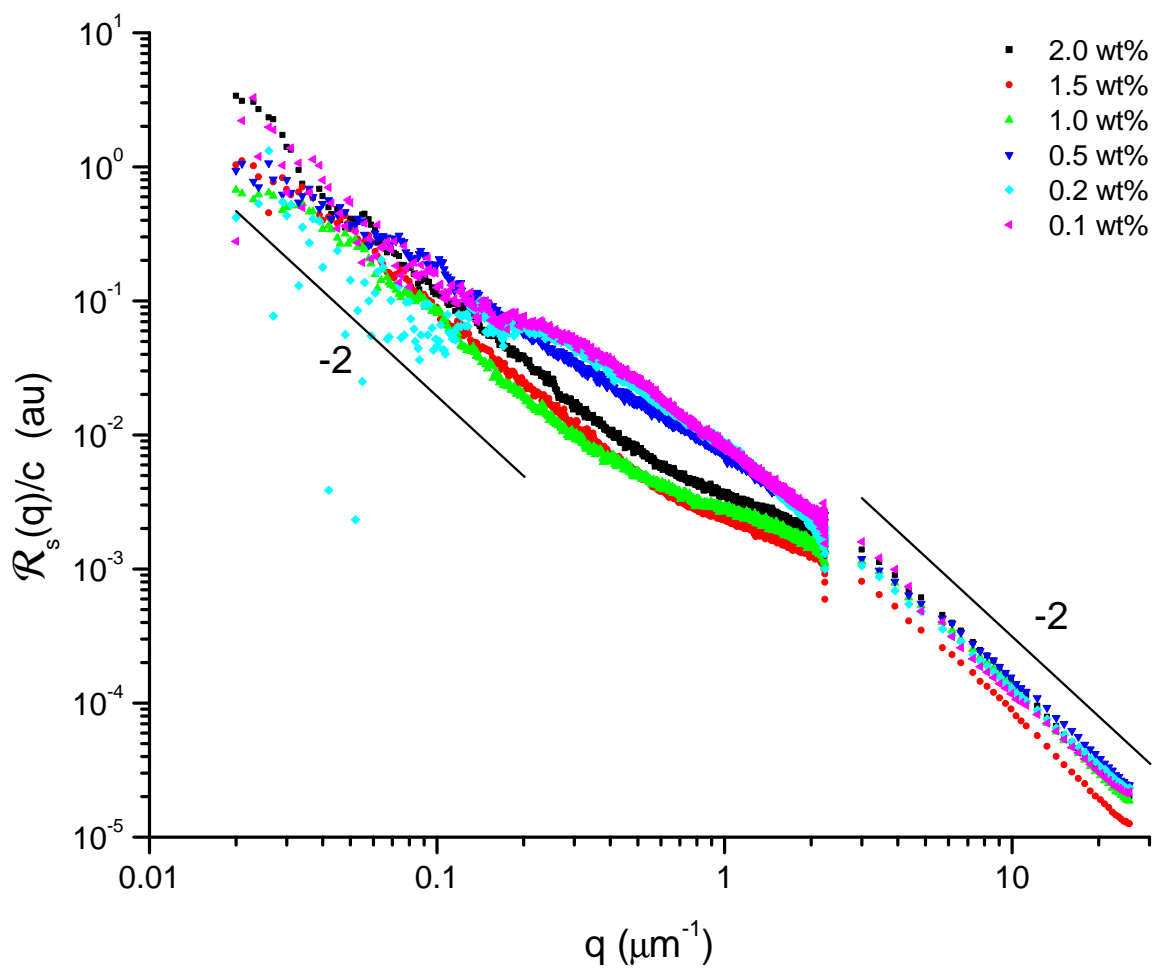
Figure 3.16: Concentration scaled relative intensity of light scattered $\mathcal{R}_s$ as a function of scattering wavevector q for Carbopol ETD2050 neutralized to $\approx$pH 4.25.
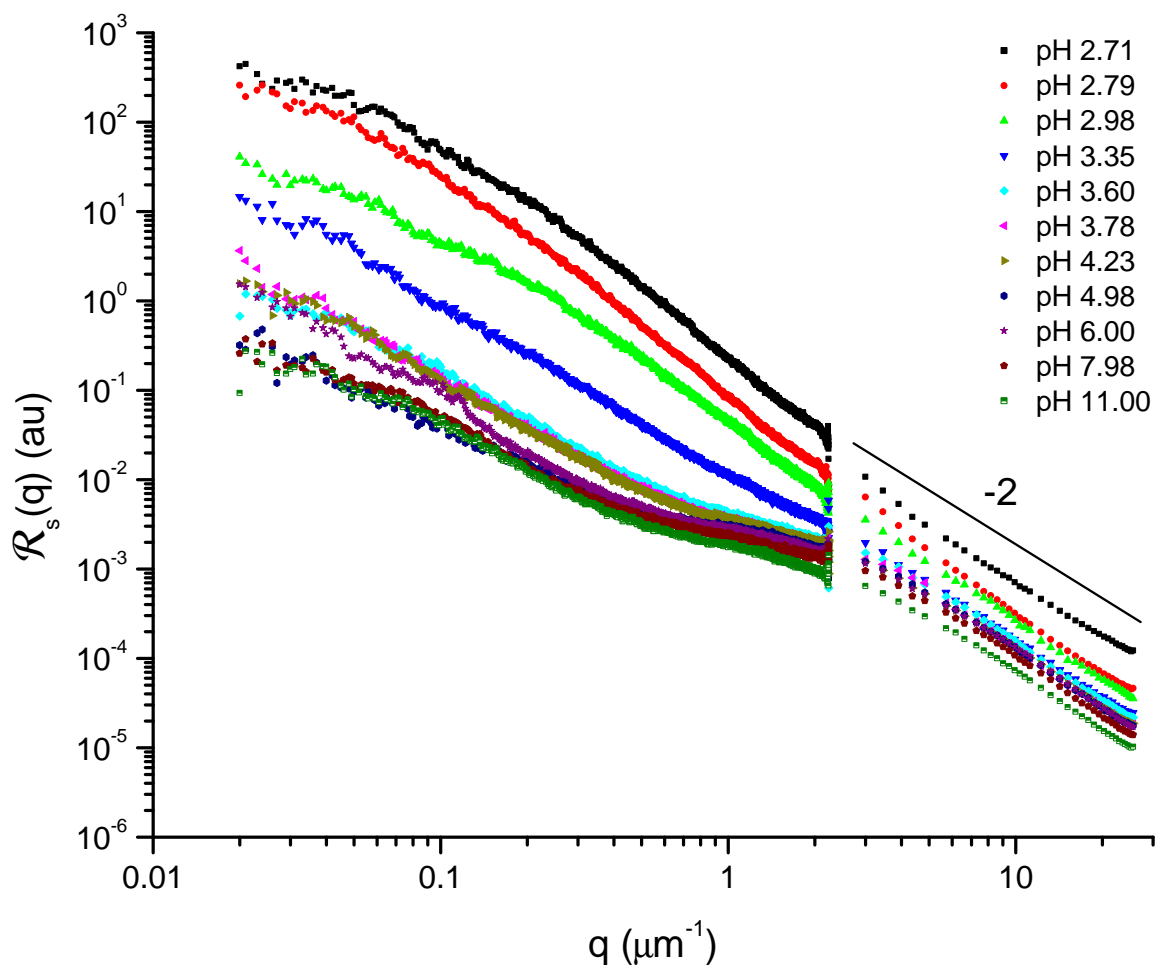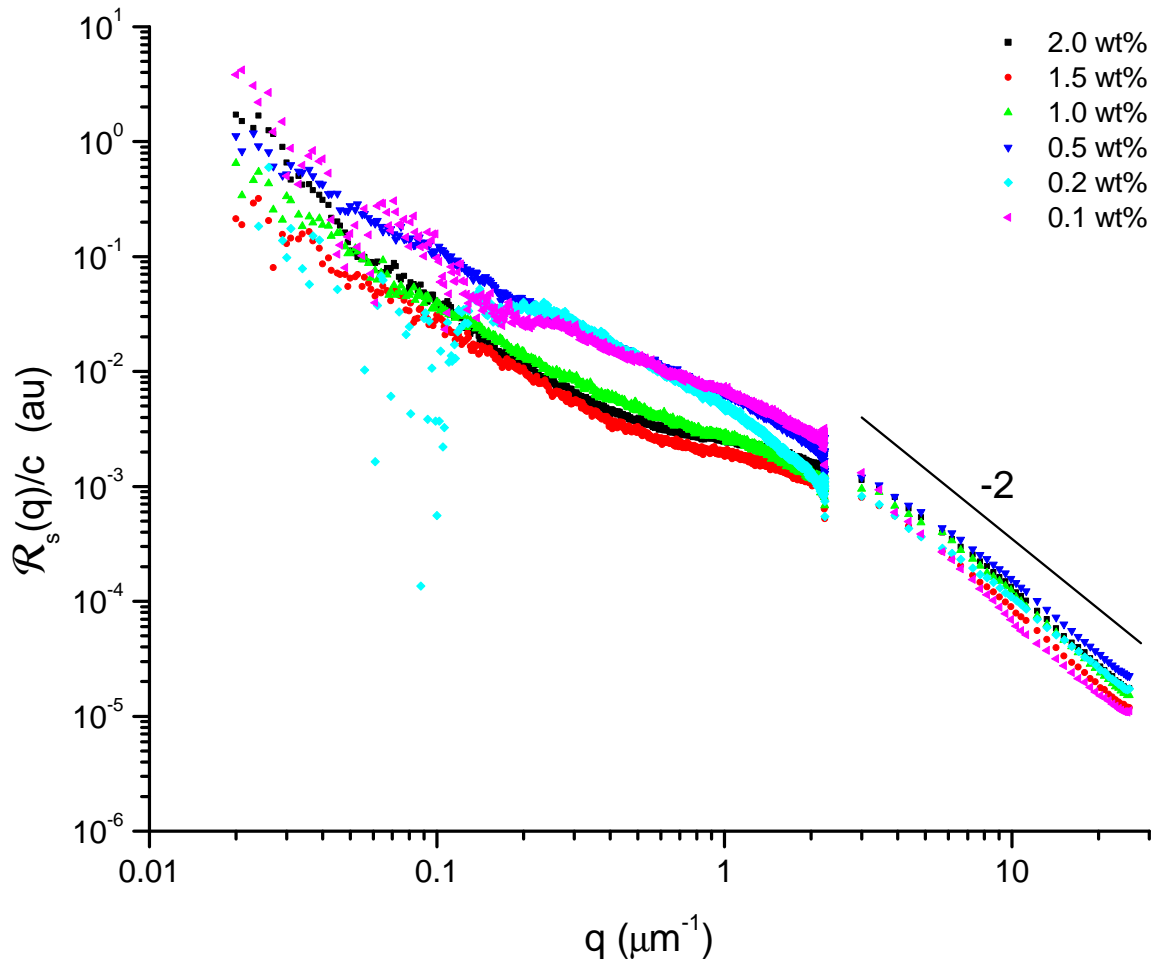
Figure 3.17: Concentration scaled relative intensity of light scattered $\mathcal{R}_s$ as a function of scattering wavevector q for Carbopol ETD2050 neutralized to $\approx$pH 5.0.
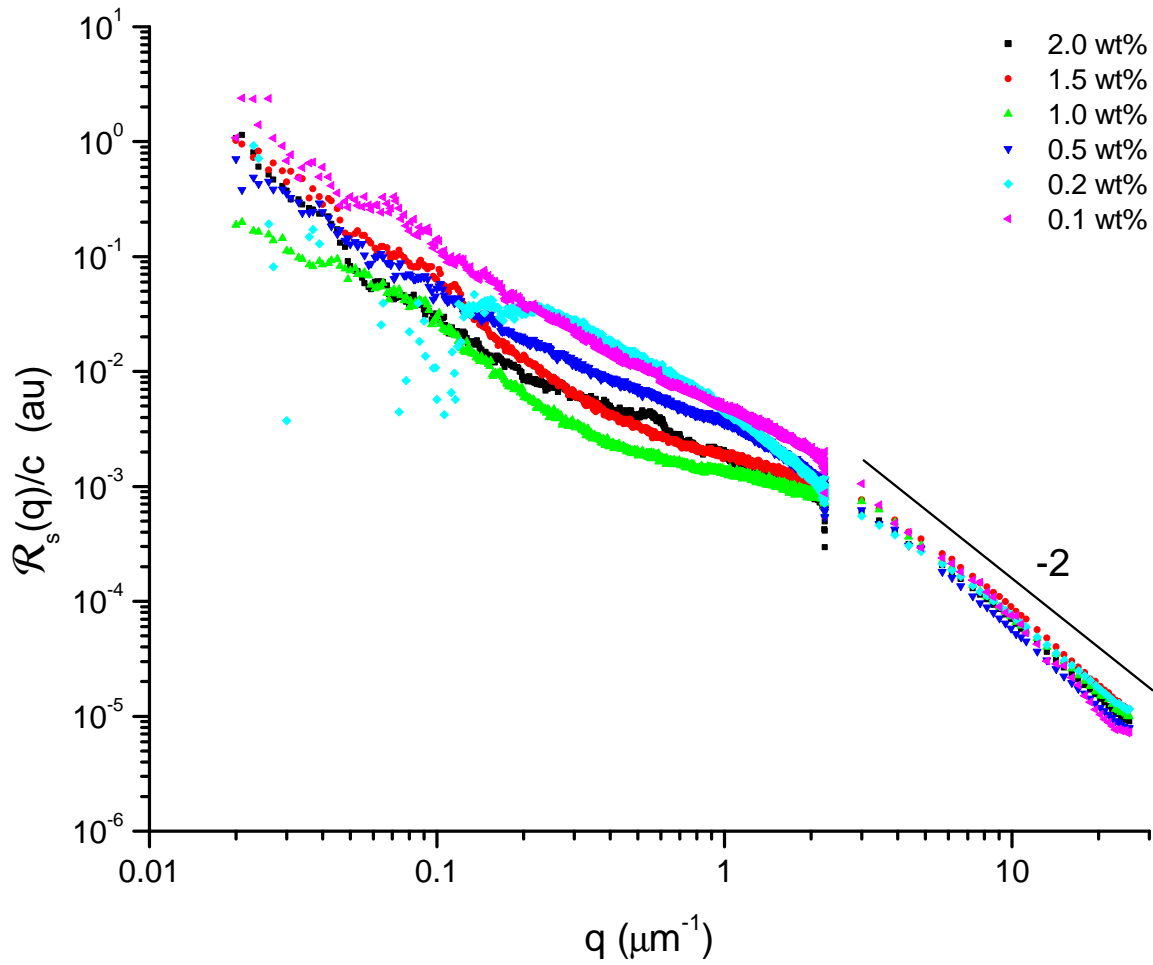
Figure 3.18: Concentration scaled relative intensity of light scattered $\mathcal{R}_s$ as a function of scattering wavevector q for Carbopol ETD2050 neutralized to $\approx$pH 6.0.
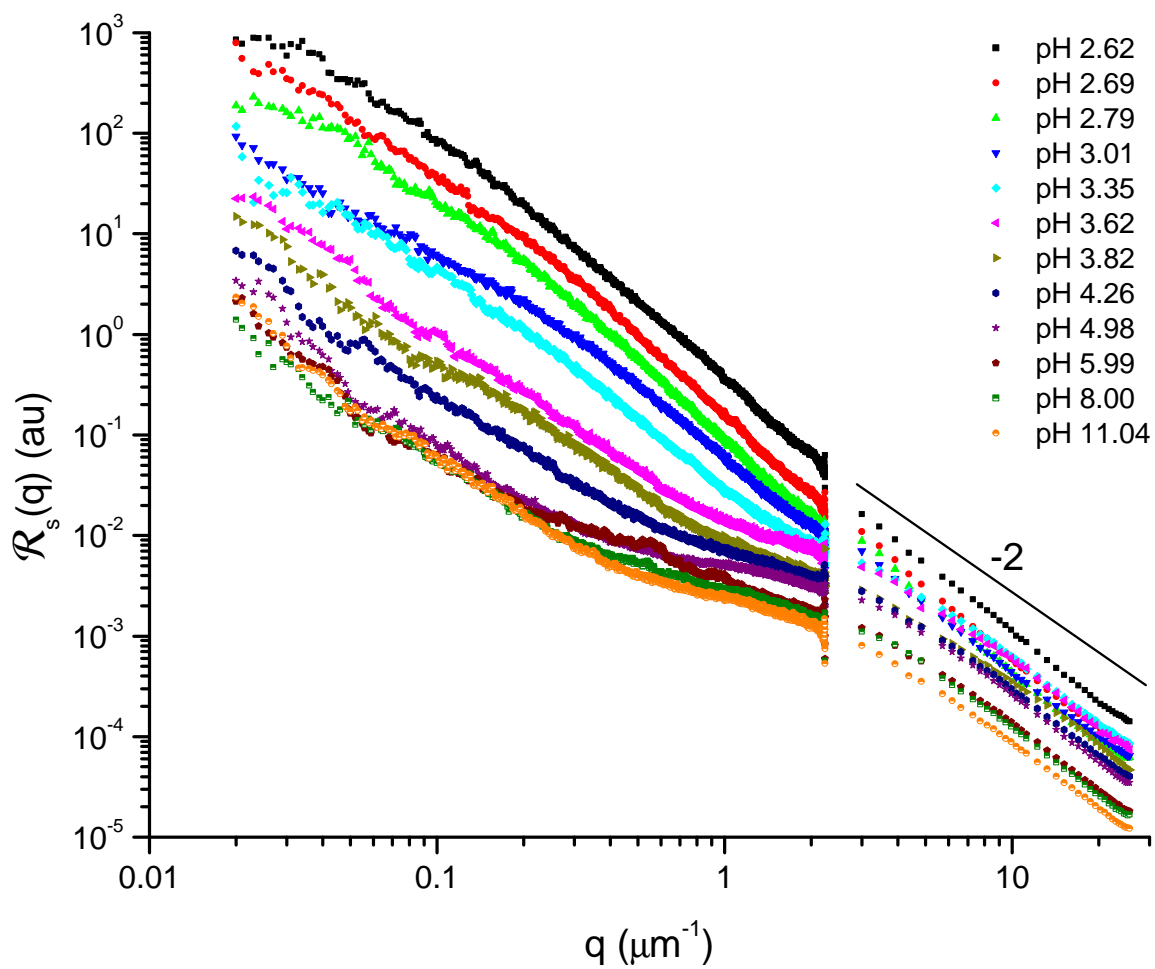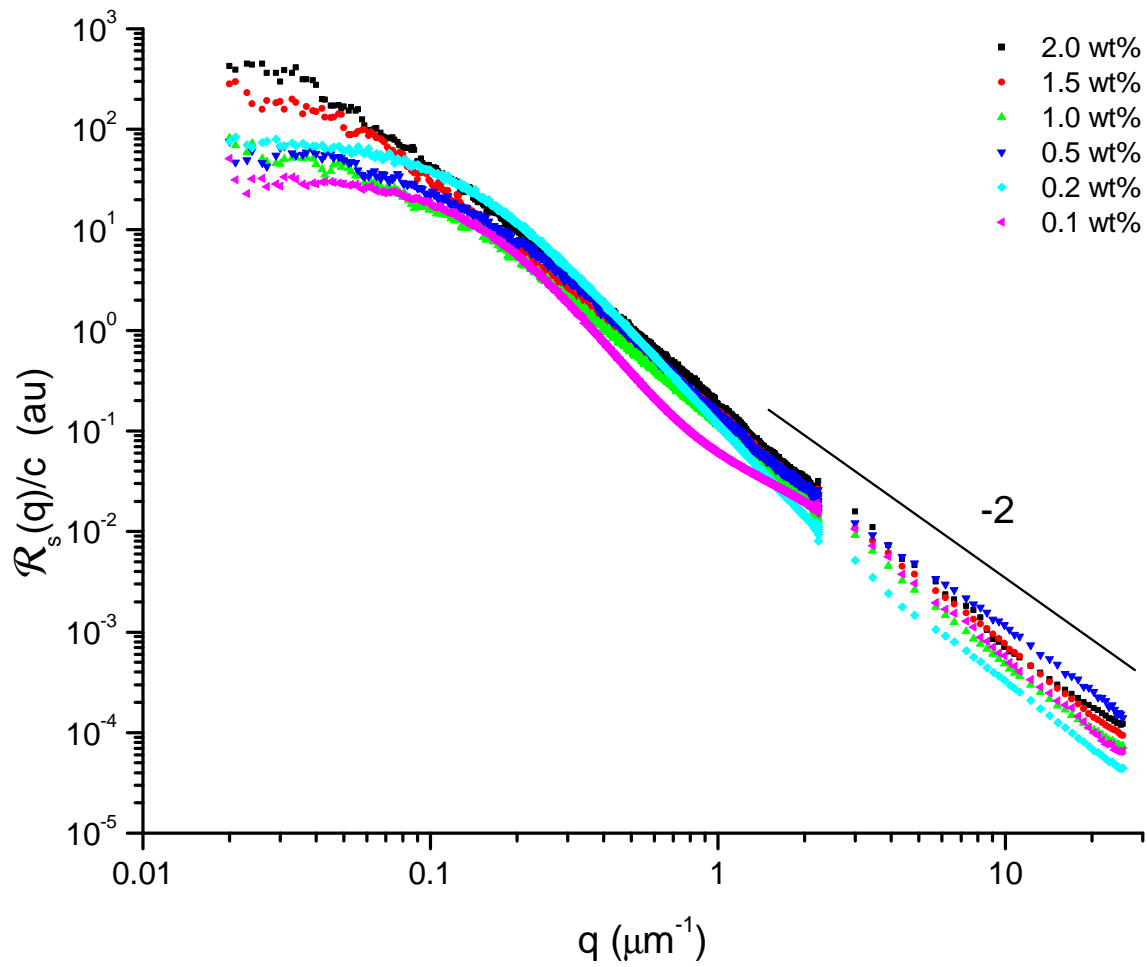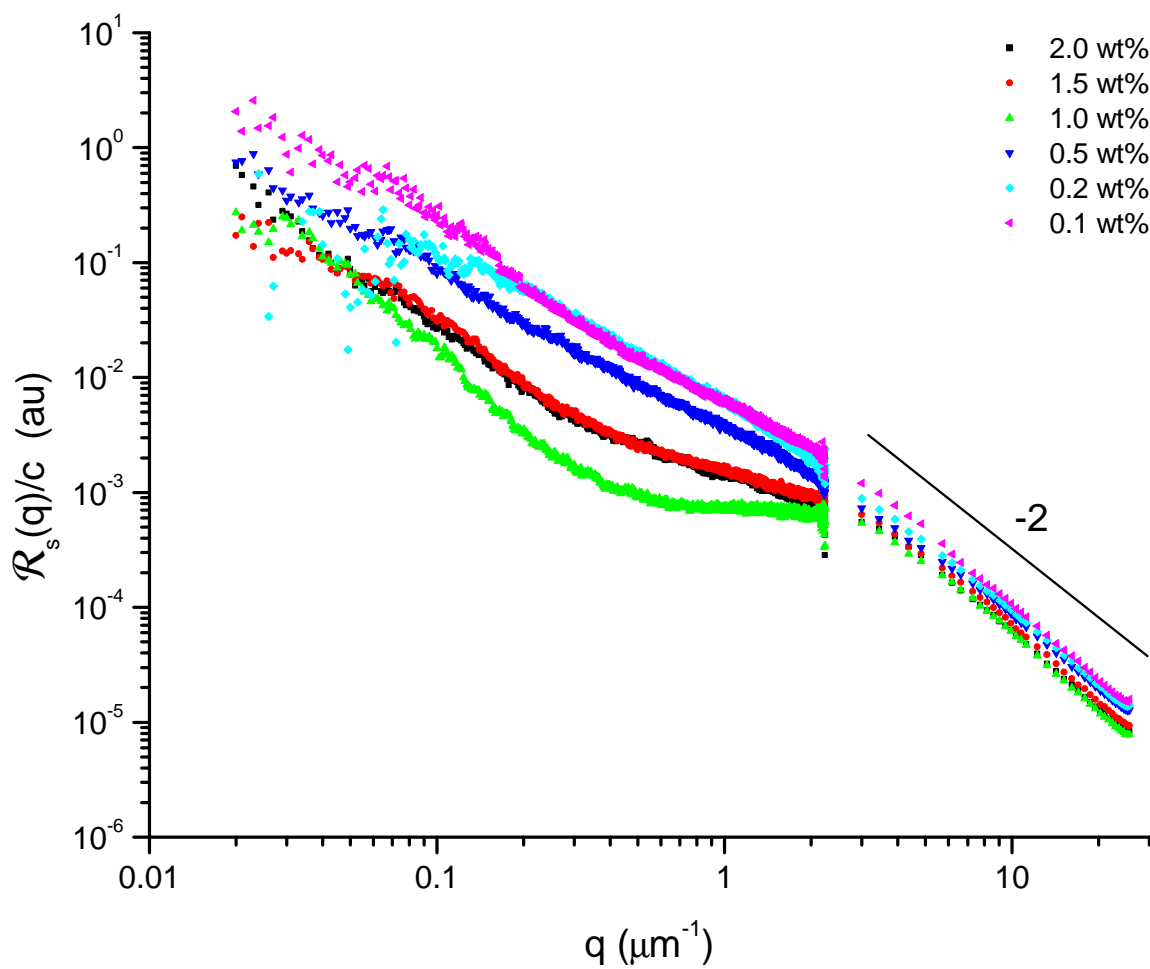
Figure 3.19: Concentration scaled relative intensity of light scattered $\mathcal{R}_s$ as a function of scattering wavevector q for Carbopol ETD2050 neutralized to $\approx$pH 8.0.
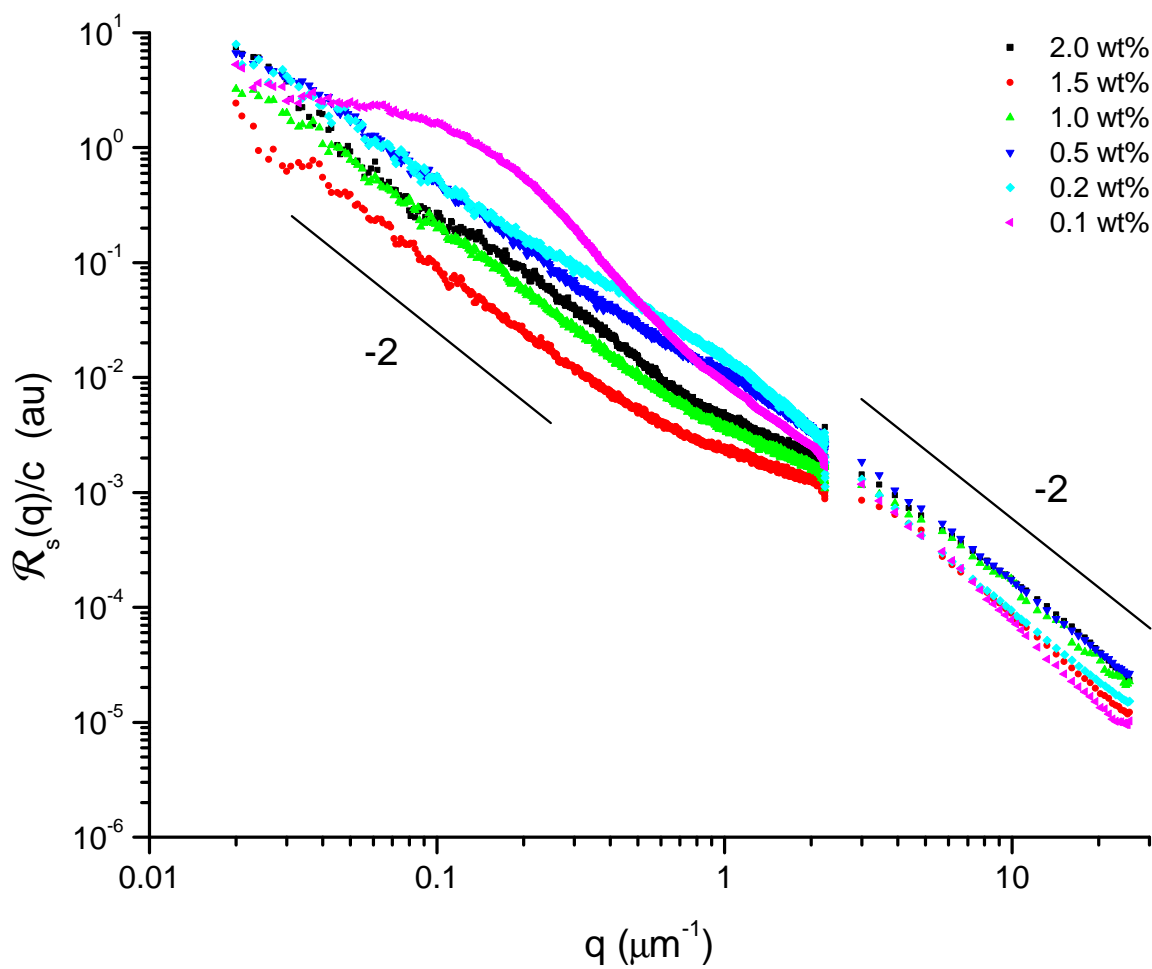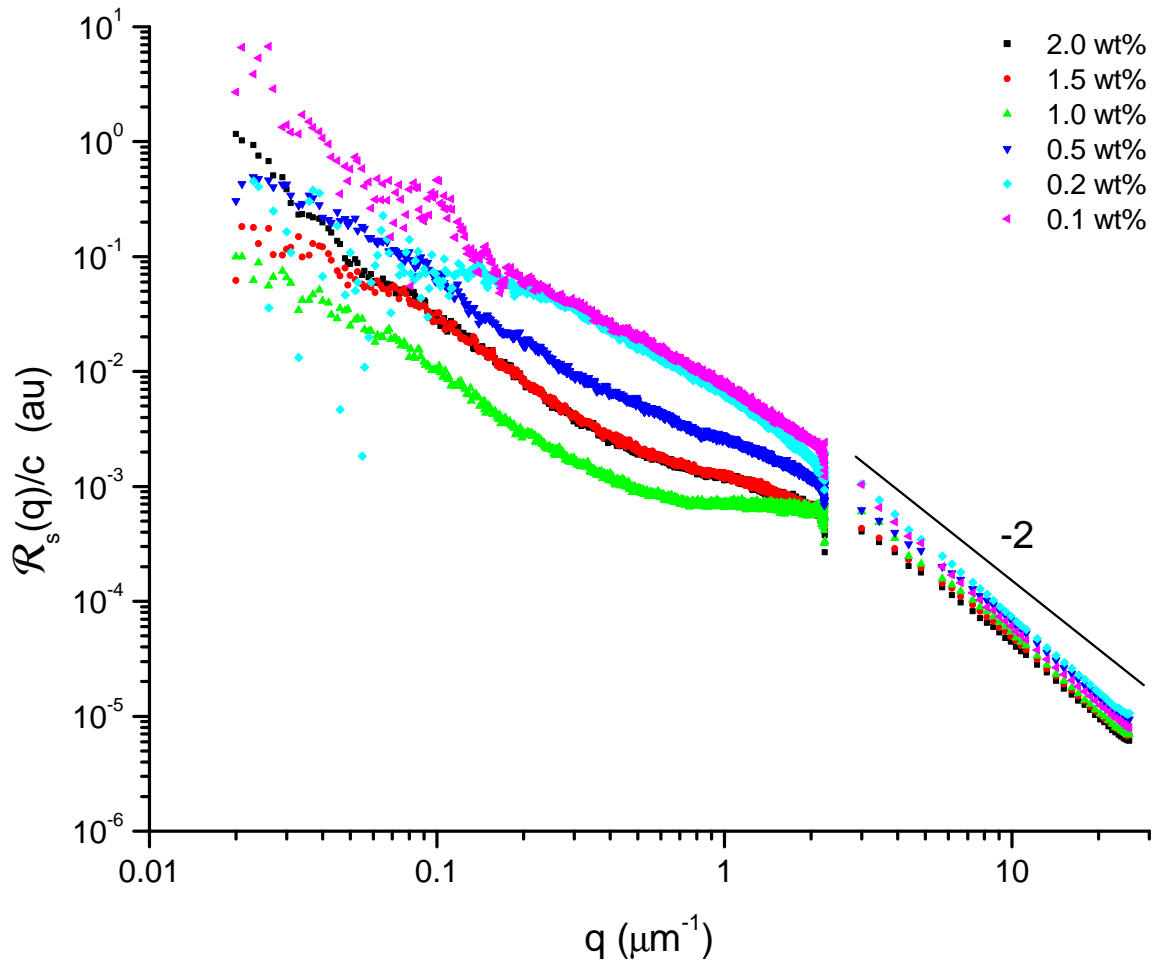
Figure 3.20: Concentration scaled relative intensity of light scattered $\mathcal{R}_s$ as a function of scattering wavevector q for Carbopol ETD2050 neutralized to $\approx$pH 11.0.

3.5 Interpretation of Scattering Results

For fractal or aggregate systems, such as Carbopol, the mass of the object $M(r)$ scales as r^{D_f}, and the correlation function is written as [61]

$$G(r) = A \, e^{-r/\xi} \, r^{D_f - 3} \quad , \tag{3.3}$$

where A is a normalization constant, D_f is the fractal dimension, which must be less than or equal to the dimensionality of the system, and ξ is the characteristic size of the scatterer. The cutoff function, $e^{-r/\xi}$, is constant for $r \ll \xi$ and rapidly falls to zero when $r \gg \xi$. The fractal dimension D_f is a mathematical quantity that describes how the fractal structure fills space: the higher the fractal dimension, the more compact the structure. Table 3.2 presents several mass-fractal dimensions found in scattering experiments [62].

Mass-fractal structure	Fractal dimension
Excluded volume polymer	1.67
Ideal polymer (Θ solvent)	2.00
Collapsed polymer	3.00
Swollen branched polymer	2.00
Randomly branched polymer	2.29
Diffusion limited cluster aggregate (Cluster-Cluster)	1.80
Reaction limited cluster aggregate	2.10
Diffusion limited aggregate (Particle-Cluster)	2.50

Table 3.2: Several examples of mass-fractal dimensions found in scattering experiments.

The structure factor $S(q)$ is the Fourier transform of the correlation function $G(r)$. For a homogeneous and isotropic dispersion, $S(q)$ depends only on the magnitudes of $\mathbf{q}$ and $\mathbf{r}$. Thus,

$$S(q) = 4\pi \int_0^\infty G(r) \frac{\sin(qr)}{qr} r^2 dr \quad . \tag{3.4}$$

Substituting Eq. 3.3 into Eq. 3.4 and completing the integration, we obtain [61],

$$S(q) = \frac{S_o}{(1 + q^2 \xi^2)^{(D_f - 1)/2}} \frac{\sin((D_f - 1) \arctan(q\xi))}{(D_f - 1) q\xi} \quad , \tag{3.5}$$

where S_o is a scalar amplitude.

At small-q, the value of the structure factor $S(q)$ is approximately constant, $S(q \to 0) = S_o$, which indicates that there are spatial fluctuations on all length scales. At large-q, $S(q)$ falls off with power-law behaviour, q^{-D_f}. The transition between these two limits occurs at $q \approx 1/\xi$. The characteristic length scale ξ indicates the extent of the correlated regions, and roughly corresponds to the size of regimes such as the randomly distributed particles or random density fluctuations. The corresponding radius of gyration, R_g, is given by the relation [63]

$$R_g^2 = \frac{D_f(D_f + 1)}{2}\xi^2 \quad . \tag{3.6}$$

The radius of gyration is the root mean square distance of the objects' parts from either its center of mass.

A model function consisting of a single term of the form given by Eq. 3.5 or a sum of two terms of the form,

$$S(q) = S_1(q) + S_2(q) \quad , \tag{3.7}$$

was fit to each data set. For sets where the characteristic length scale ξ_1 at small-q was not discernible, generally for pH values above 4, $S_1(q)$ was replaced by $F_1(q) = F_o q^{-D_{f1}}$ and the sum of two terms of the form,

$$S(q) = F_1(q) + S_2(q) \quad , \tag{3.8}$$

was fit to each data set. The form of $F_1(q)$ is based on the assumption that ξ_1 is located at a value of q too small to be accessible by the SALS instrument, and that the observed scattering follows the power-law behaviour discussed above.

Fitting procedures were performed using the non-linear least-square fit algorithm provided by OriginLab software with minimizing χ^2. Example curve fits are presented in Figs. 3.21 and 3.22 where the curve is also separated into the two component terms and the lower graph is a plot of the residuals in terms of the uncertainty (σ) of each data point. Arrows on these figures identify characteristic length-scales from fits, and lines are a guide to the eye for the power-law slope. Figures 3.23 and 3.24 show examples of fitting results for the un-neutralized series, and for the 1.0 wt% concentration series, respectively. The results of the fit parameters, characteristic length scales (ξ_1 and ξ_2) and fractal dimensions (D_{f1} and D_{f2}), are tabulated in Appendix D and are presented in the following sections.
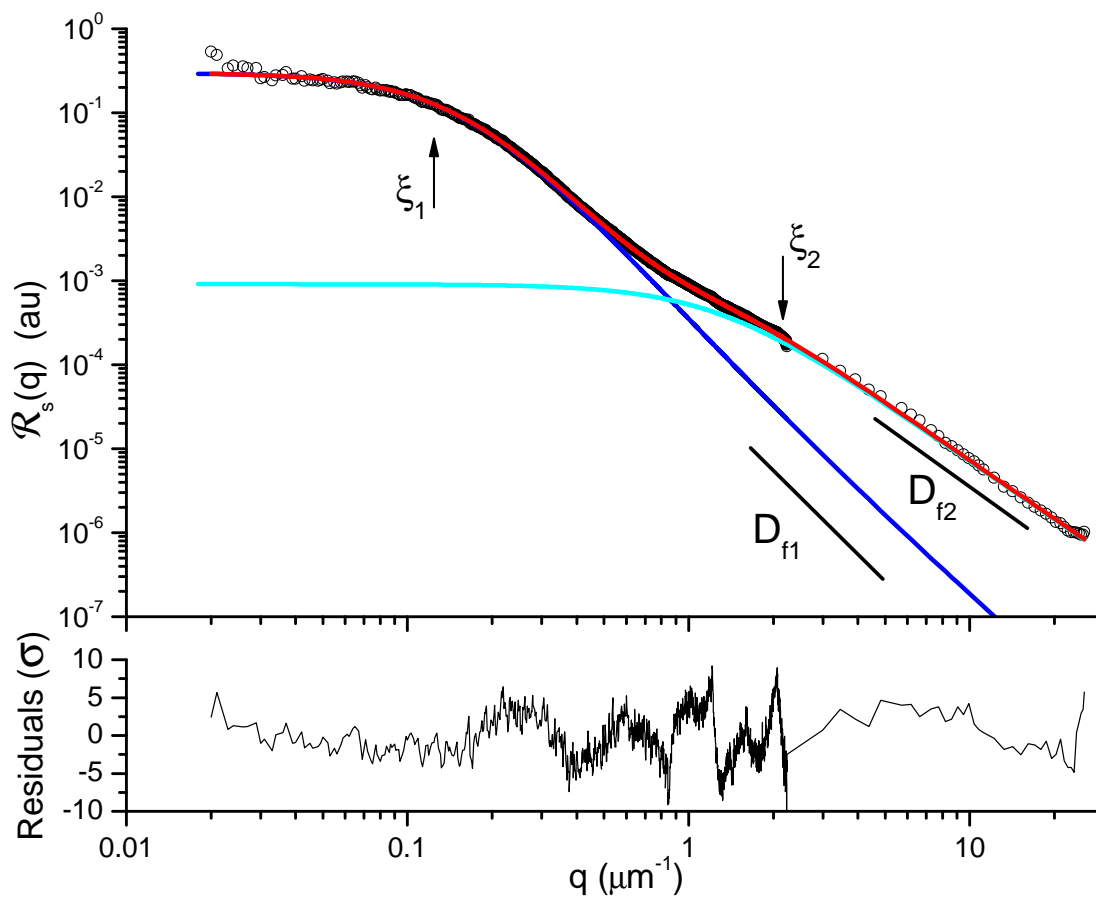
Figure 3.21: Sample fit of the 0.1 wt% Carbopol data at pH 3.81 using the two-term model of Eq. 3.7. The data is shown as open circles, and the three curves show each term, $S_1(q)$ and $S_2(q)$, individually and the sum, $S(q)$. The lower graph presents the residuals in terms of the uncertainty, σ, for each data point.
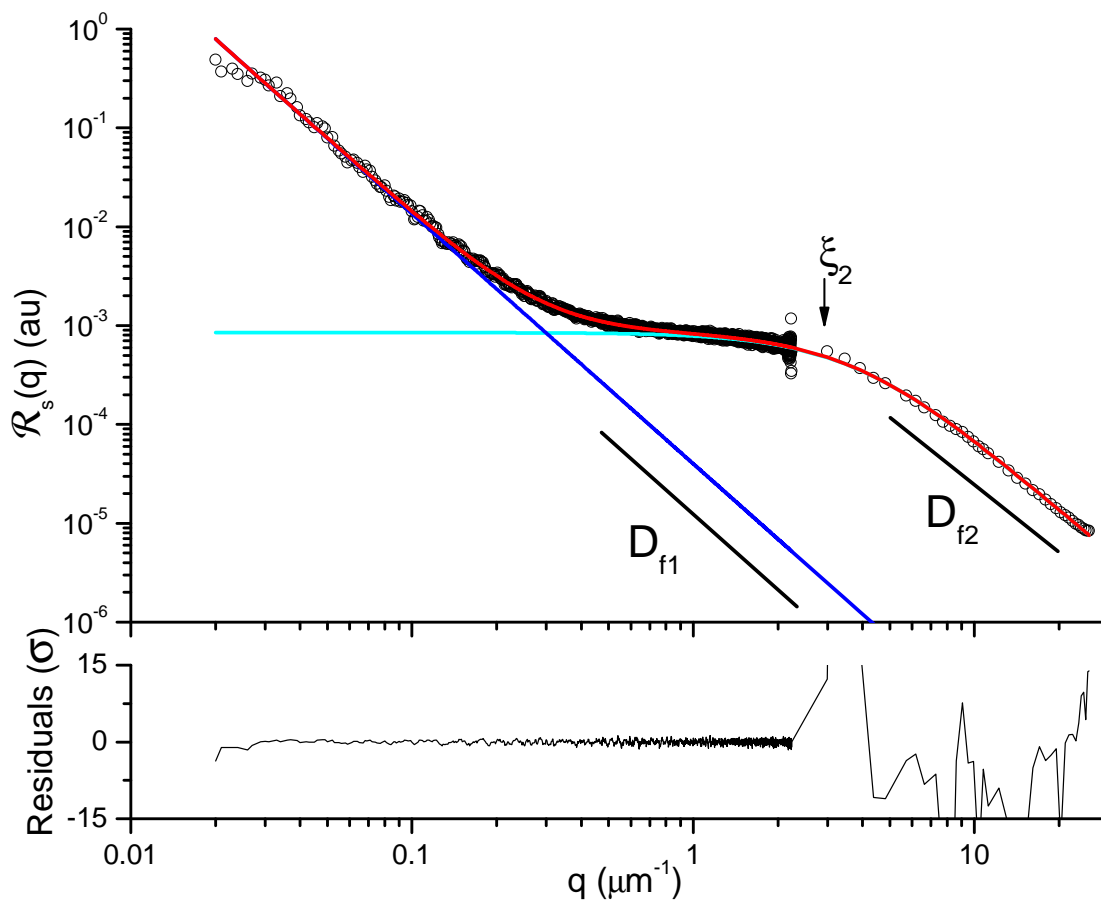
Figure 3.22: Sample fit of 1.0 wt% Carbopol data at pH 8.07 using the two-term model of Eq. 3.8. The data is shown as open circles, and the three curves show each term, $F_1(q)$ and $S_2(q)$, individually and the sum, $S(q)$. The lower graph presents the residuals in terms of the uncertainty, σ, for each data point.
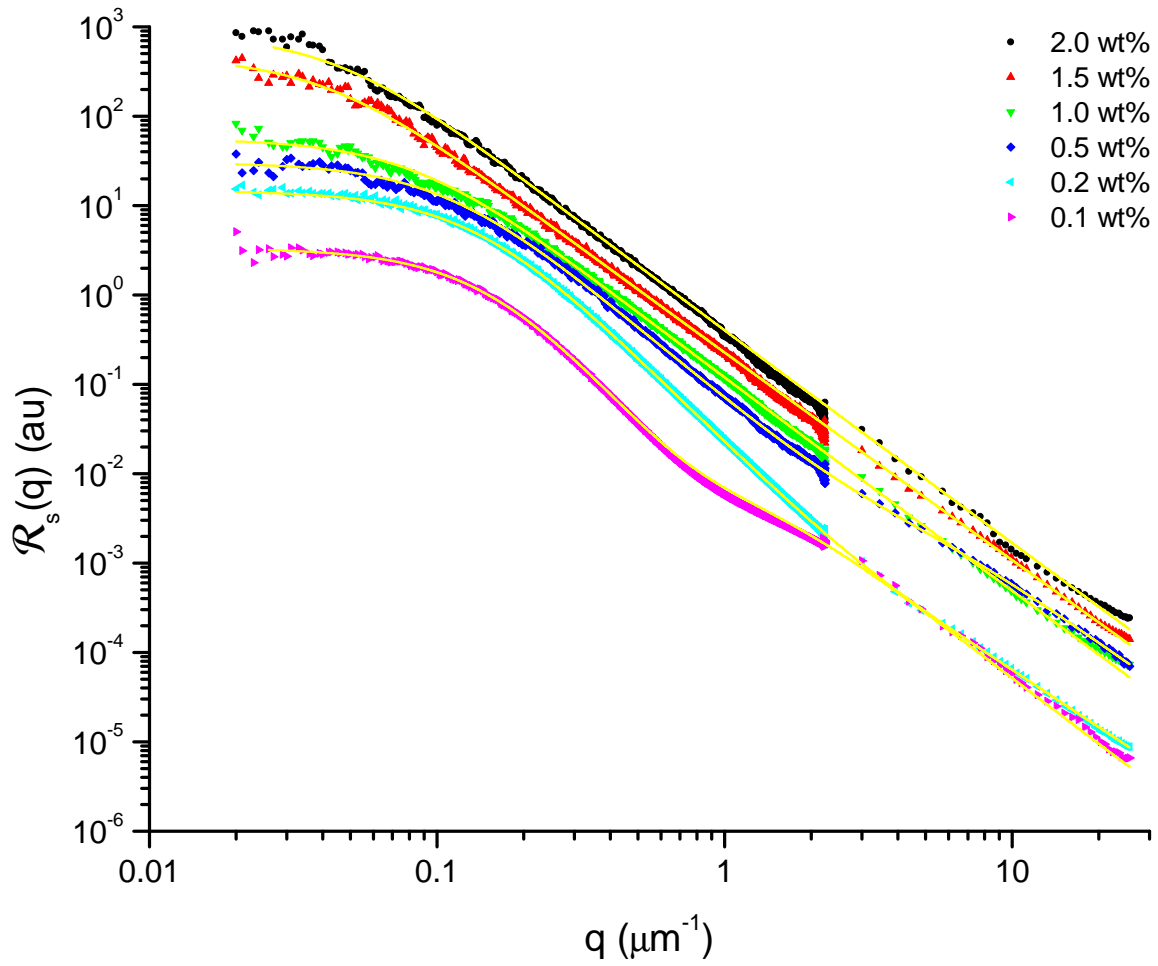
Figure 3.23: Fit of Eq. 3.7 to data for un-neutralized Carbopol samples.
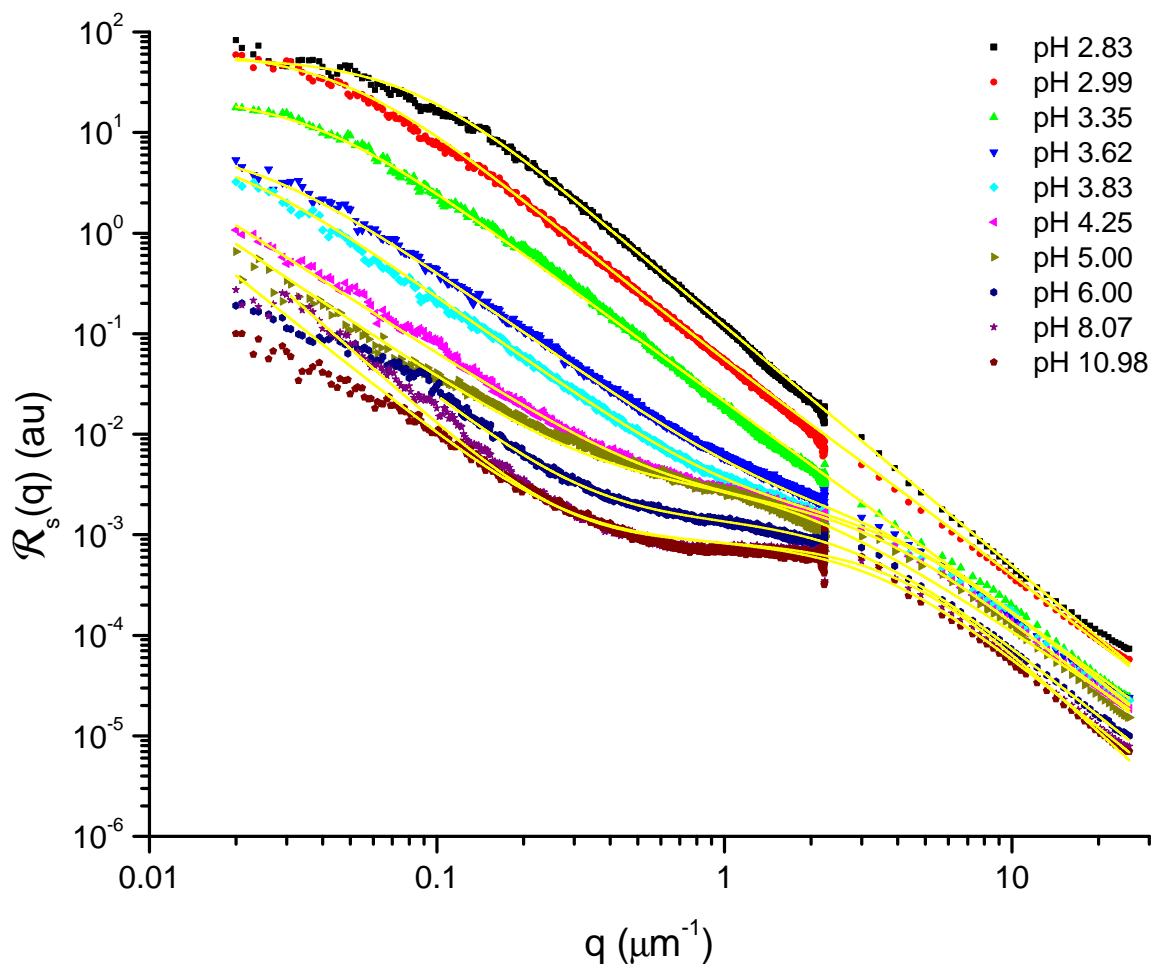
Figure 3.24: Fit of Eqs. 3.7 or 3.8 to data for the pH series from $1.0wt\%$ Carbopol samples with pH$\in [2.83, 10.98]$.

3.6 Summary of All Results from Fitting Procedure

The fitting process provides values for six parameters, but the scalar amplitudes, S_{o1} (or F_o) and S_{o2}, are not discussed in this thesis. The remaining four parameters, the characteristic length scales (ξ_1 and ξ_2) and fractal dimensions (D_{f1} and D_{f2}), will be discussed in detail in the following subsections. Figure 3.6 summarizes all of these parameters, without uncertainties, for every Carbopol sample as a function of pH. Later figures showing these same results include the uncertainty.
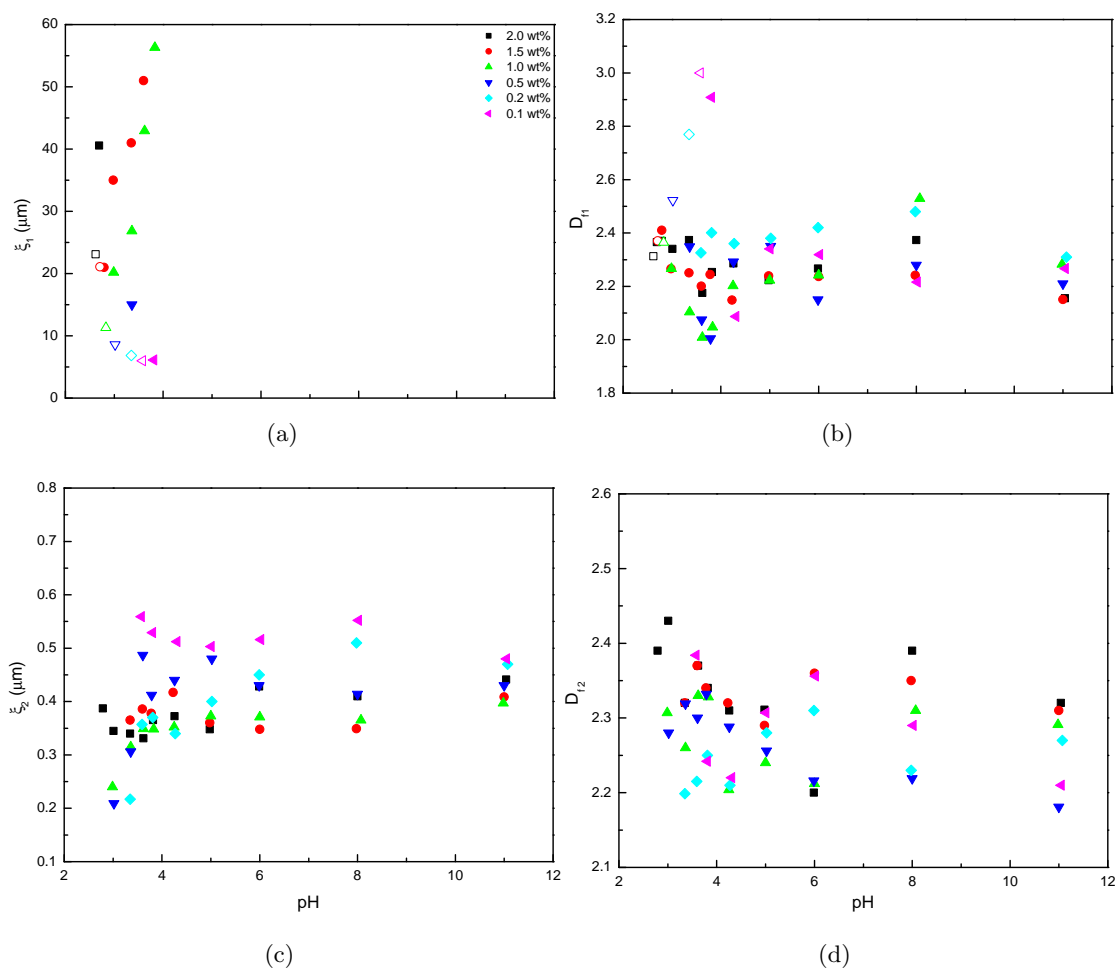
Figure 3.25: The pH dependence of the characteristic length scale ξ_1 and ξ_2 and the fractal dimensions D_{f1} and D_{f2} for the concentrations studied in this thesis. The open markers represent data from un-neutralized Carbopol samples. The legend for all of these graphs in shown in (a).

3.6.1 Larger Characteristic Length Scale ξ_1 and Fractal Dimension D_{f1}

Un-neutralized Carbopol Dispersions

The values for the larger characteristic length scale ξ_1 determined for the un-neutralized Carbopol samples is shown in Fig. 3.26(a) as a function of pH. This length scale decreases from 23.1(3) to 6.0(1)μm with increasing pH. The first fractal dimension, D_{f1}, is shown in Fig. 3.26(b). It increases from ≈ 2.3 to ≈ 3.0 with increasing pH.

(a)   (b)
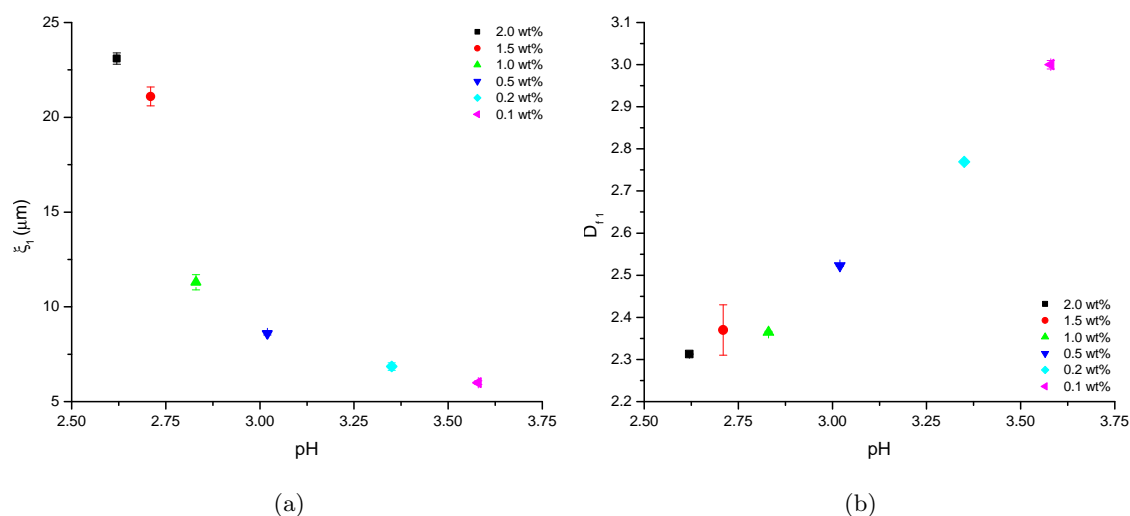
Figure 3.26: The pH dependence of (a) the characteristic length scale ξ_1 and (b) the fractal dimension D_{f1} for un-neutralized Carbopol samples.

As mentioned previously in Sec. 3.1, the greater the Carbopol concentration the higher the carboxylic acid concentration and, therefore, the lower the pH. Therefore, it is more conventional to display the values of ξ_1 and D_{f1} for un-neutralized samples as a function of concentration. Plots of ξ_1 and D_{f1} as a function of concentration are shown in Figs. 3.27(a) and (b), respectively. In this format, ξ_1 increases from 6.0(1) to 23.1(3)μm, and D_{f1} decreases from ≈ 3.0 to ≈ 2.3 over this concentration range. At 2 wt%, this result is similar to optical microscope results presented in Sec. 3.2.1, where it was found that the un-neutralized sample exhibited heterogeneous regions of $\approx 20\mu$m. As $c \to 0$, ξ_1 approaches a finite limiting size of $\approx 6\mu$m, which can be concluded from the finite fractal dimension of ≈ 3 representing a very dense system. At dilute concentrations, it appears that Carbopol gel particles are compact and space filling.
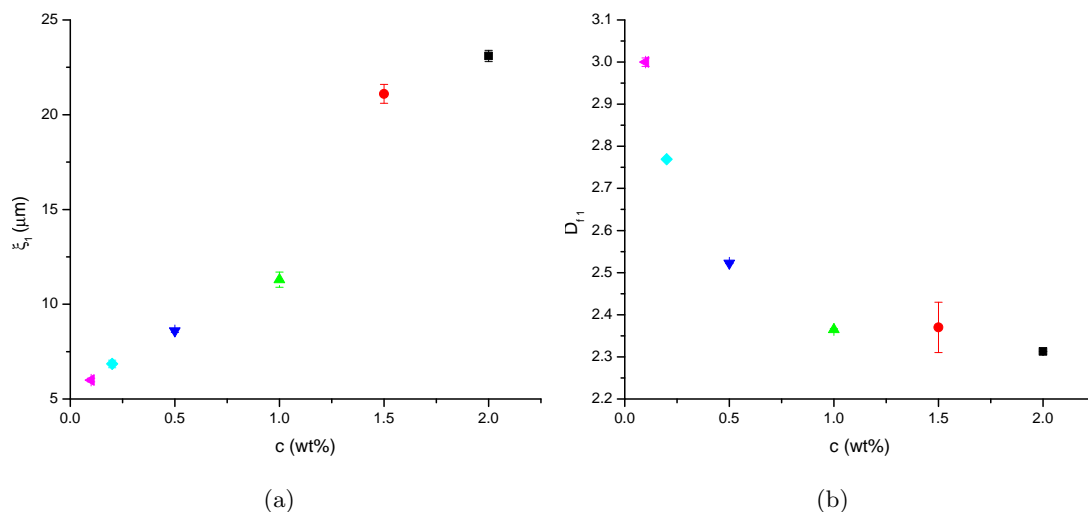
Figure 3.27: The concentration dependence of (a) the characteristic length scale ξ_1 and (b) the fractal dimension D_{f1} for un-neutralized Carbopol samples.

Neutralized Carbopol Dispersions

Figure 3.28(a) and (b) presents ξ_1 and D_{f1} values as a function of pH over the range of Carbopol concentrations studied in this thesis.   Also plotted are values from the un-neutralized Carbopol samples (cf. Fig. 3.26). For each concentration, ξ_1 increases as the pH increases. When the pH is greater than 4, ξ_1 could not be determined from the fit. Based on the observed trend, ξ_1 is believed to be located at a smaller q not accessible by the SALS instrument. Therefore for samples where $\xi_1 > 1/q_{min} \approx 50\mu$m, we only observe the fractal scattering behaviour $I(q) \approx q^{-D_{f1}}$. The values of D_{f1} for neutralized Carbopol samples are scattered between 2.0 and 2.5, with data primarily centered around ≈ 2.2. Comparing these values to Table 3.2, the range of fractal dimensions observed here suggests that the Carbopol mass-fractal structure could range from an ideal polymer ($D_f = 2$) to cluster aggregate ($D_f = 2.5$). The structure may also be interpreted as a mass-fractal with mass $M \propto r^{D_f}$. Note that the values of the fractal dimension should not be taken as an accurate measure since sample polydispersity generally leads to an under-estimation of the fractal dimension [64], and our samples are probably polydisperse. The qualitative changes in behaviour of ξ_1, and D_{f1} occurs at almost the same pH (pH$\approx$4) at which changes in the viscosity of Carbopol are observed. At pH values below 4, the viscosity is moderate, typically several orders of magnitude larger than that of water, while above a pH of 4 the
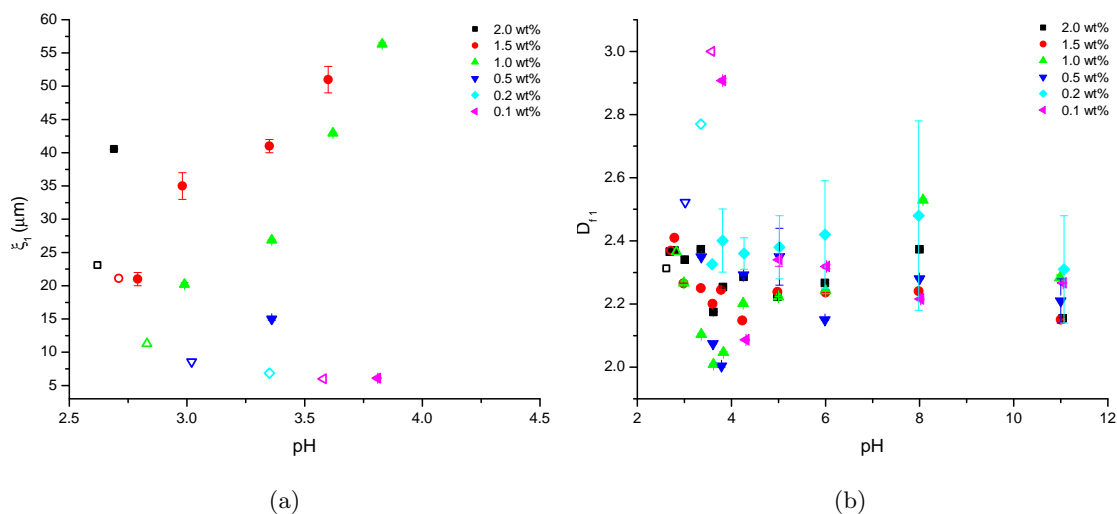
Figure 3.28: The pH dependence of the (a) the characteristic length ξ_1 and (b) the fractal dimension D_{f1} for different concentrations. The open symbols represent data for un-neutralized samples as presented previously in Fig. 3.26.

viscosity increases by approximately 5 orders of magnitude [3, 35].

3.6.2 Smaller Characteristic Length Scale ξ_2 and Fractal Dimension D_{f2}

The pH dependence of the smaller characteristic length scale, ξ_2, and the associated fractal dimension, D_{f2}, is presented in Figs. 3.29(a) and (b) respectively. ξ_2 appears to increase slightly with increasing pH up to $\approx$pH 4, and then appears to be roughly constant over the remaining pH and concentration range with a mean value of 0.42 μm a standard deviation of 0.02 μm. The fractal dimension ranges between 2.1 and 2.5 over the range of pH that was investigated. As with ξ_1, and D_{f1}, the qualitative changes in behaviour of ξ_2 occurs at almost the same pH (pH$\approx$4) that changes in the viscosity of Carbopol are observed.
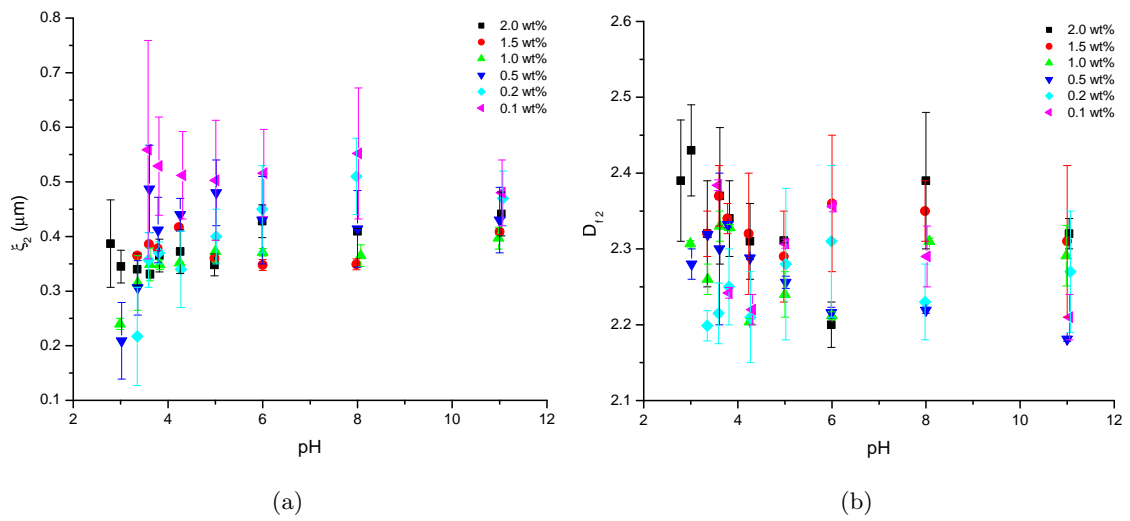
Figure 3.29: The pH dependence of the (a) the characteristic length ξ_2 and (b) the fractal dimension D_{f2} for the different concentrations.

3.7   Structure and Response

The following section examines possible contributions to the following trends in the characteristic length scale and fractal dimension of Carbopol, as extracted from the preceding analysis:

1. ξ_1 of un-neutralized Carbopol increases with increasing concentration

2. D_{f1} of un-neutralized Carbopol decreases with increasing concentration

3. ξ_1 increases with increasing neutralization over the full concentration range studied

4. D_{f1} is virtually constant with increasing neutralization over the full concentration range studied

5. ξ_2 is virtually constant with increasing neutralization over the full concentration range studied

6. D_{f2} is virtually constant with increasing neutralization over the full concentration range studied

The theoretical treatment of the swelling and de-swelling of gels is based on the minimization of the Gibbs free energy of the gel, first described in Flory's 1953 treatise on the thermodynamics of gels [65]. Contributions from quantitative experiments were later incorporated into this description [66, 67]. An ionic gel is subjected to an osmotic swelling pressure, π, which is equal to the polymer's volume derivative of the Gibbs free energy at fixed temperature and fixed concentration, $\pi = -\left(\frac{\partial \Delta G}{\partial V}\right)_{T,n}$.

Swelling of gels results mainly from the combined contributions of: the entropy of mixing polymer and continuous media, the configuration entropy of fixed ionic groups within the network, the degree of crosslinking, the degree of ionization of the charged groups, and the ionic concentration in the continuous medium [65, 68, 69, 33]. The swelling pressure is expressed as the sum of three components, mixing-, configuration-, and ionic-pressure,

$$\pi = \pi_{mix} + \pi_{config} + \pi_{ionic} \quad . \tag{3.9}$$

At equilibrium, π is zero.

The osmotic pressure associated with mixing entropy, π_{mix}, is given by the Flory-Huggins equilibrium model [65],

$$\pi_{mix} = -\frac{RT}{V_1} \left[\ln(1-v) + v + \chi v^2 \right] \quad , \tag{3.10}$$

where V_1 is the molar volume of the solvent, and v is the swollen polymer volume fraction (fully swollen $v = 1$). The Flory-Huggins polymer-solvent interaction parameter, χ, which represents the strength of interaction between the polymer and the solvent depends on the concentration-dependent solubility parameters of the polymer and solvent. Therefore, the swollen-volume fraction varies inversely with the Flory-Huggins parameter. The Flory-Huggins model is also the basis for the Flory-Rehner equilibrium model, which takes into account the average number of monomers between two crosslink sites, N_x, when describing the equilibrium polymer swelling volume [65],

$$- \left[ln(1-v) + v + \chi v^2 \right] = V_1 N_x \left[v^{1/3} - \frac{v}{2} \right] \quad . \tag{3.11}$$

A high degree of crosslinking results in a smaller swollen volume faction.

The osmotic pressure associated with configurational entropy, π_{config}, is determined by considering the free energy ΔG of the isotropic swelling process [66],

$$\Delta G = RT \left[n \left(\gamma_4 A_4 + \ln \frac{A_4}{\sinh A_4} - \gamma_5 A_5 + \ln \frac{A_5}{\sinh A_5} \right) + \frac{1}{2} \ln v \right] \tag{3.12}$$

where n is the number of monomers per polymer, $A_i = L^{-1}(\gamma_i)$ is the inverse Langevin function, and γ_i are parameters which depend on the volume fraction v and monomer count n. The inverse Langevin function may be expanded in a power series [68].

The osmotic pressure arising from ions and ionic interactions, π_{ionic}, is given by [65, 68],

$$\pi_{ionic} = RT \left[\Gamma \sum C_{in} - \gamma \sum C_{out} \right] \quad , \tag{3.13}$$

where C_{in} and C_{out} are the mobile ion concentrations inside and outside of the polymer. Γ and γ are osmotic coefficients that depend on the degree of ionization, α. Ionization of polymer groups, by conjugate-base neutralization, increases C_{in}, which increases the osmotic pressure. The addition of a polyelectrolyte to the system results in a decrease in the osmotic pressure. For polyelectrolyte-free systems, C_{out} is 0, and C_{in} is the concentration of ionized

sites, $C_{in} \propto \alpha C_o$, where C_o is the concentration of ionizable groups. At complete ionization, $\alpha = 1$, continued neutralization will increase C_{out} resulting in a decrease in the osmotic pressure [69].

The light scattering experiments performed on Carbopol exhibit some of these properties. The neutralization of Carbopol dispersions by NaOH exchanges the free hydrogen cation with sodium. This results in an increase in the number of mobile ions inside the polymer, and contributes to an increase in the osmotic pressure, as per Eq. 3.13. Crosslinking constrains the polymer from undergoing uncontrolled expansion. Lightly crosslinked polymers expand easily, while heavily crosslinked polymers do not expand as easily and are generally smaller in size, as per Eq. 3.11. This suggests that since $\xi_2 < \xi_1$ and ξ_2 is independent of pH, ξ_2 describes a region of polymers with a higher crosslink density than the region described by ξ_1. The difference in crosslink density may result from the synthesis process where rapid consumption of the crosslinker takes place early leading to a lower crosslink concentration in the outer regions of the polymer network. This interpretation of the length scales is consistent with the schematic diagram of Carbopol shown in Fig. 1.1. Figure 3.30 illustrates the swelling effect caused by neutralization.
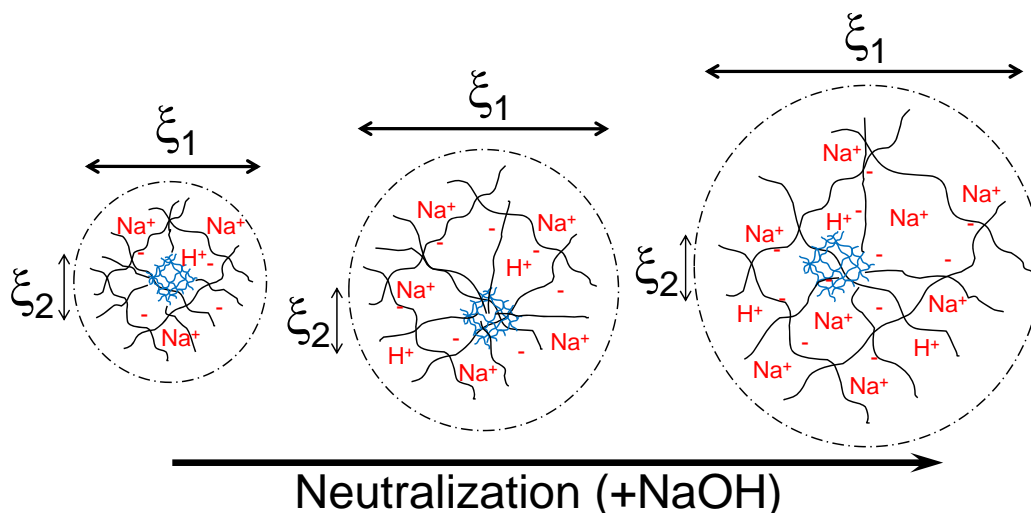
Figure 3.30: Schematic illustration of the structure of Carbopol size expansion through the neutralization process using sodium hydroxide (NaOH). ξ_2 is constant during neutralization while ξ_1 monotonically increases.

We have no explanation as to why the fractal dimensions for the two regions are similar and appear to be virtually constant with pH. It may be evidence that the Carbopol polymer
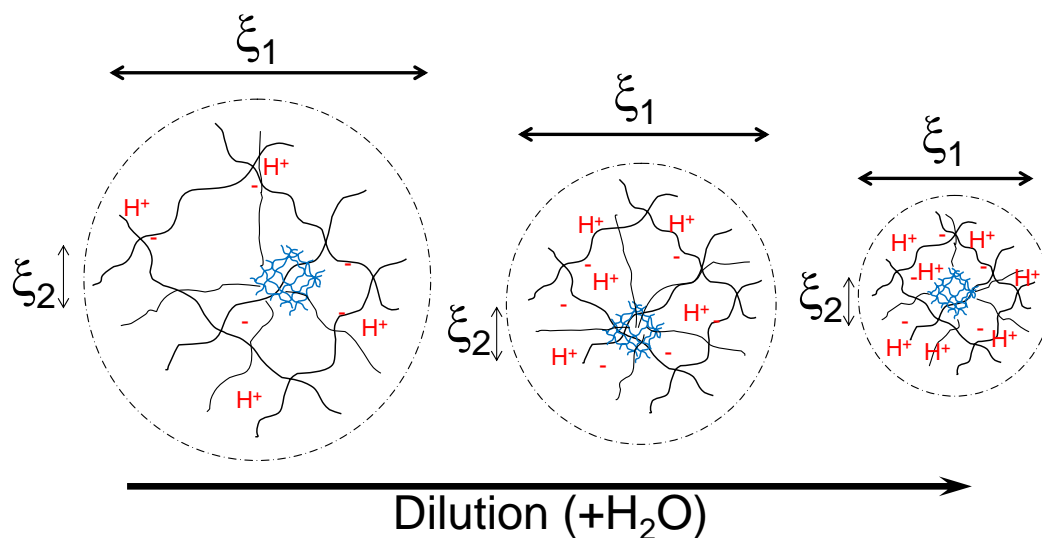
Figure 3.31: Schematic illustration of the structure of Carbopol size reduction through dilution. ξ_2 is constant during dilution while ξ_1 monotonically decreases.

system is a mass fractal, $M \propto r^{D_f}$.

The observed trends in ξ_1 and D_{f1} as the concentration of un-neutralized Carbopol dispersion is changed are currently a mystery. Figure 3.31 illustrates the de-swelling effect caused by dilution. Increasing the concentration of un-neutralized Carbopol dispersions appears to generate a positive osmotic pressure causing the polymer to swell. The high fractal dimension, 3, for the lowest concentration, $0.1wt\%$, may represent a collapsed polymer, or a polymer which has yet to swell from hydration.

Each member of the Carbopol family of polymers is synthesized using different amounts of crosslinker and different types of crosslinking polymers. Different Carbopol families are also synthesized with different types of polymers and copolymers [2]. Therefore, the characteristic length scales and fractal dimensions are expected to vary from formulations to formulation. The Carbopol dispersion formulation is also linked to other characteristic properties, such as intrinsic viscosity, ionic strength, overlap concentration and yield point [35].

Chapter 4

Summary and Outlook

Previous structural investigations of Carbopol using optical and electron microscopy have shown that the bulk structure consists of a closly packed isolated particles with length scales ranging from 2 μm to 20 μm. To investigate these large length scales, we designed and developed a small-angle light scattering instrument was designed and developed.

The small-angle light scattering instrument was designed around a detection system on a rotational base, the use of off-axis imaging to reduce aberrations and improve imaging conditions near the diffraction limit, and the ability to accomodate thick sample cells for weakly scattering samples. This arrangement extended the lower angular limit of our scattering instruments from 13° to 0.08°, and thus extends the largest measurable length scales, $d = 2\pi/q$, from 2μm to 315μm or $\xi = 1/q$, from 400nm to 50μm for scattering from aqueous media.

calibrated from diffraction from circular apertures and confirmed by polystyrene spheres.

Custom-built control software was designed for static light scattering analysis. This program gives the user the ability to define angular range, spacing, and resolution, as well as control over time-averaging and camera exposure times.

Carbopol is primarily synthesized using acrylic acid monomers, therefore modifying the pH was possible by conjugate base neutralization using sodium hydroxide. Carbopol dispersions were found to be quite turbid when un-neutralized and to have decreasing turbidity with increasing neutralization. Tabletop rheology measurements showed that a limited number of neutralized Carbopol dispersions flowed with tube inversion tests and provided a yield-stress of $\sim 4Pa$

The combination of the small-angle light scattering instrument and the ALV-5000/e

DLS/SLS light scattering instrument allowed us to explore the wavevector q over two decades in magnitude and has shed some light on the structure of Carbopol ETD2050. Light scattering data were analyzed using a mass-fractal model that provides information about characteristic length-scales and fractal dimensions. We determined that Carbopol ETD2050 polymers can be characterized by two length-scales with different behaviours. The two length scales have been attributed to regions with different cross-linking densities, a view that is consistent with an earlier model proposed by Barnes and Roberts [4]. The large length-scale depends on both concentration and neutralization, while the smaller length-scale is virtually independent of these parameters. The fractal dimensions for both length scales appear to be essentially constant over the neutralized pH range for all concentrations. However the fractal dimension for un-neutralized Carbopol dispersions decreases with increasing concentration.

Osmotic pressure has been used traditionally to explain the swelling behaviour of network polymers and gels. Contributions to the osmotic pressure include: the mixing of polymer and the solvent, the configuration of fixed ionic groups within the network, the degree of crosslinking, the degree of ionization of the charged groups, and the ionic concentration in the solvent. So far, we have been able to explain the pH dependence of the larger length scale using osmotic pressure, but we are currently unable to explain the concentration behaviour of un-neutralized dispersions. Based on the calculated swelling trends, we have attributed the fractal dimensions of these samples as evidence for a mass-fractal system, but have not been able to uniquely match the fractal dimension to a model structure.

4.1   Outlook for the small-angle light scattering instrument

Future developments of the small-angle light scattering instrument might include software redesign for performing static time-series light scattering and dynamic light scattering experiments, extending the angular range yet further, and temperature control.

Continued development of the small-angle static light scattering instrument software might include time-resolved measurements (using single or multiple exposures) to track time-dependent length scales. An example of a process that would benefit from this feature is spinodal decomposition, where a scattering peak, positioned at $q = \frac{2\pi}{l}$, translates or broadens as a function of time. Currently, the software assumes scattering is isotropic, but there may be a need for the development of a software component that determines the

equi-intensity path for polarization-dependent scattering.

On the heels of the successful implementation of the static light scattering analysis software, a dynamic light scattering analysis software package should be built. The dynamic light scattering software package should be able to simultaneously calculate the intensity-intensity correlation for multiple angles. It may be possible to build this package on top of the time-series image-capture program. The minimum accessible lag time should be about 500ms, which is set by the download transfer speed between the camera and the computer, and by related calculations. A combined static-dynamic light scattering program would be able to simultaneously report the Rayleigh scattering ratio and the intensity-intensity correlation function.

The option of extending the angular range of the small-angle light scattering instrument was briefly discussed in Chapter 2 but was not fully explored. This would require rotating the detector armature and redoing all the calibration tests discussed in Chapter 2. The upper observable angle is estimated to be $\approx 21°$.

With the commercial ALV-5000/e DLS/SLS light scattering instrument, we are able to perform temperature-dependent light scattering measurements. For the small-angle light scattering instrument, temperature control requires sample heating, which could be achieved using Peltier TEC devices mounted to a heating block surrounding the sample cell.

4.2   Outlook for Carbopol

This thesis focused on interpretation of the light scattering data of Carbopol in terms of a mass fractal. Its was found that the interpretation required to interpret the data using two mass fractal forms (*i.e.* surrounded by another mass fractal). An alternative model of interpreting the scattering data by considering as a mass fractal surrounded by a surface fractal [70]. The existence of two scattering length scales could also be interpreted as arising from dynamic and static regions of the polymer structure [71].

To aid in the understanding of the Carbopol structure and its influence on the yield-stress behaviours of these polymers, further light scattering investigations into other members of the Carbopol family of polymers are needed. Carbopol ETD2050 is part of a subgroup of Carbopol polymers which include the original Carbopol 941 and Ultrez 10. Carbopol 941 and Ultrez 10 are formulated by similar means, but 941 has a larger intrinsic viscosity, which is a possible signature of a higher crosslink density than ETD2050. ETD2050 differs from

Ultrez 10 by having a lower intrinsic viscosity and being hydrophobically modified during synthesis [35].

Companion measurements of bulk rheology of the Carbopol polymers would help in understanding how structure influences rheology. A parallel investigation of the bulk rheology of Carbopol ETD2050 showed that the yield stress is maximum in the region of pH4 and that this maximum is observed at the same pH across all concentrations [72]. These experiments also show that the yield stress increases with both pH and concentration, with slight decreases at the highest pH values for all concentrations. The study suggests that, when neutralized, the polymers uncoil and the particles enlarge. The swollen particles occupy a greater volume fraction, which increases the effects of jamming and makes the sample behave more like an elastic solid. However, as the polymer chains spread out, the individual Carbopol particles become less tightly bound and we observe a decrease in their elastic properties. The maximum spread of polymer chains occurs when the degree of neutralization is 1 ($\alpha = 1$), and further neutralization causes deswelling.

Appendix A

Mie Scattering Solution

This appendix presents the equation for the Mie solution for scattering of electromagnetic radiation by a sphere. The equations presented are taken from a combination of Bohren and Huffman [38] and van de Hulst [40].

As presented in Sec. 2.1, the elements of the scattering matrix are

$$
\begin{aligned}
S_{12}(\theta) &= S_{21}(\theta) = 0 \quad, \\
S_{11}(\theta) &= \sum_{j=1}^{\infty} \frac{2j+1}{j^2+j} \left(a_j \pi_j(\cos\theta) + b_j \tau_j(\cos\theta) \right) \quad,
\end{aligned}
\tag{A.1}
$$

$$
S_{22}(\theta) = \sum_{j=1}^{\infty} \frac{2j+1}{j^2+j} \left(a_j \tau_j(\cos\theta) + b_j \pi_j(\cos\theta) \right) \quad,
\tag{A.2}
$$

each of which consists of an infinite series of terms. The number of terms required in the series is based on the convergence of the Riccati-Bessel functions, and can be described by the size parameter kR. According to [47] the number of terms required is

$$
N = \begin{cases}
kR + 4(kR)^{1/3} + 1 & : \quad 0.02 \le kR \le 8 \\
kR + 4.05(kR)^{1/3} + 2 & : \quad 8 < kR < 4200 \\
kR + 4(kR)^{1/3} + 2 & : \quad 4200 \le kR \le 20000
\end{cases}
\tag{A.3}
$$

The functions of the series are defined in terms of Legendre polynomials

$$\pi_j(\cos\theta) = \frac{dP_j(\cos\theta)}{d\cos\theta} \tag{A.4}$$

$$\tau_j(\cos\theta) = \cos\theta\pi_j(\cos\theta) - \sin^2\theta\frac{d\pi_j(\cos\theta)}{d\cos\theta} \quad . \tag{A.5}$$

These functions can also be written in terms of the associated Legendre functions. The pre-factors of the terms in the series are defined by

$$a_j = \frac{\psi_j(\alpha)\psi_j'(\beta) - m\psi_j'(\alpha)\psi_j(\beta)}{\zeta_j(\alpha)\psi_j'(\beta) - m\zeta_j'(\alpha)\psi_j(\beta)} \quad , \tag{A.6}$$

$$b_j = \frac{m\psi_j(\alpha)\psi_j'(\beta) - \psi_j'(\alpha)\psi_j(\beta)}{m\zeta_j(\alpha)\psi_j'(\beta) - \zeta_j'(\alpha)\psi_j(\beta)} \quad , \tag{A.7}$$

where m is the refractive index of the sphere relative to the medium, and ψ and ζ are defined using Bessel and Hankel functions:

$$\psi_j(\delta) = \sqrt{\frac{\pi\delta}{2}}J_{j+\frac{1}{2}}(\delta) \quad , \tag{A.8}$$

$$\zeta_j(\delta) = \sqrt{\frac{\pi\delta}{2}}H_{j+\frac{1}{2}}^{(2)}(\delta) \quad , \tag{A.9}$$

and the arguments of these functions are

$$\alpha = \frac{2\pi n_s R}{\lambda_o} \qquad \beta = \frac{2\pi n_p R}{\lambda_o} \quad , \tag{A.10}$$

where n_s is the refractive index of the surrounding medium, n_p is the refractive index of the spherical particle, R is the radius of the sphere, and λ_o is the wavelength in vacuum of the electromagnetic wave.

Appendix B

List of Apparatus Components

This is a list of the primary components used in the construction of the small angle light scattering instrument.

Table B.1: SALS Apparatus component manifest

Part	Supplier	Details
Optical breadboard	Thorlabs	PBH51517
Camera	QImaging	Retiga 2000R Fast
		1200x1600 (Monochrome)
		12bit, Firewire 1394a
- Mounts	Linos	1094.2408.009.020
		1094.2408.009.123
		1094.2408.009.112
- Lens	Linos	273 0075 002
Laser	Thorlabs	HRP120
- Power supply		HPS2

Table B.1: *continued*

Spatial filter / Beam expander		
- Positioners	Thorlabs	ST1XY-D/M
		KC1-T/M
		SM1Z
- Aperature		PS10 (10μm)
- Achromatic Doublet		C240TM-A (f8 ϕ12.2)
- Plano-convex	NewPort	KPX040AR.14 (f19 ϕ12.7)
Detection optics		
- Achromatic Doublet	Newport Optics	PAC086AR.14 (f150 ϕ50.8)
- Positive Miniscus	Thorlabs	LE1015-A (f200 ϕ50.8)
Rotary Base	Velmex	B4872TS
		72:1, 1.9A/Phase
- Controller	Standa	8SMC1-USBh-B2-2PS
		2axis (12V, $2A_{Max}$)
Photodiodes	DigiKey	OPT101
Line Filters	Thorlabs	FL632.8-10 (FWHM=10nm)
Attenuator	Haydon Switch and Instruments	26443-12-068
Polished reflector	MiniTools Inc.	MTC13005
- Positioner	National Aperture Inc.	MM-3XYZ
Data acquisition board	Data Translations	DT9802
Computer	Dell Dimension	GX280
- Processor		Pentium 4, 3.2GHz
- Memory		2GB
LabView	National Instruments	Version 8

Appendix C

Software

This appendix summarizes three major aspects of the software described in Sec. 2.4 in greater detail.

C.1   Pixel-to-Ring Map

Input:

- Radius of the largest ring in the image (Max_R)

- Radius of the smallest ring in the image (Min_R)

- Ring width (W_R)

- Ring spacing (S_R)

- Calculated radius limits ($[r_{Min}, r_{Max}]_k$) [inputted from another code]

- Centre (x_o,y_o)

Output:

- Pixel-Ring Map matrix

For any given pixel, this algorithm determines whether or not the pixel belongs to an integration ring. If so, the corresponding element on the Pixel-Ring Map will be given the

index value of the integration ring, otherwise the element will receive a null value of -1. A value of -1 for elements of the map signifies pixels of no interest and is ignored in latter parts of the main software program.

Starting with pixel (i, j), the distance from the centre is calculated from

$$R(i, j) = \sqrt{(i - x_o)^2 + (j - y_o)^2} \quad , \tag{C.1}$$

and is fed the algorithm shown in figure C.1.
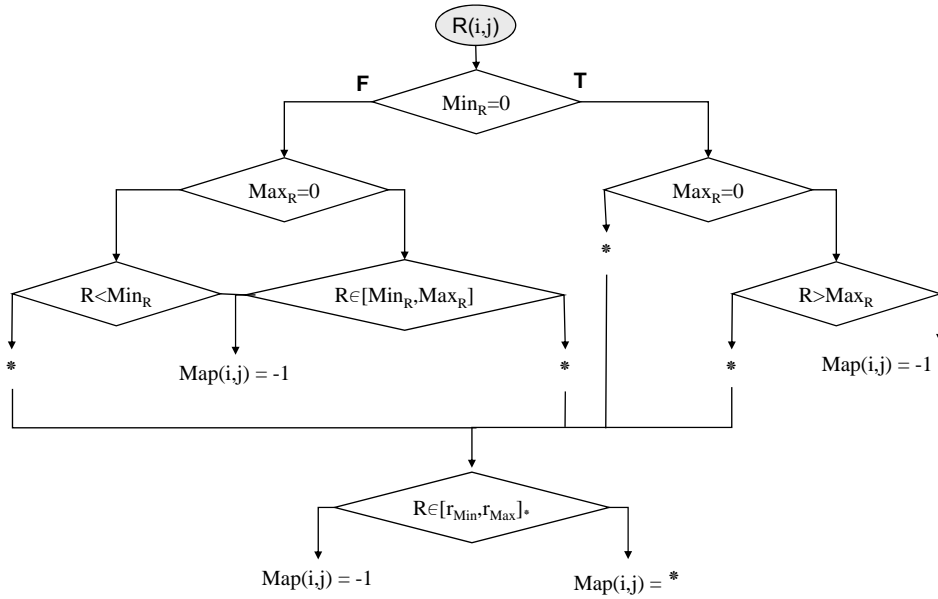
Figure C.1: Flow chart of the Pixel to Ring algorithm.

In the flowchart, the algorithm encounters a $*$ or a -1 during its process. The $*$ is a condition where an additional calculation is the performed to determine the index of the ring given by

$$* = \left\lfloor \frac{R(i, j) - Min_R}{W_R + S_R} \right\rfloor \quad . \tag{C.2}$$

A final comparison is made against the radius limits for integration, and a value is assigned to the pixel-ring map accordingly.

C.2 Ring-to-Scattering Vector q

Input:

- Calculated Radius Limits ($[r_{Min}, r_{Max}]_k$)

- Wavelength of light in vacuum (λ_o)

- Refractive index of the scattering medium (n_s)

- Pixel size (Δr)

- System magnification (M)

- Focal length of collection optics (f)

Output:

- q-array indexed by ring

- q-uncertainty array indexed by ring

From Eq. 2.17, the radius is related to an angle in air (θ_a), but the scattering angle (θ_s) from the sample is found using Snell's law in terms of the radius and the focal length

$$\sin\theta_a = \frac{r}{\sqrt{r^2 + M^2 f^2}} \quad \sin\theta_s = \frac{r}{n_s\sqrt{r^2 + M^2 f^2}} \quad . \tag{C.3}$$

Using the $\sin(\theta/2)$ half-angle identity, an equation for the magnitude of the scattering vector is obtained

$$q(r) = \frac{2\pi n_s}{\lambda_o}\sqrt{2 - 2\sqrt{1 - \frac{r^2}{n_s^2(r^2 + M^2 f^2)}}} \quad . \tag{C.4}$$

The uncertainty in q is defined by the fact that the pixel has a width of Δr; therefore the uncertainty is written as

$$\Delta q^2(r) = \Delta r^2 \left(\frac{dq(r)}{dr}\right)^2 \tag{C.5}$$

$$= \frac{\Delta r^2 2\pi^2 n_s^2 M^4 f^4 \left(\sqrt{\frac{n_s^2 r^2 + n_s^2 M^2 f^2 - r^2}{n_s^2(r^2 + M^2 f^2)}} + 1\right)}{\lambda_o^2 \left(n_s^2 r^2 + n_s^2 M^2 f^2 - r^2\right)\left(r^2 + M^2 f^2\right)^3} \quad . \tag{C.6}$$

C.3   Multiple-Exposure-Times

Input:

- Sample scatter images (I_k)

- Stray scatter images (S_k)

- Maximum linearity threshold value (Max)

- Minimum linearity threshold value (Min)

Output:

- Time matrix for scattered images ($T_{scatter}$)

- Time matrix for stray images (T_{stray})

Handling multiple exposure times extends the dynamic range of the instrument but also serves as a way to select the best-case exposure time when accounting for the stray light in sample intensities as given by Eq. 2.22 and 2.24. This algorithm assumes that a linear response region has been identified $[Min, Max]$.

The intensity of the scattered light collected from samples is greater than the intensity of the scattered light from stray sources, but this may not always be true. The algorithm presented here is applied to a single pixel by comparing each of the exposure times such that both the scattered light and stray light are within the linear bounds. The exposure times are not known to the program; therefore, the output matrices contain exposure time indices.

The algorithm first identifies the largest exposure time index such that the intensity, I of the pixel is less than Max. The selected exposure time index is subsequently used to determine if the stray light intensity is smaller that the scattered light. The exposure time index of the stray light images is selected to be within the linear region. At completion of the algorithm, two matrices are output; the exposure time index for the scattered light, and the exposure time index for the stray light.
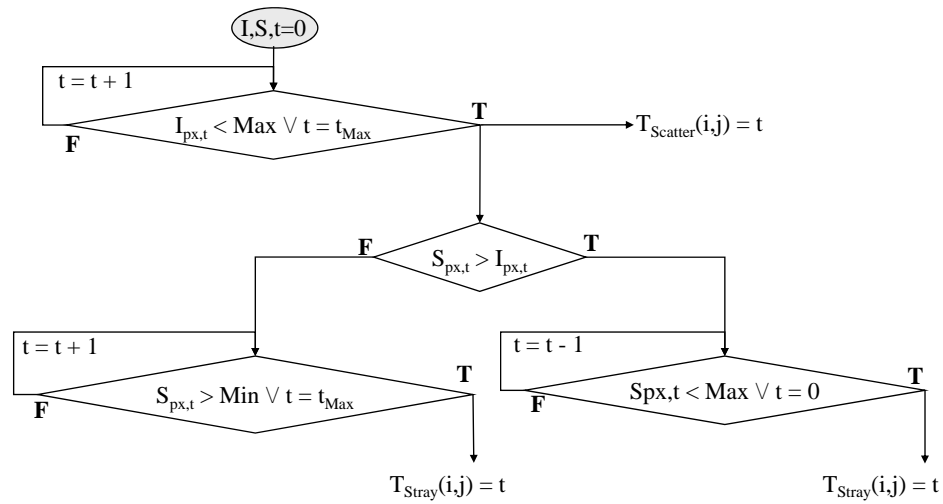
Figure C.2: Flow chart for the multiple exposure time algorithm.

In the main program, the user has the option of selecting the method to handle multiple exposure times; Ring, Coupled-Pixel , Independent-Pixel. Although the algorithm for the Independent-Pixel case is presented in full detail, the other programs are simplifications of the algorithm described above.

Appendix D

Tabulation of Fitting Parameters

Presented here are the characteristic length scales (ξ_1, ξ_2) and fractal dimensions (D_{f1}, D_{f2}) extracted from the analysis of each sample that was studied. Data from samples marked with an asterisk $*$ in the ξ_1 column were fit using Eq. 3.8. Data from samples marked with a — in the ξ_2 and D_{f2} columns were fit using only Eq. 3.5. Data from all other samples were fit using Eq. 3.7.

pH	ξ_1 (μm)	D_{f1}	ξ_2 (μm)	D_{f2}
3.58	6.0(1)	3.00(1)	0.5(2)	2.384(7)
3.81	6.11(5)	2.908(6)	0.53(9)	2.242(7)
4.31	$*$	2.087(2)	0.51(8)	2.22(2)
5.01	$*$	2.34(2)	0.5(1)	2.307(6)
6.02	$*$	2.319(7)	0.52(8)	2.356(7)
8.02	$*$	2.216(3)	0.5(1)	2.29(4)
11.85	$*$	2.267(2)	0.48(6)	2.21(3)

Table D.1: Fitting results for 0.1wt% Carbopol

pH	ξ_1 (μm)	D_{f1}	ξ_2 (μm)	D_{f2}
3.35	6.9(2)	2.769(1)	0.22(9)	2.20(2)
3.59	*	2.326(1)	0.36(5)	2.22(4)
3.81	*	2.4(1)	0.37(2)	2.25(5)
4.27	*	2.36(5)	0.34(2)	2.21(6)
5.02	*	2.4(1)	0.40(5)	2.3(1)
5.99	*	2.4(2)	0.45(8)	2.3(1)
7.98	*	2.5(3)	0.51(7)	2.23(5)
11.07	*	2.3(2)	0.47(5)	2.27(8)

Table D.2: Fitting results for 0.2wt% Carbopol

pH	ξ_1 (μm)	D_{f1}	ξ_2 (μm)	D_{f2}
3.02	8.59(7)	2.522(1)	0.21(7)	2.28(2)
3.36	15.0(2)	2.349(1)	0.31(5)	2.319(4)
3.61	*	2.075(1)	0.49(8)	2.3(1)
3.79	*	2.004(4)	0.41(6)	2.332(4)
4.26	*	2.292(3)	0.44(3)	2.288(2)
5.02	*	2.35(9)	0.48(6)	2.256(8)
5.99	*	2.150(3)	0.43(8)	2.216(7)
8.00	*	2.280(1)	0.41(7)	2.229(4)
11.00	*	2.21(7)	0.43(6)	2.181(3)

Table D.3: Fitting results for 0.5wt% Carbopol

pH	ξ_1 (μm)	D_{f1}	ξ_2 (μm)	D_{f2}
2.83	11.3(4)	2.365(2)	—	—
2.99	20.2(3)	2.267(6)	0.24(1)	2.307(4)
3.35	26.84(9)	2.104(3)	0.32(5)	2.26(2)
3.62	42.93(9)	2.009(2)	0.35(3)	2.33(2)
3.83	56.3(3)	2.047(3)	0.348(9)	2.328(4)
4.25	*	2.202(1)	0.352(1)	2.204(4)
5.00	*	2.223(1)	0.37(2)	2.24(3)
6.00	*	2.242(1)	0.371(7)	2.212(5)
8.07	*	2.529(4)	0.37(2)	2.31(4)
10.98	*	2.283(9)	0.40(2)	2.29(4)

Table D.4: Fitting results for 1.0wt% Carbopol

pH	ξ_1 (μm)	D_{f1}	ξ_2 (μm)	D_{f2}
2.71	21.1(5)	2.37(6)	—	—
2.79	21(1)	2.410(2)	—	—
2.98	35(2)	2.266(1)	—	—
3.35	41(1)	2.2505(1)	0.365(5)	2.32(3)
3.60	51(2)	2.2006(4)	0.386(4)	2.37(7)
3.78	$*$	2.2447(5)	0.378(4)	2.34(7)
4.23	$*$	2.1483(7)	0.417(5)	2.32(2)
4.98	$*$	2.2388(7)	0.360(4)	2.29(6)
6.00	$*$	2.2368(7)	0.35(1)	2.36(9)
7.98	$*$	2.241(2)	0.35(1)	2.35(4)
11.00	$*$	2.1507(7)	0.409(5)	2.3(1)

Table D.5: Fitting results for 1.5wt% Carbopol

pH	ξ_1 (μm)	D_{f1}	ξ_2 (μm)	D_{f2}
2.62	23.1(3)	2.3128(2)	—	—
2.69	40.55(3)	2.3659(2)	—	—
2.79	$*$	2.37(1)	0.387(8)	2.39(8)
3.01	$*$	2.34(1)	0.345(3)	2.43(6)
3.35	$*$	2.373(1)	0.34(3)	2.32(7)
3.62	$*$	2.326(1)	0.331(7)	2.37(9)
3.82	$*$	2.254(3)	0.37(3)	2.34(5)
4.26	$*$	2.286(2)	0.37(4)	2.31(5)
4.98	$*$	2.223(2)	0.45(2)	2.311(3)
5.99	$*$	2.267(1)	0.43(3)	2.20(3)
8.00	$*$	2.3732(7)	0.410(5)	2.39(9)
11.04	$*$	2.155(3)	0.44(4)	2.32(2)

Table D.6: Fitting results for 2.0wt% Carbopol

Bibliography

[1] T. A. Witten, "Insights from soft condensed matter," Reviews of Modern Physics **71,** S367–S373 (1999).

[2] "Noveon Polymers Technical Bulletins," Technical report, Noveon Pharmaceuticals (2002) .

[3] J. O. Carnali and M. S. Naser, "The use of dilute solution viscometry to characterize the network properties of carbopol microgels," Colloid and Polymer Science **270,** 183–193 (1992).

[4] G. P. Roberts and H. A. Barnes, "New Measurements of the flow-curves for Carbopol dispersions without slip artifacts," Rheologica Acta **40,** 499–503 (2001).

[5] S. J. Curran, R. E. Hayes, A. Afacan, M. C. Williams, and P. A. Tanguy, "Properties of Carbopol Solutions as Models for Yield-Stress Fluids," Journal Food Science **67,** 176–180 (2002).

[6] M. T. Islam, N. Rodriguez-Hornedo, S. Ciotti, and C. Ackermann, "Rheological characterization of topical carbomer gels neutralized to different pH," Pharmaceutical Research **24,** 1192–1199 (2004).

[7] H. A. Barnes, *A Handbook of Elementary Rheology* (Cambridge, Aberystwyth, Wales, 2000), Chapter 11: Very shear-thinning or yield-stress fluids.

[8] J. M. Piau, "Carbopol gels: Elastoviscoplastic and slippery glasses made of individually swollen sponges: Meso- and macroscopic properties, constitutive equations and scaling laws," Journal of Non-Newtonian Fluid Mechanics **144,** 1–29 (2007).

[9] F. K. Oppong, L. Rubatat, B. J. Frisken, A. E. Bailey, and J. R. de Bruyn, "Microrheology and structure of a yield-stress polymer gel," Physical Review E **73,** 041405 (2006).

[10] F. K. Oppong and J. R. de Bruyn, "The local structure and liquid-solid transition of a microgel suspension," In preparation (2009).

[11] J.-Y. Kim, J.-Y. Song, E.-J. Lee, and S.-K. Park, "Rheological properties and microstructure of Carbopol gel network system," Colloid and Polymer Science **281,** 614–623 (2003).

[12] J. E. Elliot, M. Macdonald, J. Nie, and C. N. Bowman, "Structure and swelling of poly(acylic acid) hydrogels: effect of pH, ionic strength, and dilution on the crosslinked polymer structure," Polymer **45,** 1503–1510 (2004).

[13] F. Schosseler, F. Ilmain, and S. J. Candau, "Structure and properties of partially neutralized poly(acrylic acid) gels," Macromolecules **24,** 225–234 (1991).

[14] in *Physical properties of polymeric gels*, J. P. Cohen-Addad, ed., (Wiley, New York, 1974), Chapter : Structure of Gels Investigated by means of Static Scatterings Techniques.

[15] G. D. Patterson, "Light scattering from bulk polymers," Annual Reviews of Material Science **13,** 219–245 (1983).

[16] A. K. Sood, "Light scattering from colloids," Hyperfine Interactions **37,** 365–384 (1987).

[17] B. Prötzl and J. Springer, "Light scattering experiments on shear induced structures on micellar solutions," Journal of Colloids and Interface Science **190,** 327–333 (1997).

[18] N. L. Kramarenko, I. V. Kurnosov, and Y. V. Naboikin, "Structure investigation of liquid crystals by light scattering," Physica Status Solidi **25,** 329–338 (1974).

[19] D. W. Weinert, T. G. Cleary, G. W. Mulholland, and P. F. Beever, "Light scattering characteristics and size distribution of smoke and nuisance aerosols," Fire Science Safety - Proceeding of the 7th International Symposium **7,** 209–220 (2003).

[20] J. Pencer and F. R. Hallet, "Effect of vesicle size and shape on static and dynamic light scattering measurements," Langmuir **19,** 7488–7497 (2003).

[21] S. V. Tsinopoulos, E. J. Sellountos, and D. Polyzos, "Light scattering by aggregate red blood cells," Applied Optics **41,** 1408–1417 (2002).

[22] H. K. Bustard and R. W. Smith, "Investigation into the scattering of light by human hair," Applied Optics **30,** 3485–3491 (1991).

[23] F. Scheffold and P. Schurtenberger, "Light scattering probes of viscoelastic fluids and solids," Soft Materials **1,** 139–165 (2003).

[24] J. W. Strutt, "A general law relating the intensity of light scattered from small particles to the wavelength of the light when the dimensions of the particles is much less than the wavelength," Philosophica Magazine **41,** 107,274,447 (1871).

[25] J. V. Iribarne and H.-R. Cho, *Atmospheric Physics* (Kluwer Academic Publishers, Boston, 1980).

[26] B. Berne and R. Pecora, in *Dynamic Light Scattering* (Dover, 2003).

[27] F. Scheffold and R. Cerbino, "New trends in light scattering," Current Opinions in Colloids and Interface Science **12,** 50–57 (2007).

[28] P. P. Debye, "A photoelectric instrument for light scattering measurements and a differential refractometer," Journal of Applied Physics **17,** 392–398 (1946).

[29] B. Chu, *Laser Light Scattering: Basic Principles and Practice* (Academic Press, Boston, 1991), Chapter 3: Photon correlation spectroscopy.

[30] J. B. Jastovka, "An optical apparatus for very-small-angle ligth scattering – Design, analysis and performance," The Bell System Technical Journal **55,** 1225–1293 (1976).

[31] F. Ferri, "Use of a charged coupled device camera for low-angle elastic light scattering," Review of Scientific Instruments **68,** 2265–2274 (1997).

[32] L. Cippelletti and D. A. Weitz, "Ultralow-angle dynamic light scattering with a charge coupled device camera based multispeckle, multitau correlator," Review of Scientific Instruments **70,** 3214–3221 (1999).

[33] M. Cloitre, R. Borrega, F. Monti, and L. Leibler, "Structure et écoulement de microgels polyélectrolytes: de la suspension au verre," Compter Rendus Physique **4,** 221–230 (2003).

[34] A. Gómez-Carracedo, C. Alvarez-Lorenzo, J. L. Gómez-Amoza, and A. Concheiro, "Glass transitions and viscoelastic properties of Carbopol and Noveon compacts," International Journal of Pharmaceutics **274,** 233–243 (2004).

[35] D. D. Desai, D. F. Hasman, and J. F. Schmucker-Castner, "Advances in Carbomer Polymer Technology," Technical report, BF Goodrich (2006) .

[36] C. Alvarez-Lorenzo and A. Concheiro, "Effects of surfactants on gel behavior: Design implications for drug delivery systems, Healthcare Technology Review," American Journal of Drug Delivery **1,** 77–101 (2003).

[37] R. Klein and B. D'Aguanno, in *Light Scattering: Principle and Development*, W. Brown, ed., (Claredon Press, Oxford, 1996), Chapter 2: Static scattering of colloidal suspensions.

[38] C. F. Bohren and D. R. Huffman, *Absorption and scattering of light by small particles* (Wiley-Interscience, New York, 1983), Chapter 1: Introduction.

[39] M. Kerker, *The Scattering of Light and Other Electromagnetic Radiation* (Academic Press, New York, 1969), Chapter 3: Scattering by a sphere.

[40] H. C. van de Hulst, *Light Scattering by Small Particles* (Dover, New York, 1981), Chapter 9: Rigorous scattering theory for spheres of arbitrary size (Mie theory).

[41] M. Kerker and E. Matijevic, "Scattering of electromagnetic waves from concentric infinite cylinders," Journal of the Optical Society of America **51,** 506–510 (1961).

[42] G. Mie, "Articles on the optical characteristics of turbid tubes, especially colloidal metal solutions.," Annalen der Physik **25,** 377–445 (1908).

[43] S. Asano and M. Sato, "Light scattering by randomly oriented spheroidal particles," Applied Optics **19,** 962–974 (1980).

[44] K. B. Strawbridge and F. R. Hallet, "Polydisperse mie theory applied to hollow latex spheres: An integrated light scattering study," Canadian Journal of Physics **70,** 401–406 (1992).

[45] L. Lorenz, in *Lysbevægelsen i og uden for en af plane Lybølger belyst Kulge (Kongelige Danaske Videnskaber Selskabs Skrifter - 1890) in Ludvig V. Lorenz and his contributions to light scattering, Proceedings of the Second International Congress on Optical Particle Sizing* (Arizona State University Printing Service, 1990).

[46] M. I. Mishchenko, L. D. Travis, and A. A. Lacis, *Scattering, Absorption and Emission of Light by Small Particles* (Cambridge University Press, 2002).

[47] W. J. Wiscombe, "Improved Mie scattering algorithms," Applied Optics **19,** 1505–1509 (1980).

[48] B. Jaggi, B. Pontifex, J. Swanson, and S. S. S. Poon, "Performance evaluation of a 12-Bit, 8Mpel/s digital camera," SPIE: Cameras, Scanners, and Image Acquisition Systems **1901,** 99–108 (1993).

[49] S. G. Lipson, H. Lipson, and D. S. Tannhauser, *Optical Physics* (Cambridge University Press, New York, 2001).

[50] M. Pader, "Gel Toothpastes: Genesis," Cosmetics & Toiletries **98,** 71–76 (1983).

[51] A. Florence and P. U. Jani, "Novel oral drug formulations. Their potential in modulating adverse effects," Drug Safety **10,** 233–266 (1994).

[52] R. S. Rounds, in *Volume 67: Liquid Detergents*, K.-Y. Lai, ed., (Dekker, New York, 1996), Vol. 67, Chapter 4: Rheology of liquid detergents.

[53] J. S. Chu, D. M. Yu, G. L. Amidon, N. D. Weiner, and A. H. Goldber, "Viscoelastic properties of polyacrylic gels in mixed solvents," Pharmaceutical Research **46,** 1659–1663 (1992).

[54] T. W. G. Solomons, *Organic Chemistry* (Wiley, 1996).

[55] J. M. G. Cowie, *Polymers: Chemistry and Physics of modern materials* (Intertext Books, Great Britain, 1973).

[56] B. R. Saunders and B. Vincent, "Microgel particles as model colloids: theory, properties and applications," Advances in Colloid and Interface Science **80,** 1–25 (1999).

[57] J. T. G. Overbeek, "The Donnan equilibrium," Progress in Biophysics and Biophysical Chemistry **6,** 57–84 (1956).

[58] L. Baudonnet, D. Pere, P. Michaud, J.-L. Grossiord, and F. Rodriguez, "Effect of dispersion stirring speed on the particle size distribution and rheological properties of Carbomer distributions and gels," Journal of Dispersion Science and Technology **23,** 499–510 (2002).

[59] L. Baudonnet, J.-L. Grossiord, and F. Rodriguez, "Effect of dispersion stirring speed on the particle size distribution and rheological properties of three Carbomers," Journal of Dispersion Science and Technology **25,** 183–192 (2004).

[60] S. R. Raghavan and B. H. Cipriano, in *Molecular gels: Materials with self-assembled fibrillar networks*, R. G. Weiss and P. Terech, eds., (Springer, Netherlands, 2005), Chapter 8: Gel formation: Phase diagram using tabletop rheology and calorimetry.

[61] S. K. Sinha, T. Freltoff, and J. K. Kjems, in *Kinetics of Aggregation and Gelation*, F. Family and D. Landau, eds., (North-Holland, Amsterdam, 1984), Chapter 21: Observation of power law correlations in silica-particle aggregates by small-angle neutron scattering.

[62] G. Beaucage, "Small-angle scattering from polymeric mass fractals of arbitrary mass-fractal dimension," Journal of Applied Crystallography **29,** 134–146 (1996).

[63] J. Teixeira, "Small-angle scattering by fractal systems," Journal of Applied Crystallography **21,** 781–785 (1988).

[64] J. E. Martin, "Scattering exponents for polydisperse surface and mass fractals," Journal of Applied Crystallography **19,** 25–27 (1986).

[65] P. J. Flory, *Principle of Polymer Chemistry* (Cornell University Press, New York, 1953), Chapter 13.3: Swelling of Network Structures.

[66] J. Hasa, M. Ilavsky, and K. Dusek, "Deformational, swelling, and potentiometric behaviour of ionized poly(Methachrylic acid) gels. I. Theory," Journal of Polymer Science **13,** 253–262 (1975).

[67] J. Ricka and T. Tanaka, "Swelling of ionic gels: Quantitative performance of Donnan theory," Macromolecules **6,** 57–84 (1984).

[68] E. Vasheghani-Farahani, J. H. Vera, D. G. Cooper, and M. E. Weber, "Swelling of ionic gels in electrolyte solutions," Industrial Engineering and Chemistry Research **29,** 554–560 (1990).

[69] B. R. Saunders and B. Vincent, in *Encyclopedia of Surface and Colloid Science*, A. T. Hubbard, ed., (CRC, New York, 2002), Chapter : Responsive Microgel Dispersions, pp. 4544–4559.

[70] H. Wu, J. Xie, M. Lattuada, and M. Morbidelli, "Scattering structure factor of colloidal gels characterized by static light scattering, small-angle light scattering, and small-angle neutron scattering measurements," Langmuir **21,** 3291–3295 (2005).

[71] E. Geissler, A.-M. Hecht, C. Rochas, F. Horkay, F. Bley, F. Livet, and M. Sutton, "Small-angle scattering and the structure and dynamics of filled and unfilled rubbers," Material Research Society Symposium Proceedings **661,** KK9.1.1–KK9.1.10 (2001).

[72] D. Lee, I. A. Gutowski, A. E. Bailey, J. R. de Bruyn, and B. J. Frisken, "Structural Investigation of Carbopol by Light Scattering," In preparation (2009).